MASTERARBEIT | MASTER'S THESIS

Titel | Title

Orbital decomposition of the nuclear star cluster in the early-type galaxy FCC047

verfasst von | submitted by

Julia Lamprecht BSc

angestrebter akademischer Grad | in partial fulfilment of the requirements for the degree of

Master of Science (MSc)

Wien | Vienna, 2025

Studienkennzahl lt. Studienblatt | Degree programme code as it appears on the student record sheet:	UA 066 861
Studienrichtung lt. Studienblatt | Degree programme as it appears on the student record sheet:	Masterstudium Astronomy
Betreut von | Supervisor:	Dr. Anja Krause BSc MSc

Acknowledgements

First and foremost, I express my gratitude to my supervisors, Dr. Anja Feldmeier-Krause and Dr. Mariya Lyubenova, for their guidance and mentorship throughout this project and beyond. Their scientific input and support have helped to shape not only this thesis but also the exciting step of starting my PhD this autumn.
I gratefully acknowledge the support of the European Southern Observatory (ESO) in Garching, which hosted me for two research stays and provided financial support through the Undergraduate Program Allowance (UpA). I also thank the University of Vienna for funding my research through the KWA grant, which enabled me to work on this thesis on-site at ESO in Garching.
I would like to thank Dr. Giulia Santucci for guiding me through the development of the decomposition routine, and Dr. Jesús Falcón-Barroso for helping me overcome challenges with the kinematic extraction by publishing a new version of the *Bayes-LOSVD* code. A big thank you to Dr. Thomas Maindl for his immense patience and support whenever I ran into issues with the `DYNAMITE` code. I'm also grateful to Stefanie Reiter, Dr. Katja Fahrion and Dr. Prashin Jethwa for always welcoming my questions and taking the time to explain things – thank you!
A heartfelt thank you to my family and friends for daily motivation and unwavering encouragement. Even though the things I work on may sound more like Chinese or just completely crazy to you, I truly appreciate your steady support.

Now it's just getting started ! :)

Abstract

Nuclear star clusters (NSCs) are among the densest stellar systems in the Universe and often coexist with supermassive black holes (SMBHs) at galaxy centres. While the formation history of a SMBH is essentially lost, NSCs preserve imprints of their evolution in their stellar populations and kinematics, with the latter reflecting cumulative effects of mergers, accretion, and internal dynamical evolution. Despite their ubiquity, the formation and evolutionary pathways of NSCs remain poorly understood. Dynamical modelling has been used multiple times to determine the masses of both NSCs and SMBHs, but so far, the orbital distribution of stars in NSCs has not yet been explored in depth in external galaxies. In this thesis, I present new results using `DYNAMITE` Schwarzschild orbit-superposition modelling to investigate the orbital structure of the unusually large NSC ($R_{\text{eff}} = 66.5 \pm 11.1$ pc) in the early-type galaxy FCC047. The models are constrained using VLT/MUSE IFU data, from which I extract the line-of-sight velocity distribution (LOSVD) via the *Bayes-LOSVD* approach. I decompose the models into hot (low angular momentum), cold (high angular momentum), warm (moderate angular momentum), and counter-rotating orbits. At the nucleus, I detect triple-peaked LOSVDs, revealing a highly complex dynamical structure. This NSC forms a counter-rotating kinematically decoupled core, rotating nearly orthogonal to the galaxy's minor axis. Decomposing the system into its dynamically distinct components reveals a compelling snapshot of hierarchical galaxy evolution. The presence of a dynamically hot, pressure-supported component in the nucleus suggests that a star cluster was accreted early on. The detection of a warm, counter-rotating structure hints at a complex interplay between an inner counter-rotating cold disk and the surrounding stellar population, shaped by past accretion and angular momentum redistribution. The disk might represent a later-formed, strongly rotating, high-angular-momentum component, possibly originating from in-situ star formation fueled by gas inflows that retained the angular momentum of the initially accreted stellar system.

Abstract (ger)

Kernsternhaufen zählen zu den dichtesten stellaren Systemen im Universum und treten häufig gemeinsam mit supermassereichen Schwarzen Löchern im Zentrum von Galaxien auf. Während sich die Entstehungsgeschichte eines supermassereichen Schwarzen Lochs nicht mehr rekonstruieren lässt, bewahren Kernsternhaufen die Informationen zu ihrer Entwicklung in ihren Sternpopulationen und deren Dynamik. Letzteres reflektiert die kumulativen Effekte von Verschmelzungen, Akkretion und interner dynamischer Entwicklung. Trotz ihrer weiten Verbreitung sind die Entstehungs- und Entwicklungspfade von Kernsternhaufen bislang nur unzureichend verstanden. Dynamische Modellierungen wurden vielfach eingesetzt, um die Massen von Kernsternhaufen und supermassereichen Schwarzen Löchern zu messen. Die zugrundeliegende Verteilung stellarer Umlaufbahnen – charakterisiert durch ihren Drehimpuls – wurde jedoch bisher in externen Galaxien kaum untersucht. In dieser Arbeit präsentiere ich neue Ergebnisse basierend auf Schwarzschild-Modellierungen mit `DYNAMITE`, um die Umlaufbahnstruktur des außergewöhnlich großen Kernsternhaufen ($R_{\mathrm{eff}} = 66.5 \pm 11.1\,\mathrm{pc}$) in der Galaxie FCC047 zu untersuchen. Dieser Kernsternhaufen bildet einen kinematisch entkoppelten Kern, der sich entgegen der Gesamtrotation der Galaxie bewegt. Basierend auf VLT/MUSE Daten extrahiere ich die Geschwindigkeitsverteilung entlang der Sichtlinie mithilfe der *Bayes-LOSVD*-Methode, die sich besonders für komplexe Systeme mit mehreren dynamischen Komponenten eignet. Im Zentrum beobachte ich dreifach ausgeprägte Geschwindigkeitsverteilungen, was auf eine hochkomplexe dynamische Struktur hinweist. Die Zerlegung in dynamisch unterschiedliche Komponenten, basierend auf dem Drehimpuls der Sternumlaufbahnen um die kleinste Achse, liefert Einblick in eine hierarchische Entwicklung: Eine dynamisch heiße, druckgestützte Komponente im Zentrum weist auf die frühe Akkretion eines externen Sternhaufens hin. Eine warme, gegenrotierende Struktur deutet auf ein Zusammenspiel mit einer inneren, gegenrotierenden kalten Scheibe und der umgebenden Sternpopulation hin.

Contents

List of Tables

List of Figures

1. Introduction

Nuclear star clusters (NSCs) are extremely dense and massive star clusters [Neumayer et al., 2020]. They are highly luminous and compact resulting in a tremendous rise in the surface brightness of its host galaxy. There is ample evidence that NSCs co-exist with super massive black holes (SMBH) in the centres of many galaxies. While the formation history of the black hole (BH) is essentially lost, NSCs preserve their evolutionary history imprinted onto their stellar populations and kinematics [Thater et al., 2023]. In that sense, they are, until now, studied as morphological light features rather than physical components of external galaxies in the context of dynamics. NSCs have typical effective Radii ($R_{\rm eff}$) comparable to those of Globular Clusters (GC), typically ranging from 3-10 pc, [see Neumayer et al., 2020, and references therein]. The mass range of a NSC is from 10^5 to $10^8 M_\odot$ or in a few extreme cases cases up to $10^9 M_\odot$. Their host galaxies reach across the morphological spectrum from the dwarf galaxies to massive ellipticals and spirals, whereas the NSC number density peaks for host galaxy stellar mass ranges of 10^8 to $10^{10} M_\odot$. More than 70% of galaxies in this mass range host NSCs. Neumayer et al. [2020] emphasize that the mechanisms for the initial NSC formation and their subsequent growth do not necessarily have to be the same. They state, the answer to whether NSCs form before, together with, or after their hosts can help solve basic questions of galaxy evolution. Since they lie deepest in the potential well of galaxies where gas densities are likely to be highest, seed NSCs could be among the earliest structures to form in a galaxy, [see Neumayer et al., 2020, and references therein]. One formation pathway is the gas-free merger of infalling GCs that spiral inwards due to dynamical friction where the strength of this dynamical friction depends linearly on the mass of the cluster [Fahrion et al., 2021]. This might be a natural way to bring metal-poor stellar populations to the centre of the galaxy. The massive star clusters that can inspiral to NSCs appear to be more efficiently produced at low metallicities [Pfeffer et al., 2017]. Another formation pathway is the in-situ scenario where stars form directly at the galactic centre from inflowing gas and local star formation. This might explain the presence of young stellar populations in many NSCs in late-type hosts. Here in-situ star formation is usually invoked, which occurs when gas reaches the central few pc and triggers an intense burst of star formation [Neumayer et al., 2020]. Guillard et al. [2016] have shown that these processes may operate together in a hybrid scenario of gas-rich proto-star cluster accretion. However, how NSC formation mechanisms work in different regimes and what determines galaxy nucleation is still unclear [Fahrion et al., 2021]. Dynamical modelling has been used multiple times to determine the masses of NSCs, but so far the distribution of stellar orbits has not yet been explored in depth. Disentangling the different types of orbits within a NSC, which is usually done based on distinct angular momentum, gives us important hints about the evolutionary history of the galaxy nucleus. Understanding the formation and growth of

NSCs is therefore crucial for a complete picture of galaxy evolution.

1.1. Context

Due to observational constraints, it is not trivial to study a NSC. Considering small effective radii, it is hard to resolve NSCs in external galaxies. The early-type galaxy FCC047 hosts a NSC in its centre with an unusually large $R_{\mathrm{eff,NSC}} = 66.5 \pm 11.1$pc and an age of about 13 Gyrs [Fahrion et al., 2019]. On the grounds of the large size of the NSC, we can formally resolve it using Multi Unit Spectroscopic Explorer (MUSE) data assisted by adaptive optics. The Point Spread Function (PSF) at the Full Width Half Maximum (FWHM) of the MUSE observation corresponds to the effective radius of the NSC. The Field of View (FoV) reaches up to $2R_{\mathrm{eff}} = 5.20$kpc of its host galaxy. Fahrion et al. [2019] explain that this renders FCC047 an ideal laboratory to constrain NSC formation. Additionally, the rich GC system in FCC047 and the host galaxies' younger age (compared to the NSC) of about 8 Gyr makes it a captivating object to study.
In Fahrion et al. [2019], they obtained maps for the stellar kinematics and stellar population properties of FCC047 whilst characterising the stellar light, NSC and the rich GC system simultaneously. They extracted the spectra of the central NSC and showed that it has a distinct stellar population compared to the surrounding galaxy. They found that the NSC is very over-massive and has a strong counter-rotation. It appears kinematically decoupled from the host galaxy with a rotation axis almost orthogonal to the short axis of the galaxy [Fahrion et al., 2019].
More general, in a former work, Fahrion et al. [2021] studied NSC formation pathways and provided a quantitative determination of the relative contribution of the two main processes involved in the assembly of individual NSCs. They combined a semi-analytical model based on the orbital evolution of inspiraling GCs with observed properties of NSCs and GC systems, they constrained the fraction of in-situ born stellar mass $f_{\mathrm{in,\,NSC}}$ as well as the NSC mass and the ratio of NSC to the total GC system for 119 galaxies in the Local Volume, the Fornax, and Virgo galaxy clusters. They use those derived masses to indicate the dominant NSC formation channel. According to Fahrion et al. [2021], more massive NSCs formed predominantly via the in-situ formation of stars ($f_{\mathrm{in,\,NSC}} \sim 0.9$), while the lower-mass NSCs are expected to have formed predominantly through the merger of GCs ($f_{\mathrm{in,\,NSC}} \sim 0.2$). Bringing FCC047 in this context, its high stellar mass of $M_* = (1.04 \pm 0.05) \times 10^{10} M_\odot$ as well as the high mass of the NSC of $M_{\mathrm{NSC}} = 7 \pm 1.4 \times 10^8\, M_\odot$, suggests a high mass fraction of in-situ born stars.
Thater et al. [2023] focus on the mass determination of the SMBH in the centre of FCC047. They show that, for an accurate dynamical model, one has to take into account the effect of a spatially variable stellar mass-to-light (M/L) ratio and a free Initial Mass Function (IMF). They combine large-scale VLT/MUSE and high-resolution adaptive-optics-assisted observations from the Spectrograph for INtegral Field Observations in the Near Infrared (SINFONI) and use a Schwarzschild orbit-superposition approach (with the `DYNAMITE` code) [Jethwa et al., 2020]. Compared to dynamical models with a constant stellar M/L ratio, the black hole mass decreased by 48%. But besides refining the BH mass

measurement, they also took a look into the orbit distribution of the galaxy's nucleus and verified strong rotation and high angular momentum of the NSC, initially suggested by Lyubenova and Tsatsi [2019] and confirmed by Fahrion et al. [2019]. Within the central $1'' \approx 90$pc, they find a large fraction of counter-rotating orbits almost orthogonal (115°) to the short axis of FCC047.

1.2. Strategy and Goals

The goal of this study is to decompose the NSC into dynamically distinct components based on their angular momentum, placing the findings in the context of galaxy nucleation as described by Fahrion et al. [2021]. Building on existing literature described above, this study goes a step further — not only examining the orbital distribution but also decomposing it into distinct orbital types and recalculating kinematics including higher-order moments h_3 and h_4 for each component.
The study follows a structured approach: First, I establish a theoretical framework. Then, I present the MUSE data used in the analysis, along with SINFONI data, which provides additional insight into the kinematic structure of the nucleus. Next, I describe the stellar kinematics extraction using *Bayes-LOSVD*, a method introduced by Falcon-Barroso and Martig [2020], particularly effective for recovering the line-of-sight velocity distribution (LOSVD) in systems with multiple kinematic components on small scales like NSCs.
Dynamical modelling follows, where I reconstruct the galaxy's gravitational potential using `DYNAMITE` to derive the orbit distribution that best fits the input data. This serves as a robust foundation for decomposing the galaxy into its orbital components, thereby with special attention to the NSC. I recalculate the kinematics for each individual component, constrain higher-order kinematic moments, and study the contribution of light. By analyzing angular momentum around both the minor $z-$ and major $x-$ axes, I provide a multidimensional view of the galaxy's and NSC's structure.
Additionally, I investigate differences in kinematic recalculations by comparing two commonly used methods and demonstrating their impact on the counter-rotating components. Finally, I apply the `DYNAMITE` decomposition routine to the SINFONI kinematic set using the best-fit model from Thater et al. [2023]. The structural differences between the MUSE- and SINFONI-based decompositions will be analysed in detail, highlighting how variations in kinematic extraction methods influence orbital distributions and the recovered kinematic properties of dynamically distinct components.

2. Theoretical Background

This chapter outlines the theoretical framework underlying the dynamical modelling of galaxies, which is grounded in the principles of stellar dynamics. The pre-processing starts with reconstructing the gravitational potential of a galaxy, a foundational step that enables the analysis of its internal structure and dynamics. This involves the preparation of input data which will then be processed using the advanced capabilities of the `DYNAMITE` software. At its core, the modelling leverages the Schwarzschild orbit-superposition method to compute the galaxy's gravitational potential.
Once the gravitational potential is determined, the focus shifts to decomposing the system into its orbital distribution. This involves dissecting the galaxy's stellar components into distinct orbits, characterized by properties such as circularity and angular momentum. Understanding these orbital distributions is essential for interpreting the physical processes that drive the galaxy's evolution, including accretion, mergers, and star formation. This chapter explains the theoretical principles and definitions of orbit types used to derive this decomposition, providing a foundation for linking the modelled orbital structures to the galaxy's formation and history.

2.1. Stellar Dynamics

The stellar dynamics approach provides a statistical framework to describe the collective motion of stars influenced by their mutual gravitational field. Instead of focusing on individual stars, this approach derives a macroscopic representation of the system as a whole. In galaxies, stars can be treated as collisionless because the characteristic crossing time t_c and the galaxy's age are much shorter than its relaxation time t_{rel} [Binney and Tremaine, 2008]. The relaxation time is the period after which cumulative stellar encounters cause a star to gain a transverse velocity comparable to its initial velocity [Ferrarese and Ford, 2005].
The collisionless Boltzmann equation, see Equ. 2.1, forms the foundation of this approach, linking the gravitational potential $\Phi(\vec{x}, t)$ with the distribution function $f(\vec{x}, \vec{v}, t)$, which represents the probability of a star occupying a given phase-space point $(\vec{x}, \vec{v})$ at time t.

$$\frac{\partial f}{\partial t} + \vec{v} \cdot \vec{\nabla} f - \vec{\nabla}\Phi(\vec{x}, t) \cdot \frac{\partial f}{\partial \vec{v}} = 0 \tag{2.1}$$

Here, $\vec{v}$ is the velocity vector, $\vec{x}$ the position vector, and t the time. The rate of change of the number of stars within a given phase-space volume is equal to the amount of inflow minus the amount of outflow [Ferrarese and Ford, 2005]. Observationally, individual stars in external galaxies are unresolved due to telescope resolution limits, and only integrated properties, such as averages along the line-of-sight (LOS), are accessible [Binney and Merrifield, 1998]. The motion of individual stars does not directly influence the macroscopic analysis. Instead, their collective behaviour shape the system's overall dynamics.

Dynamical modelling, which involves superimposing orbits, is often employed to determine the central gravitational potential. However, challenges such as low surface brightness and faint absorption lines complicate the obtainment of kinematic data. Extracting stellar kinematical data therefore entails walking a fine line between the need for high spatial resolution and the need for high spectral signal-to-noise [Ferrarese and Ford, 2005].

2.2. Overview

This study employs the Schwarzschild orbit-superposition method to dynamically model a galaxy. Computational tools like `DYNAMITE` play an integral role in this process. The subsequent section explains how to constrain the gravitational potential and outlines the theoretical principles underlying black hole mass measurements via the stellar dynamics approach, with an emphasis on the Schwarzschild method.

The foundation of Schwarzschild modelling was laid in 1979 by Martin Schwarzschild, who introduced the concept of using triaxial potentials to model galaxy dynamics [Schwarzschild, 1979]. However, at that time, the method was purely numerical and lacked the capability to be compared with kinematic observations, limiting its application. Early applications of Schwarzschild models that incorporated observational data were developed for simpler spherical and axisymmetric potentials. For example, Rix et al. [1997] employed spherical models, while Cretton et al. [1999] extended the approach to axisymmetric cases (see van den Bosch et al. [2008] for a detailed review).

Since those early developments, the method has been generalized to triaxial potentials, enabling the modelling of more complex galaxy morphologies [van den Bosch et al., 2008]. Advances in computational techniques and the availability of high-quality observational data have played a crucial role in bridging the gap between numerical models and kinematic measurements. Modern implementations, such as `DYNAMITE`, take full advantage of this progress, providing a robust framework for comparing dynamical models with detailed observational data, including higher-order kinematic moments and multi-component systems.

2.3. Extracting Gravitational Potentials

A galaxy's total gravitational potential Φ_{tot} consists of contributions from the potential of the central black hole $\Phi_{M_{BH}}$, the stellar mass Φ_*, and the dark matter halo Φ_{DM}. This relationship is expressed as:

$$\Phi_{tot} = \Phi_{M_{BH}} + \Phi_* + \Phi_{DM} \tag{2.2}$$

Isolating the black hole's gravitational potential can be achieved by subtracting the contributions of the stellar mass and the dark matter halo from the total potential:

$$\Phi_{M_{BH}} = \Phi_{tot} - \Phi_* - \Phi_{DM} \tag{2.3}$$

Therefore, by constraining the stellar and dark matter potentials as well as the total gravitational potential, it leaves us with the potential of the black hole $\Phi_{M_{BH}}$.

2.3.1. Stellar Potential Φ_*

The stellar potential Φ_* is derived using the observed distribution of stellar light, which is closely correlated with the stellar mass distribution. The Multi-Gaussian Expansion (MGE) method decomposes a galaxy's light distribution into a series of N two-dimensional Gaussians, where each Gaussian has a peak intensity (amplitude) L_j, a width described by its dispersion σ_j, and an axis ratio q_j [the ratio of the minor to the major axis of the ellipse that describes the flattening of the system, Cappellari, 2002]. The 2D surface brightness profile can be written as:

$$\Sigma(x', y') = \sum_{j=1}^{N} \frac{L_j}{2\pi\sigma_j^2 q_j} \exp\left(-\frac{1}{2\sigma_j^2}\left(x'^2 + \frac{y'^2}{q_j^2}\right)\right) \tag{2.4}$$

Here, x' and y' represent the coordinates in the plane of the sky.
To transform the light distribution into a mass map, one can multiply the peak intensity (amplitude) L_j of each Gaussian with a M/L ratio. This has been done many times for constant stellar M/L ratios. However, a spatially varying stellar M/L ratio can be derived from stellar population properties, including metallicity, age, and the IMF. Unlike traditional methods that rely solely on surface brightness distributions, this approach accounts for spatial variations in the IMF and their influence on the stellar M/L ratio. This is in particular useful for galactic systems with significant stellar population variations, such as those hosting a NSC in their centre. Using this approach, the actual observed image is multiplied by the M/L map to produce a mass distribution map. An MGE is then fitted to this mass distribution map, representing stellar mass rather than surface brightness. This approach provides a more accurate conversion from light to mass distributions, accounting for variations in stellar populations.
To accurately recover the galaxy's intrinsic light distribution, observed galaxy images must account for the point spread function (PSF), which describes the blurring effects introduced by the atmosphere and the telescope. The PSF is modelled as a sum of Gaussians and is convolved with the MGE to correct for these effects.
The resulting MGE represent a projected surface mass density Σ_j, which is then converted into an intrinsic three-dimensional mass density, $\rho_*(\vec{x})$, under the assumption of three viewing angles (θ, ϕ, ψ). This critical step is performed using the `DYNAMITE` software.
Finally, the stellar potential Φ_* is computed by solving the Poisson equation, which relates the gravitational potential to the mass density $\rho_*(\vec{x})$:

$$\nabla^2 \Phi_*(\vec{x}) = 4\pi G \rho_*(\vec{x}) \tag{2.5}$$

Here, ∇^2 is the Laplace operator, $\vec{x}$ is the position vector in three-dimensional space, and G is the gravitational constant.

2.3.2. Dark Matter Potential Φ_{DM}

The dark matter potential Φ_{DM} is modelled using a spherical Navarro-Frenk-White (NFW) profile, which is commonly used to describe the distribution of dark matter in galaxies [Navarro et al., 1996]. The density profile of the spherical NFW halo is given by:

$$\rho_{DM}(r) = \frac{\rho_0}{\frac{r}{R_S}\left(1 + \frac{r}{R_S}\right)^2} \tag{2.6}$$

Here, ρ_0 is the characteristic density, R_S is the scale radius, and r is the distance from the centre of the halo. The corresponding potential of the NFW profile $\Phi_{M_{DM}}$ is then again won by solving the Poisson equation:

$$\Phi_{M_{DM}}(r) = -\frac{4\pi G \rho_0 R_S^3}{r} \ln\left(1 + \frac{r}{R_S}\right) \tag{2.7}$$

The scale radius R_S determines the size of the region where the density transitions from a central cusp to an outer decline, and ρ_0 controls the overall density normalization [Navarro et al., 1996].
To define the halo parameters, we use the virial mass M_{200} and virial radius r_{200}, which are related to the region within which the average density is 200 times the critical density of the Universe:

$$M_{200} = \frac{4}{3}\pi r_{200}^3 \cdot 200\rho_{\text{crit}}, \tag{2.8}$$

where $\rho_{\text{crit}}(z) = \frac{3H(z)^2}{8\pi G}$, is the critical density of the Universe, H is the Hubble parameter, and G is the gravitational constant [Dutton and Macciò, 2014]. The fraction f of dark mass to baryonic mass of a galaxy can be calculated by:

$$f = \frac{M_{200}}{M_*} \tag{2.9}$$

Besides the dark matter fraction, the concentration of dark matter within the main halo is another key parameter characterising a spherical NFW dark matter profile. The concentration can be estimated by using the halo-mass relation by Dutton and Macciò [2014], given by:

$$log_{10}c_{200} = 0.905 - 0.101 log_{10}(M_{200}/10^{12}/h), \tag{2.10}$$

They use NFW fits to estimate halo properties, adopting a Hubble constant normalization parameter $h = 0.671$, that is consistent with the Planck cosmology.
In dynamical modelling, as in the DYNAMITE software, the dark matter fraction f and the concentration parameter c_{200} are used to describe a spherical NFW halo.

2.3.3. Black hole Potential Φ_{BH}

Similarly to the dark potential, the black hole potential contributes non-luminous mass to the total gravitational potential of the system. The potential of a black hole is described using a Plummer potential:

$$\Phi_{BH}(r) = -\frac{GM_{BH}}{\sqrt{r^2 + a^2}}, \tag{2.11}$$

where M_{BH} is the mass of the black hole, r is the distance from the centre, G is the gravitational constant. The softening length a prevents the potential from diverging at $r = 0$ to avoid singularities at the centre [Plummer, 1911] [Dejonghe, 1987].
In this context, the black hole dominates the potential in the innermost regions of the galaxy, influencing the kinematics of stars and gas.
In dynamical modelling, as in the DYNAMITE software, M_{BH} can be treated as a free parameter that is constrained during the modelling process. The softening length a is generally chosen to be around $\sim 1/100$ of the spectroscopic spatial resolution. Often it is fixed to $a = 1 \times 10^{-3}$ which is small enough to preserve the observationally inferred gravitational effects of the black hole while avoiding singularities in the centre that would lead to computational instabilities.

2.3.4. LOSVD as a tracer of the Total Gravitational Potential Φ_{tot}

Observationally, the total gravitational potential Φ_{tot} is constrained by the kinematics of stars within the galaxy since they are accelerated by the total mass of the system including baryonic and dark components. Stellar kinematics, derived from spectroscopic observations, provide measurements of the mean velocity and velocity dispersion, along the LOS.
Since individual stars cannot be resolved in external galaxies, the process instead yields a distribution of velocities along the LOS. The LOSVD is represented mathematically in Eq. 2.12, where μ denotes the projected surface brightness at position (x, y) for normalization purposes, $\vec{v_i}$ represents the velocity in the i-th component, and $f(\vec{x}, \vec{v})$ is the distribution function, already mentioned in see Section 2.1 [Ferrarese and Ford, 2005].

$$LOSVD(v_z, x, y) = \frac{1}{\mu} \iiint f(\vec{x}, \vec{v})\, dv_x dv_y dz \tag{2.12}$$

Hence, to infer the total gravitational potential Φ_{tot} the LOSVD must be constructed out of spectroscopic observations. This can be achieved through several methods, such as the Parametric Recovery approach described in Section 3.4.2 or the *Bayes-LOSVD*, more detailed in Section 4.2.

2.4. The Schwarzschild Method

The Schwarzschild method is a powerful technique for reconstructing the gravitational potential of a galaxy by fitting observational data to theoretical models of stellar orbits. The method relies on the principle that the orbits of stars within a galaxy are determined by its total gravitational potential, which includes contributions from the central black hole, stars, gas, and dark matter. By comparing observational data with model predictions, the method allows for the precise estimation of key parameters, e.g. the mass of the black hole, that define the galaxy's structure and dynamics.
A critical aspect of the Schwarzschild method is the iteration of free parameters, such as the mass of the central black hole or the stellar M/L ratio. These parameters are adjusted until the best agreement between the observational data and the modelled distribution is found. The fitting process ensures that the reconstructed gravitational potential is consistent with both the galaxy's observed kinematics (the LOSVD) and its photometric properties (the MGE).
In Application, a large number of stellar orbits are computed and superimposed to reproduce the observed kinematics. This requires solving the equations of motion for a variety of orbit families within the assumed gravitational potential. A non-negative weight is assigned to each orbit which will then be optimized to match the observed LOSVD, as well as constraints from the MGE.
Computational tools like `DYNAMITE` are utilized to handle the complexity and computational intensity of the Schwarzschild method. These tools enable efficient orbit integration, parameter optimization, and weight solving. The process is executed on high-performance computing facilities such as the Vienna Scientific Cluster (VSC-5 and VSC-4), which provides the computational resources necessary to handle the extensive calculations. This combination of advanced open-source algorithms and powerful hardware allows the Schwarzschild method to deliver robust results that enhance our understanding of galaxy dynamics and the role of SMBHs.

2.4.1. `DYNAMITE`

`DYNAMITE` is a versatile tool for dynamical modelling of galaxies. It integrates the equations of motions to create orbits within a given gravitational potential and optimizes the model parameters to fit observed kinematics. Mainly developed at the University of Vienna, `DYNAMITE` supports a wide range of dynamical studies [Jethwa et al., 2020][van den Bosch et al., 2008][Thater et al., 2022].
The Schwarzschild method implemented in `DYNAMITE` involves the following steps:

1. **Prepare a configuration file containing**:
    a) Orbit library settings.
    b) Physical system parameters, such as black hole mass, dark matter fraction, intrinsic shape parameters, and M/L ratio, including upper and lower limits as well as step sizes for the iteration process.

Figure 2.1.: DYNAMITE Logo.

   c) Observational inputs like the MGE and kinematic data.

2. **Orbit integration:** For a position-space grid, `DYNAMITE` chooses initial conditions for each orbit and integrates the equations of motion over defined orbital periods. A tally is kept of how much time each orbit spends in each cell, representing the mass contribution of each orbit to the cell [DYNAMITE, 2025b].

3. **Translate model orbits into "observable" kinematics:** Consider observational effects like the PSF and kinematic binning.

4. **Weight solving:** Assign non-negative weights (between 0 and 1) to the orbits to best match the observed LOSVD and surface brightness.

5. **Evaluate the fit:** Calculate χ^2 values to assess how well the model reproduces the observations. The model with the lowest χ^2 is identified as the best fit.

This process is iterated by adjusting the model parameters until an optimal parameter set is obtained. Different methods are available to explore the parameter space by adjusting the free parameters and reconstructing the gravitational potential. These methods include:

1. **Gridwalk:** This method focuses on the vicinity of the current best fit. The centre of the gridwalk is the parameter set with the lowest χ^2 value, depending on the configuration of the parameter space.

2. **Full Grid:** A complete Cartesian grid is constructed across all free parameters, bounded by specified low/high values with a defined step size. For cases with more than three free parameters, this approach may result in an impractically large number of models.

3. **Legacy Grid Search:** This method explores all plausible models starting from the initial configuration. The process iterates as follows:
   a) Identify all models within a specified threshold of $|\chi^2 - \chi^2_{\mathrm{min}}|$.

b) For each model within this threshold, generate new models by independently stepping ± 1 in each parameter with the defined step size.

c) If no new models are generated at the end of an iteration, the step sizes for all parameters are halved until the specified minimum step size is reached.

Throughout the process, and for the final best fit, plots are generated to visualize the procedure. Several output files, such as orbital weights, are saved, though they will not be discussed in detail here.

2.5. Orbit Distribution

The distribution of orbits within a galaxy provides insights into its internal dynamics and further into its evolutionary history. In the Schwarzschild modelling framework, the orbit distribution serves as a fundamental component for reproducing the observed kinematics and constraining the gravitational potential. By analyzing the contributions of different orbital families, such as box, short-axis or long-axis tube orbits, we can infer the galaxy's intrinsic shape, angular momentum distribution up to formation mechanisms. Orbital types are classified based on their circularity, which quantifies their angular momentum, as well as their random vs. ordered motion. Additionally, the orbital anisotropy, expressed through the velocity anisotropy parameter β, is a key diagnostic of the dynamical state of the system.

2.5.1. Orbit Types and Angular Momentum Conservation in a Triaxial Potential

In a triaxial potential, we define three axes that describe the system. See Figure 2.2, the major x-axis representing the longest axis of the ellipsoid is drawn in red. The intermedite y-axis is inclined and drawn in brown. The shortest z-axis is drawn in green.

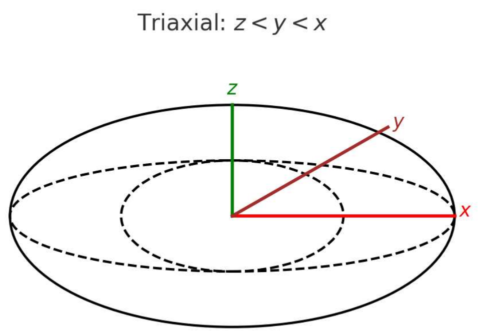

Figure 2.2.: Triaxial ellipsoid with axes labelled as major x-axis (red), intermediate y-axis (brown) and minor z-axis (green).

Tube orbits dominate the orbital distribution in many galaxies and are characterized by their conservation of angular momentum around a specific axis:

- **Short-Axis Tube Orbits:** These orbits circulate around the short z-axis and maintain a constant angular momentum J_z. They are commonly associated with disk-like structures and contribute significantly to rotationally supported systems.

- **Long-Axis Tube Orbits:** These orbits revolve around the long x-axis and maintain a constant angular momentum J_x. Long-axis tubes are often found in triaxial systems, such as elliptical galaxies.

- **Box Orbits:** Unlike tube orbits, box orbits do not conserve angular momentum along any axis. Instead, they fill out a two-dimensional box-like region. These orbits are typically found in the central regions of triaxial or spheroidal systems, contributing to their pressure-supported dynamics.

See Figure 2.3 for visualization of tube and box orbits. Note that orbits around the intermediate axis do not exist in reality since they are unstable [Binney and Merrifield, 1998] [Zhu et al., 2018].

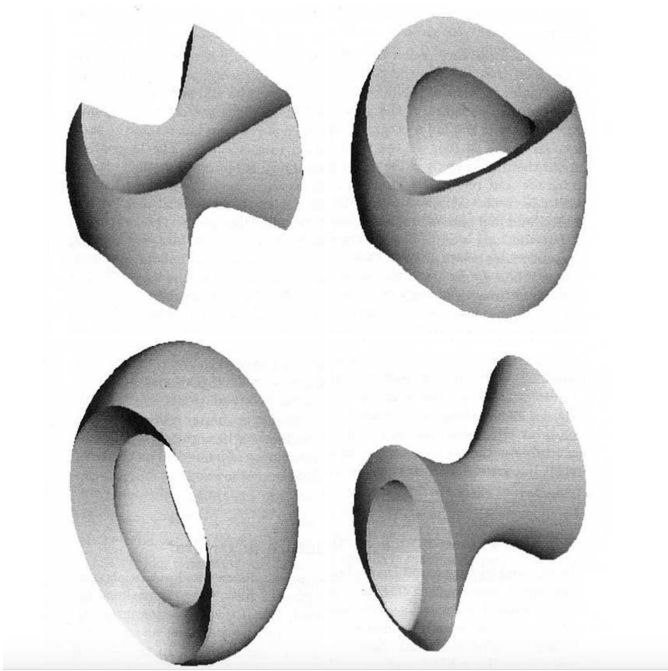

Figure 2.3.: Orbits in a triaxial potential. From top left: box orbits, short-axis tube orbit, inner long-axis tube orbit and outer long-axis tube orbit. Image adopted from Statler [1987].

2.5.2. Orbit Types based on Circularity λ_z

Orbits in galaxies are classified using the circularity parameter, which quantifies the angular momentum normalized by the maximum angular momentum of a circular orbit with the same binding energy [Zhu et al., 2018]. The most commonly used circularity parameter is λ_z, which measures angular momentum around the short z-axis. However, the circularity around other axes, such as λ_x, can also provide valuable insights, particularly for triaxial systems or systems with significant fraction of long-axis tubes. The circularity parameter is defined as:

$$\lambda_i = \frac{J_i}{J_{\max}(E)}, \tag{2.13}$$

where J_i is the angular momentum around the i-th axis ($i = x, y, z$), and $J_{\max}(E)$ is the maximum angular momentum of a circular orbit with the same binding energy E [Zhu et al., 2018]. Looking into both parameters λ_x and λ_z can provide a multi-dimensional view of a galaxy's orbital architecture.
The orbit circularity distributions reveal significant trends across galaxy types:

- **Cold Orbits ($\lambda_z \geq 0.8$):** Dominant in thin disks, these orbits are strongly rotationally supported and most prevalent in galaxies with intermediate stellar masses ($10^{10} M_\odot < M_* < 2 \times 10^{10} M_\odot$) [Zhu et al., 2018]. Exactly circular orbits are a special case that exist only in the plane $z = 0$, where angular momentum around the z-axis is maximized ($\lambda_z = 1$).

- **Warm Orbits ($0.25 \geq \lambda_z < 0.8$):** Primarily short-axis tubes, these orbits retain significant angular momentum but exhibit some random motion. Representing thick disks, warm orbits dominate the overall orbital distribution within the effective radius for most galaxy types [Zhu et al., 2018, Santucci et al., 2022].

- **Hot Orbits ($-0.25 \geq \lambda_z < 0.25$):** Dominated by random motion, these orbits include box orbits and some long-axis tubes. Found in bulges and pressure-supported systems, hot orbits increase in fraction with stellar mass, dominating massive galaxies ($M_* > 10^{11} M_\odot$) [Zhu et al., 2018] [Santucci et al., 2022].

- **Counter-Rotating Orbits ($\lambda_z < -0.25$):** These orbits, indicative of retrograde rotation, provide clues to past interactions or accretion events [Santucci et al., 2022][Thater et al., 2023].

These classifications are essential for understanding the dynamical state of a galaxy, particularly the balance between ordered and random motions.

2.5.3. The Spin Parameter: Fast vs. Slow Rotators

The distinction between fast and slow rotators is based on the spin parameter λ_{R_e} or the specific angular momentum, which quantifies the ratio of ordered to random motion within the effective radius R_e [Santucci et al., 2022]. It is defined as:

$$\lambda_{R_e} = \frac{\sum_{i=1}^{N} F_i R_i |V_i|}{\sum_{i=1}^{N} F_i R_i \sqrt{V_i^2 + \sigma_i^2}}, \tag{2.14}$$

where F_i is the flux in the i-th spatial bin, R_i is the projected distance from the galaxy centre, V_i the mean velocity, and σ_i is the velocity dispersion in the i-th bin.
Galaxies with $\lambda_{R_e} > 0.31\sqrt{\epsilon_{\text{intr}}}$, where ϵ_{intr} is the intrinsic ellipticity, are classified as fast rotators, indicating significant rotational support. Conversely, galaxies with lower λ_{R_e} values are classified as slow rotators, dominated by random motions and pressure-supported dynamics [Emsellem et al., 2011].
The combination of λ_z, λ_x, and λ_{R_e} allows for a detailed exploration of galaxy dynamics and formation histories:

- **Fast Rotators:** Dominated by cold and warm orbits, these galaxies exhibit significant rotational support and are typically associated with disk-dominated systems.

- **Slow Rotators:** With higher fractions of hot orbits and lower λ_{R_e} values, slow rotators are often massive, triaxial systems. Slow rotators are often formed through gas-poor mergers [Zhu et al., 2018].

2.6. Velocity Anisotropy and the β Parameter

The velocity anisotropy parameter, β, quantifies the relative contributions of radial, azimuthal, and vertical components of the velocity dispersion in a stellar system following the definition of [Binney and Tremaine, 2008]:

$$\beta = 1 - \frac{\sigma_{\text{azimuthal}}^2 + \sigma_{\text{vertical}}^2}{2\sigma_{\text{radial}}^2}. \tag{2.15}$$

A system is isotropic if $\sigma_{\text{azimuthal}} = \sigma_{\text{vertical}} = \sigma_{\text{radial}}$, resulting in $\beta = 0$. Tangentially anisotropic systems ($\beta < 0$) are dominated by azimuthal and vertical motions, while radially anisotropic systems ($\beta > 0$) exhibit predominantly radial motions [Binney and Tremaine, 2008].
The anisotropy parameter often varies with radius, requiring a detailed anisotropy profile for a complete characterization. Since observations integrate light along the LOS, the inferred velocity dispersion can be biased towards either radial or tangential motions depending on the underlying orbital composition. In the central regions of a galaxy, where the LOS passes through the densest stellar core, radial velocities dominate the LOS velocity dispersion, causing radially anisotropic systems to have higher central dispersions compared to isotropic or tangentially anisotropic systems. Conversely, at larger radii, where the galaxy's density profile steeply decreases, tangential velocities dominate the contribution to the LOS velocity dispersion. This explains why radially anisotropic

systems tend to have a steeper velocity dispersion profile with radius, while tangentially anisotropic systems show higher dispersions in the galaxy's outer regions [Binney and Tremaine, 2008]. Figure 2.4 shows LOS velocity dispersions as a function of projected radius R/a from spatially identical systems that are either isotropic ($\beta = 0$), tangential ($\beta < 0$) or radially ($\beta > 0$) biased. Figure 2.5 shows individual radial and tangential orbits illustrated by Rasmussen [2016]. The latter are planar orbits that only exist in the midplane with z = 0. Outside the midplane, they would puff up into tube orbits.

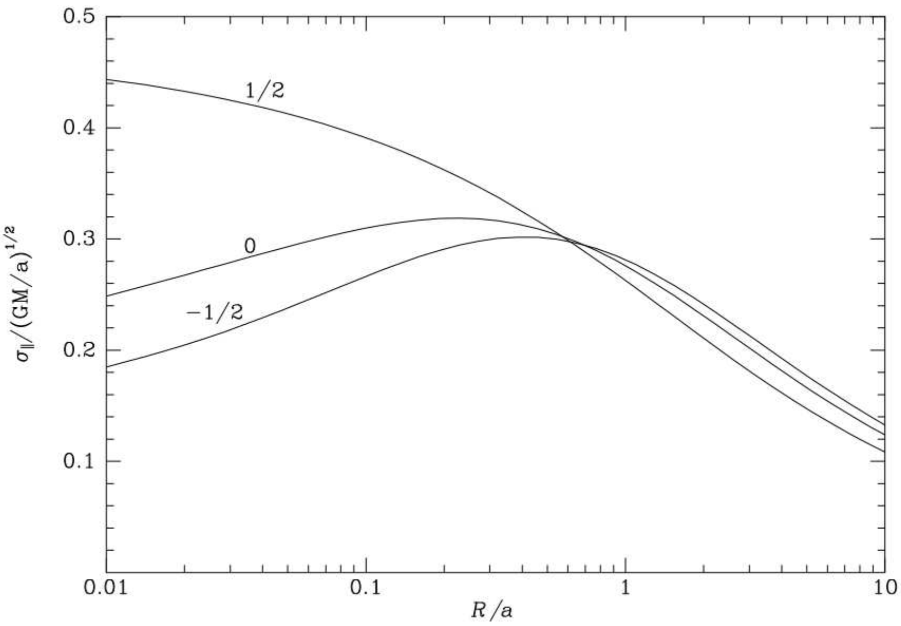

Figure 2.4.: LOS velocity anisotropy as a function of distance to the galatic centre in a Hernquist potential for different values of β [Binney and Tremaine, 2008].

According to Santucci et al. [2022], fast-rotating galaxies are more tangentially anisotropic than slow-rotating systems, which are more radially anisotropic. Besides, the ratio of ordered to random motion increases with increasing ellipticity ϵ_{intr}.

2.6.1. Mass-Anisotropy Degeneracy

A key challenge in dynamical modelling of galaxies is to solve the degeneracy between the mass of the system and the anisotropy β. This arises because the observed kinematics, such as velocity dispersion profiles, can be equally well reproduced by a system with a higher total mass and isotropic orbits, or by a less massive system with significant velocity anisotropy. As a result, the degeneracy complicates efforts to disentangle the galaxy's mass distribution from its orbital structure. The assumption of circular orbits would distort measurements, as dynamically hot stars move in anisotropic orbits characterized by the anisotropy parameter β. While LOS velocity dispersion quantifies deviations from

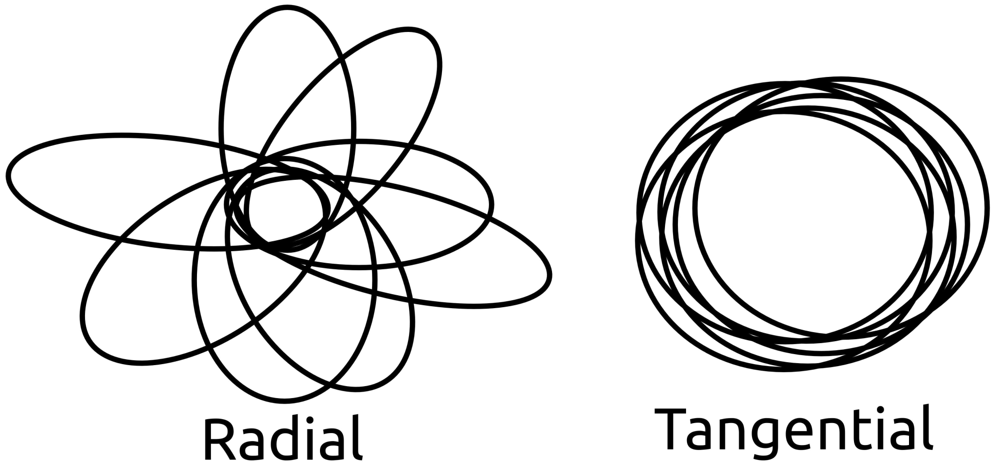

Figure 2.5.: Radial and tangential biased bound orbits [Rasmussen, 2016]. Where isotropic structures would have β value equal to zero, purely tangential orbits correspond to a β value of $-\infty$ and purely radial orbits to a β value of unity.

circular motion, it does not reveal the direction or nature of the orbits [Ferrarese and Ford, 2005]. Resolving this degeneracy requires additional constraints, such as higher-order kinematic moments.

Higher-order kinematic moments

The LOSVD can be expanded using Gauss-Hermite moments, which model deviations from a Gaussian profile via orthogonal functions [Ferrarese and Ford, 2005]. It is expressed as:

$$LOSVD = \frac{e^{-\frac{y^2}{2}}}{\sqrt{2\pi\sigma^2}} \left[1 + \sum h_m H_m(y)\right], \tag{2.16}$$

where $y = (v - V)/\sigma$, V is the mean velocity, σ is the velocity dispersion, H_m is the m^{th} Hermite polynomial, and h_m is the corresponding Hermite moment [Liepold et al., 2020]. Figure 2.6 shows the Hermite polynomials up to order 6.

Higher-order moments, h_3 (skewness) and h_4 (kurtosis), break the mass-anisotropy degeneracy by revealing deviations from Gaussianity (Figure 2.7). Skewness h_3 describes the asymmetry of the distribution: negative skewness indicates a left-skewed tail, while positive skewness indicates a right-skewed tail. Kurtosis h_4 quantifies the sharpness of the distribution's peak: positive excess indicates a sharper peak, and negative excess a flattened peak. These deviations reflect the deviation from circular orbits, providing clues about orbital anisotropy and shapes [Nagel, 2020].

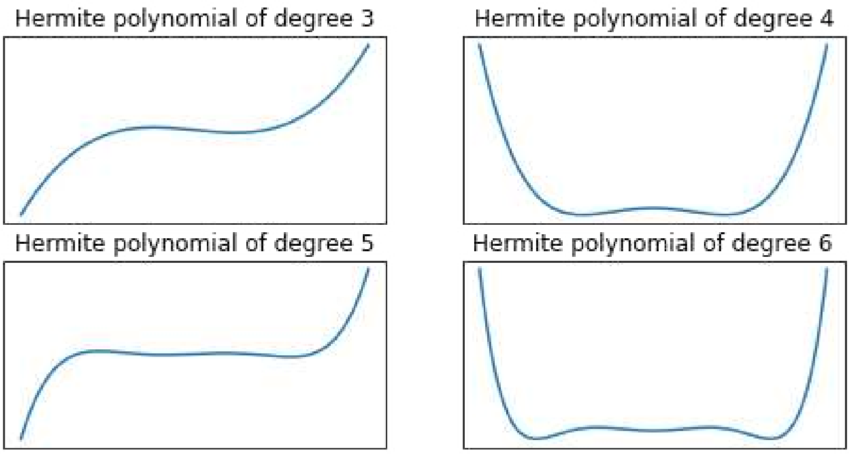

Figure 2.6.: Hermite polynomials from h_3 to h_6.

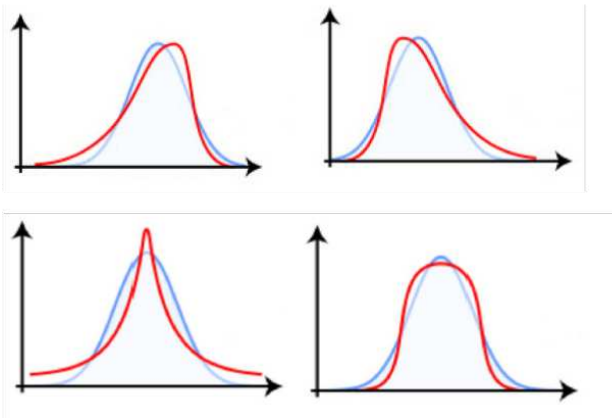

Figure 2.7.: Skewness and kurtosis of a Gaussian. Top figure illustrates skewness (where left is negative skew, right is positive skew, while the bottom figure shows kurtosis (left has positive excess, right negative excess)[Nagel, 2020].

2.7. Connecting Orbit Distribution and Velocity Anisotropy to Galaxy Formation

The orbit distribution and velocity anisotropy profile not only describe the present dynamical state of a galaxy but also offer clues about its formation history. Radial orbits ($\beta > 0$) are indicative of merger-driven formation processes, as such events disrupt isotropy [Burkert and Naab, 2005]. Tangential orbits ($\beta < 0$), on the other hand, might suggest secular processes like bar instabilities or angular momentum redistribution [Athanassoula, 2012].

For example, box orbits, which contribute to triaxial configurations, often accompany

radially anisotropic systems formed through violent relaxation during major mergers [Binney and Tremaine, 2008]. Conversely, disk galaxies dominated by tube orbits exhibit more isotropic or slightly tangentially biased velocity dispersions, reflective of their rotational support [Sellwood, 2014].
Understanding velocity anisotropy is essential for interpreting the observed kinematics and breaking the mass-anisotropy degeneracy. As shown in Figure 2.5, the distinct nature of radial and tangential orbits influences the projected LOS velocity dispersion. Incorporating a velocity anistropy β profile allows for a more robust reconstruction of the galaxy's gravitational potential and its orbital structure. Note that within the Schwarzschild modelling process they are not incorporated per se, however plotted for visualization after finding the best-fit. For example, the so-called Jeans models use a velocity anistropy β profile within the fitting process.
In systems with NSCs, the orbit distribution plays a vital role in understanding the interplay between the NSC and the host galaxy. The decomposition of orbits within the NSC region can reveal whether its structure is dynamically distinct from the surrounding stellar population or part of a continuous distribution. This has implications for NSC formation scenarios, such as in-situ star formation or the accretion of globular clusters. Analyzing the orbital composition in the NSC can also shed light on the influence of the central black hole on stellar dynamics, as well as the processes governing mass inflow and star formation in the central regions [Fahrion et al., 2019][Fahrion et al., 2021][Neumayer, 2012].
In conclusion, the orbit distribution provides a comprehensive picture of a galaxy's dynamical state, its formation history, and its mass distribution. Constraining a galaxy's orbit distribution is advancing our understanding of galaxy evolution, formation and the role of SMBHs co-evolving with their host systems.

2.8. Limitations

Despite that Schwarzschild models provide a robust framework for understanding galaxy dynamics, it is important to acknowledge their limitations. Uncertainties in observational data and simplifying assumptions needed for the models pose challenges.
Dynamical modelling, which involves superimposing orbits, is often employed to determine the central gravitational potential. However, challenges such as low surface brightness and faint absorption lines complicate the obtainment of kinematic data. Extracting stellar kinematical data therefore entails walking a fine line between the need for high spatial resolution and the need for high spectral signal-to-noise [Ferrarese and Ford, 2005].
Observationally, issues such as limited spatial resolution, low signal-to-noise ratios, and biases introduced by the PSF can affect the quality of the input data. These limitations may propagate through the modelling process and might impact the accuracy of derived parameters such as black hole mass measurements or stellar M/L ratios.
Furthermore, dynamical models rely on simplifying assumptions, such as axisymmetry, triaxiality, or specific forms of the (individual) gravitational potential(s). While these assumptions are needed to make the models computationally feasible, they may not fully

capture the true mass distributions of the real galaxy, particularly those with irregular or disturbed morphologies. For instance, the Schwarzschild method assumes that orbital weights are sufficient to reproduce the observed kinematics, but this may not always account for e.g. ongoing mergers, tidal interactions or other processes that changes the morphology of the galaxy.

Finally, the mass-anisotropy degeneracy remains a challenge, requiring additional constraints to disentangle the effects of velocity anisotropy and mass distribution. While incorporating higher-order kinematic moments can address this issue, it may not always be possible to solve it.

In conclusion, while dynamical modeleling offers a powerful tool to investigate a galaxy's structure, reaching their theoretical potential remains restricted on addressing these observational and theoretical limitations.

3. Data

During the following chapter, the galaxy FCC047 and its NSC are introduced. Subsequently, I describe the data used for preprocessing and preparation in the context of dynamical modelling. To study the galaxy FCC047, I employ a combination of spectroscopic and imaging data. The spectroscopic data, specifically the LOSVD, trace the total gravitational potential of the system, since the motion of stars is influenced by the combined effects of baryonic mass, dark matter, and the central potential. Photometric data, on the other hand, are essential for analyzing the galaxy's light distribution. To construct the LOSVD, a high spectral signal-to-noise is needed while for a precise light distribution (MGE) one needs a high spatial resolution. The first can benefit from the large collective area of ground-based telescopes, while the latter demands the use of space telescopes, according to Ferrarese and Ford [2005].

3.1. Facts about FCC047

FCC047 (NGC 1336) is located in the Outskirts of the Fornax Cluster, a well-studied group of galaxies approximately 20 Mpc away that serves as an ideal laboratory for galaxy evolution studies. FCC047 has a redshift of $z \sim 0.0048$, corresponding to a distance of $d \sim 18.3 \pm 0.6\,\mathrm{Mpc}$ [Blakeslee et al., 2009, Simbad2024]. At this distance, 1 arcsecond corresponds to a physical scale of approximately 88.72 pc.[1]

FCC047 is an early-type galaxy, specifically a lenticular (S0), that shows morphological characteristics intermediate between elliptical and spiral galaxies. It features a prominent bulge and an extended disk, but it lacks significant ongoing star formation or pronounced spiral arms. The best-fit deprojection from Thater et al. [2023] revealed triaxial axis-ratios. Additionally, FCC047 hosts a over-large NSC, which provides a unique opportunity to study the interplay between the galaxy's central structures and its overall formation and evolutionary history. The central peak in velocity dispersion provides strong evidence for a SMBH, see the velocity dispersion map of $12'' \times 12''$ in Figure 3.1. The *pPXF* kinematics from Thater et al. [2023] show a peak of $\approx 130\,\mathrm{km/s}$ indicating the presence of the SMBH. Of particular interest is the dynamical mass measurement of the SMBH in the presence of a nearby NSC, providing valuable insights into the complex interactions between these central components. Thater et al. [2023] measured the mass of the SMBH $M_{BH} = 4.4^{+1.2}_{-2.1} \times 10^7 M_\odot$.

The galaxy's inclination, defined as the angle between its LOS and polar axis, has been determined to $i \sim 47 \pm 4^\circ$ based on kinematic modelling [Thater et al., 2023]. The inclination is crucial for dynamical modelling, as it influences the projection effects

[1] based on the calculation: $\mathrm{pc} = 18.3 \times 10^6 \times \pi/0.648$

observed in the galaxy's photometric and spectroscopic data. Together, its location in the Fornax Cluster, the presence of an over-large NSC and its structural properties make FCC047 an excellent object for studying the dynamics and formation history of galaxies and their NSCs.

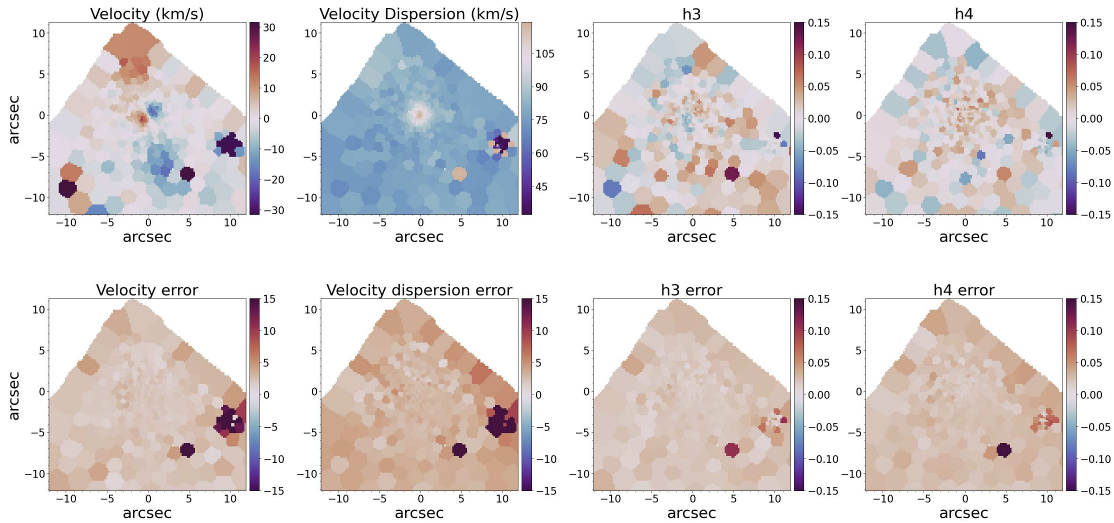

Figure 3.1.: Zoom-in $12'' \times 12''$ *pPXF* Kinematics of FCC047 based on MUSE observations.

3.2. Facts about the NSC in FCC047

While NSCs usually have sizes like a GC, ranging from 3 - 10 pc, the NSC in FCC047 has an effective radius of $R_{\text{eff, NSC}} \sim 66.5 \pm 11.1$pc. It is approximately 13 Gyr old while the galaxy's main body has an age of approximately 8 Gyr [Fahrion et al., 2019]. The large size of the NSC allows it to be spatially resolved using adaptive-optics-assisted MUSE and SINFONI observations. The NSC is kinematically distinct from its host galaxy, showing strong counter-rotation and a rotation axis nearly orthogonal to the galaxy's short axis, see velocity map in Figure 3.1. The NSC's high mass, high metallicity and rotation suggest that its formation cannot be explained by globular cluster (GC) inspiral alone but likely includes significant in-situ star formation that was quickly quenched [Fahrion et al., 2019]. This aligns with findings that massive NSCs are predominantly formed via in-situ processes [Neumayer et al., 2020]. The younger host galaxy age compared to the NSC, along with the large effective radius of the NSC, further highlights FCC047 as an ideal laboratory for investigating NSC formation pathways.

3.3. Photometric Data and Stellar Mass Model

In this section, the photometric data used as the foundation to construct the surface brightness distribution is described as well as the methodology undertaken by Thater et al. [2023] to translate it into the final mass map, which I also utilized in my dynamical modelling. The photometric dataset is a high-resolution imaging obtained with the Hubble Space Telescope (HST). These observations provided the necessary data to analyse the light distribution of FCC047 with high spatial precision.

3.3.1. HST Image of FCC 47

The high-resolution image of FCC047 was obtained with the HST using the Advanced Camera for Surveys (ACS) in the F850LP filter, as part of the ACSFCS project (PI: Jordán, PID: 10217). The F850LP filter is a long-pass filter centred around 850 nm (near-IR), with a broad wavelength range designed to capture light predominantly in the red part of the spectrum, extending slightly into the near-infrared [HST]. The imaging data, retrieved from the ESA Hubble Science Archive, spans a FoV of $202'' \times 202''$ with a spatial sampling of $0.05''$ per pixel and a spatial resolution of approximately $0.09''$ (FWHM), see Figure 3.2. The high resolution is particularly important for recovering the light distribution including the NSC. The wide FoV, meanwhile, ensures sufficient spatial coverage. The image has an exposure time of 1220 seconds, enabling the recovery of lower surface brightness features at the galaxy's edges [Thater et al., 2023].

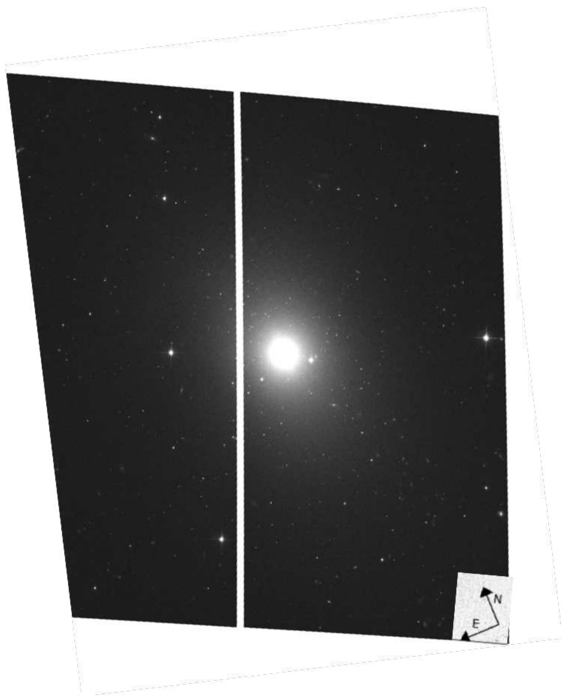

Figure 3.2.: HST image of FCC047 from the ESA Hubble Science Archive.

The find_galaxy routine from the mgefit Python package is a tool for determining photometric properties of imaging data [Cappellari, 2002]. It estimates characteristics such as the galaxy's orientation, ellipticity or photometric position angle, which are essential for constructing accurate models of its light distribution.
See Figure 3.3, where the ellipticity was measured to $\epsilon = 0.348$, indicating the degree of flattening of the galaxy, which is consistent with the findings of Fahrion et al. [2019] of $\epsilon = 0.28$. Caon et al. [1994] also find $\epsilon = 0.26$. Thereby, the routine used 1,358,381 pixels from the image with the peak brightness located at pixel coordinates $(2502, 2070)$, while the mean centre of the light distribution is calculated at $(2522.09, 2080.66)$. Showing the centre and peak intensity are more or less aligned. The galaxy's major axis orientation is determined to be $\theta \sim 163.8°$, measured counterclockwise from the image's x-axis. The astronomical position angle (PA) is 106.2°, measured eastward from north, defining the galaxy's orientation on the sky. These parameters serve as the foundation for subsequent MGE fitting that was done by Thater et al. [2023] and enables accurate deprojection of the galaxy's light into three-dimensional mass density.

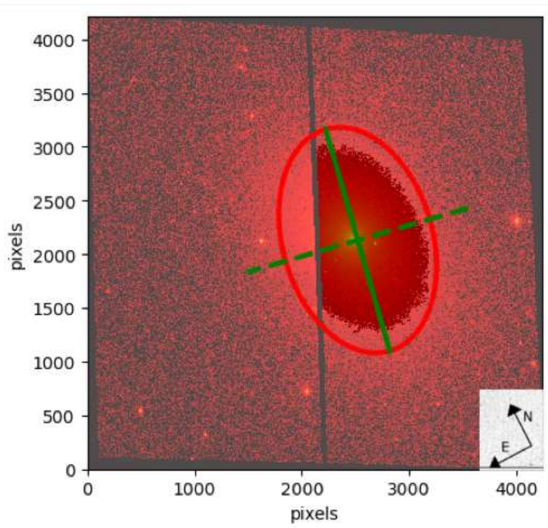

Figure 3.3.: HST image of FCC047 in the find_galaxy routine.

3.3.2. Stellar mass model with a free Initial Mass Function

To generate mass maps, the HST image was rescaled and multiplied with a stellar M/L ratio map derived from stellar population properties, including metallicity, age, and the stellar IMF. These properties were obtained by fitting stellar population models to the MUSE observations (following Section 3.4.1, using spectral index fitting and the Penalized Pixel-Fitting ($pPXF$) technique [Cappellari and Emsellem, 2004] [Martín-Navarro et al., 2019]. This approach goes beyond traditional methods based solely on surface brightness distributions by incorporating spatial variations in the IMF and their effect on the M/L

ratio.

FCC047's large NSC at its centre adds complexity to its stellar population structure. The NSC has a distinct M/L ratio compared to the surrounding galaxy, coming from significant differences in the stellar populations. The M/L map is therefore an essential tool for accurately distinguishing the NSC from the galaxy's main body in the mass distribution. Figure 3.4 illustrates the stellar M/L map for the galaxy, displaying the entire FoV in the left plot and a zoomed-in view of the central region in the right plot, adapted from Thater et al. [2023]. The variation in M/L values between the central NSC and the main body of the galaxy / the outskirts is evident. The centre exhibits a significantly higher stellar M/L of ~ 3.5 in the i-band, reflecting its older stellar population and higher metallicity. In contrast, the outer regions of the galaxy have a lower M/L of ~ 1.5, indicative of younger, less metal-rich stellar populations.

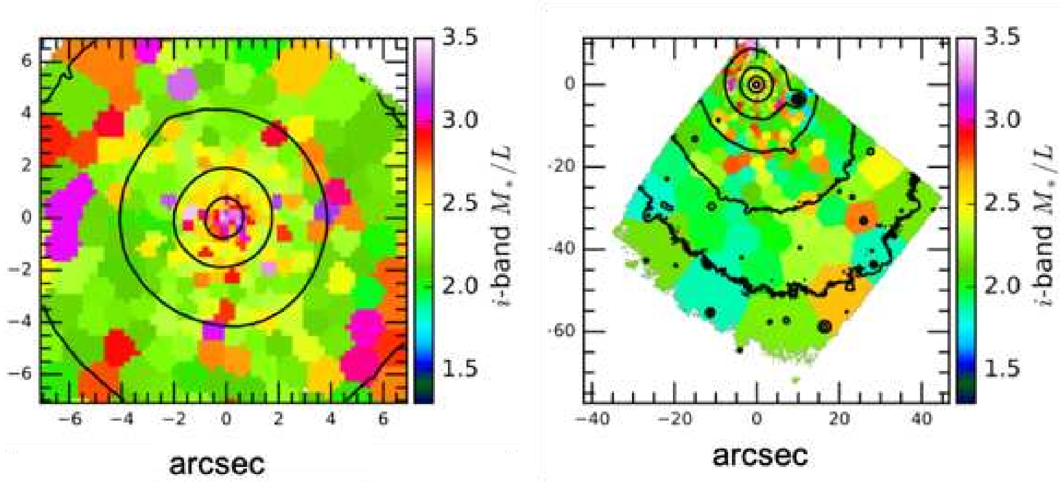

Figure 3.4.: Stellar M/L maps in the i-band from Thater et al. [2023]. The left plot shows a zoomed-in view of the central region, highlighting the distinct M/L ratio of the nucleus compared to the galaxy's outskirts. The right plot presents the M/L distribution across the full FoV. North is up and east to the left.

The resulting MGE describe the galaxy's mass distribution rather than its light distribution. Each Gaussian is described by the projected surface mass density Σ_j $[M_\odot pc^{-2}]$, which is the amplitude of the Gaussian component, and its dispersion σ [arcsec] that expresses the FWHM of the corresponding Gaussian component, see Table 3.1, where all the parameters are listed. Additionally, q'_j, the flattening (b'/a'), needs to be taken into account as well, which indicates the ellipticity of the isophotes. Based on the MGE, further calculations and derivations follow in Section 4.1. See Figure 3.5 for the final mass model from Thater et al. [2023].

Σ_j $[M_\odot pc^{-2}]$	σ_j [arcsec]	q_j
182852.949648	0.037288	0.999900
159793.018604	0.080091	0.999900
218310.655829	0.125750	0.771538
45439.049550	0.262125	0.574536
19145.672785	0.568206	0.862505
4560.008019	1.304108	0.932696
1335.206231	2.208725	0.955103
482.812595	4.053020	0.490000
731.016494	4.221395	0.889459
349.329870	7.219302	0.769863
189.562847	9.532482	0.986934
161.346669	21.599901	0.668807
21.798608	56.036711	0.490000
28.737796	56.036711	0.999900

Table 3.1.: Fitted parameters for 14 Gaussians defining the projected mass distribution of FCC047.

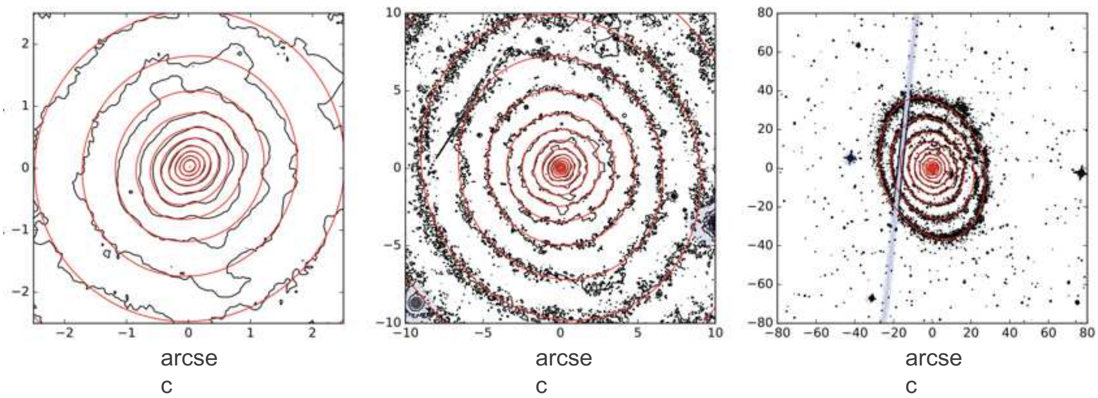

Figure 3.5.: The final mass map after multiplying the HST image with the spatially varying stellar M/L map that takes spatial variations of the IMF into account. From left to right: the left panel focuses on the NSC within a $5'' \times 5''$ region, the middle panel covers a $20'' \times 20''$ region, and the right panel displays the full galaxy. Orientation as in Figure 3.2.

3.4. Spectroscopic Data

In this section, the spectroscopic data used for further analysis is described. The adaptive-optics-assisted Multi-Unit Spectroscopic Explorer (MUSE) instrument on the Very Large

Telescope (VLT) provides the primary spectroscopic data for my Schwarzschild models. This data covers up to $60'' \times 60''$, including the NSC in the centre and surrounding galaxy, with sufficient spatial resolution to resolve the NSC's stellar kinematics.
Complementarily, Thater et al. [2023] utilized both MUSE and the adaptive-optics-assisted Spectrograph for INtegral Field Observations in the Near Infrared (SINFONI) instrument for their models, combining larger-scale observations with high-resolution central data. To extract stellar kinematics, such as the LOSVD, multiple methods are available. As outlined in the theory section (see Sec. 2.3.4), these methods aim to recover the LOSVDs that trace the galaxy's total gravitational potential, influenced by both baryonic and dark matter.

3.4.1. MUSE

MUSE is an integral field spectrograph installed at the UT4 on the VLT at the European Southern Observatory (ESO) in Paranal, Chile. It operates in the visible up to the infrared wavelength range (4650–9300 Å), combining a wide FoV with high spatial and medium spectral resolution, making it ideal for a variety of astronomical studies [Observatory, 2024]. The data was acquired during the Science Verification phase (60.A-9192, P.I. Fahrion) in September 2017 after the commissioning of the Ground Atmospheric Layer Adaptive Corrector for Spectroscopic Imaging (GALACSI) AO system [Fahrion et al., 2019].
Key Features of these MUSE observations:

- **FoV:** $1' \times 1'$, sampled at $0.2''$ per pixel.
- **Spectral Resolution:** $\Delta\lambda = 2.5$ Å (FWHM) at 7000 Å.
- **Resolving Power:** R $\approx \lambda/\Delta\lambda = 2800$ at 7000 Å.
- **Spatial Resolution:** $0.7''$ (FWHM) [Observatory, 2024].

Fahrion et al. [2019] obtained ten exposures with 360 seconds exposure time each, providing sufficient depth for detailed spectroscopic analysis. However, the wavelength range from 5800 to 6000 Å is filtered out due to AO, which operates with four strong sodium lasers. These lasers saturate the detector in the region around the sodium D line at 5884 Å [Fahrion et al., 2019]. See Figure 3.6 for the full and raw MUSE spectrum of FCC047, which includes the central region, the outskirts of the galaxy, and the outskirts of the data cube. What I had in mind when I created this plot was to visualize the increase of flux the more one goes to the centre of the datacube and thereby towards the centre of the galaxy. To compare the noise level of the different regions in the datacube, see Figure 3.7 for the normalized MUSE spectrum of FCC047. The spectrum is divided by its median while ignoring NaN values. It can be easily seen that the level of noise (the sky lines) is much higher in the outskirts of the datacube than in the centre.
Between 6900 Å and 7050 Å, there are few useful absorption lines, limiting the information available in this region. Between 7000Å and 7600Å, the spectrum becomes rather noisy with numerous telluric absorption lines.

Despite these challenges, the wavelength range between 8400 Å and 8900 Å, which includes the Calcium Triplet (CaT), is interesting. See Figure 3.8 for a zoomed-in view of this region. However, masking of the strong sky emission lines in this range is necessary before kinematic extractions can be performed effectively.
In contrast, the wavelength range from 4750 Å to 5450 Å (Figure 3.9) provides a clean region with several strong absorption lines, including H-beta, Magnesium and two Iron features. This region is free from significant sky contamination, eliminating the need for masking during kinematic analysis. As a result, this range was chosen for further analysis, providing a robust foundation for extracting the galaxy's stellar kinematics in Section 4.2.

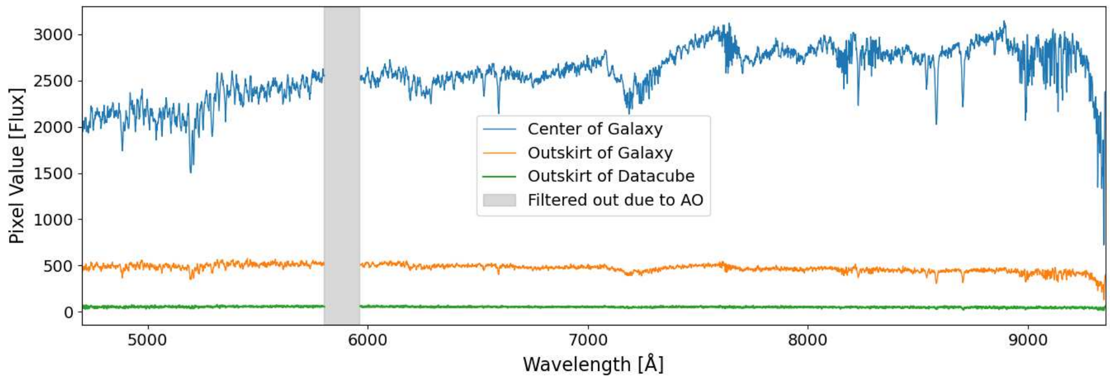

Figure 3.6.: Full MUSE spectrum for three regions in the galaxy FCC047: central region, outskirts of the galaxy, and outskirts of the data cube. The central region shows stronger flux and features compared to the outer regions.

3.4.2. SINFONI

SINFONI (Spectrograph for INtegral Field Observations in the Near Infrared) was an integral field spectrograph installed at the Cassegrain focus of UT3 on the VLT at ESO in Paranal, Chile. It operated from 2003 until its decommissioning in June 2019, conducting observations with AO using either a natural or a laser guide star to achieve near diffraction-limited observations [Observatory, 2019]. Operating in the 1.1 to 2.45 µm wavelength range, SINFONI was particularly well-suited for studying objects obscured by interstellar dust, such as star-forming regions and galactic centres [Observatory, 2019].
Observations for this work were performed under the science programme 092.B-0892 (PI: Mariya Lyubenova) in November 2013 with the AO system in LGS mode.
Key Features of this SINFONI observation:

- **FoV:** $3'' \times 3''$, sampled at $0.05'' \times 0.10''$ per pixel [Lyubenova and Tsatsi, 2019].
- **Spectral Resolution:** $\Delta\lambda = 6.2$ Å (FWHM) with K-band grating (1.95 – 2.45 µm).

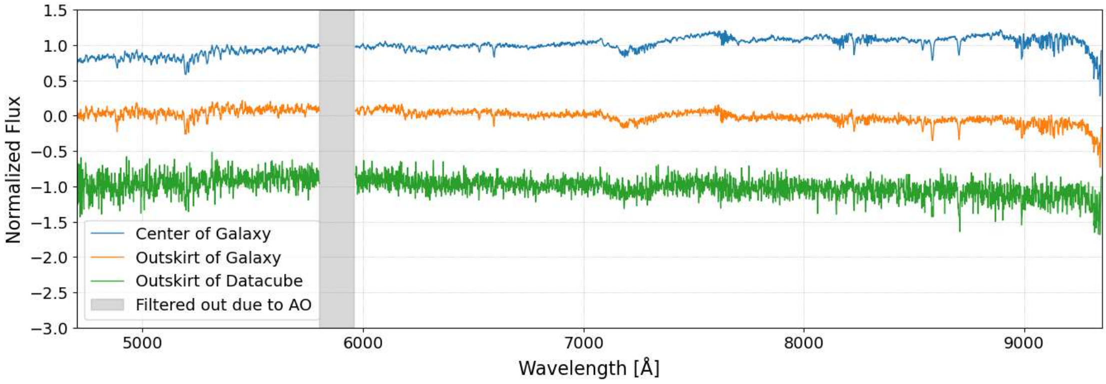

Figure 3.7.: Normalized full MUSE spectrum for three regions in the galaxy: central region, outskirts of the galaxy (offset -1), and outskirts of the data cube (offset -2). It can be easily seen that the level of noise (sky lines) is higher the further out.

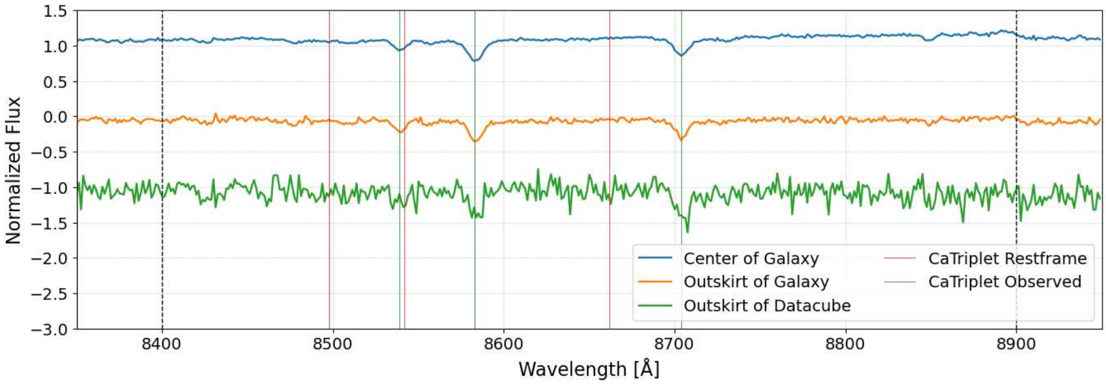

Figure 3.8.: Zoomed-in view of the wavelength range 8400–8900 Å, highlighting the Calcium Triplet (CaTriplet) region.

- **Resolving Power:** R $= \lambda/\Delta\lambda \approx 3550$ at 22.000 Å.
- **Spatial Resolution:** $0.14''$ (FWHM)

I was provided with the extracted SINFONI kinematics used in Thater et al. [2023]. The method employed to construct the LOSVD is known as *Parametric Recovery*, as described in detail by Cappellari and Emsellem [2004]. This technique recovers the LOSVD parameters from galaxy absorption-line spectra using the maximum penalized likelihood approach. The observed spectrum of a galaxy is a superposition of discrete stellar spectra, forming a continuous galactic spectral distribution. The Penalized PiXel-Fitting method (*pPXF*) extracts the galaxy's stellar kinematics by fitting a set of templates to the observed

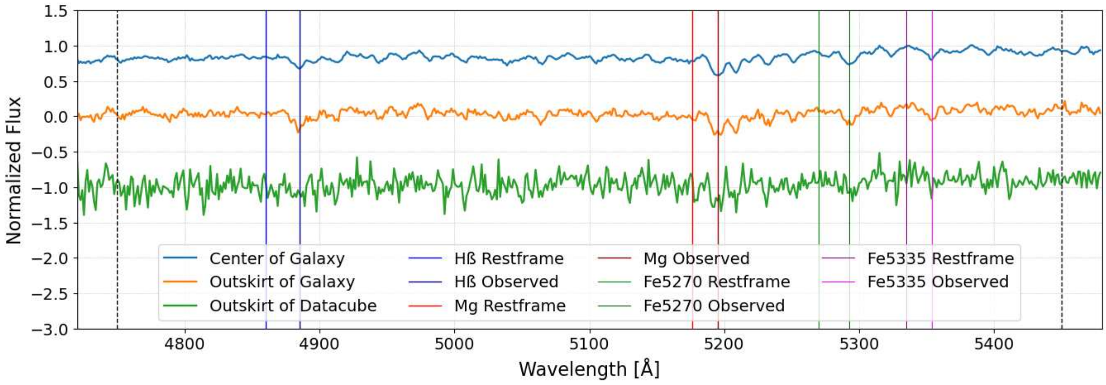

Figure 3.9.: Zoomed-in view of the wavelength range 4750–5450 Å, showing prominent absorption lines such as Hβ, Magnesium and Iron. This region does not require masking and is ideal for kinematic extraction.

spectrum—specifically, the absorption features identified beforehand—via full-spectrum fitting [Cappellari and Emsellem, 2004].

For this dataset, the wavelength range of 2.1–2.36 µm was fitted to a library of seven K and M giant star template spectra observed with the same instrumental setup and regions affected by strong near-infrared sky lines were masked during the fitting process [Lyubenova and Tsatsi, 2019]. The data was subsequently binned into 404 Voronoi bins, each with a target S/N of 40 and a second pass was made into 68 Voronoi bins, each with a target S/N of 100 [Cappellari and Copin, 2003].

See Figure 3.10 for the S/N of 40 and Figure 3.11 for the S/N of 100. The binned coordinates were irregularly spaced and did not display an axis-aligned image with square pixels. To visualize the data, I used the `scipy.interpolate.griddata` method with the `nearest` interpolation scheme. This interpolation method assigns the nearest data value to each point on the beforehand constructed grid, minimizing smoothing effects and preserving the quality of the data. The grid was constructed by sorting and meshing unique binned x and y coordinates. Each figure consists of two rows and five columns with plots from left to right: Flux and below S/N, velocity v and its error, velocity dispersion σ and its error, followed by h_3 and h_4 and their errors.

The plot with a target S/N of 40 exhibits significantly more spatial detail, as it uses more bins. The higher number of bins allows for a finer resolution of kinematic features, capturing more variations in the quantities. However, the error plots reveal larger uncertainties per bin because of the lower S/N. The plot with a target S/N of 100 achieves higher precision per bin but averaging out kinematic details. The trade-off is a significant loss of spatial resolution with only 68 bins. This binning smooths out finer details and results in a more generalized representation of the kinematic and photometric properties. Despite the reduced spatial resolution, the central regions remain well-defined in terms of the flux and velocity dispersion, with the higher S/N enabling a clearer view

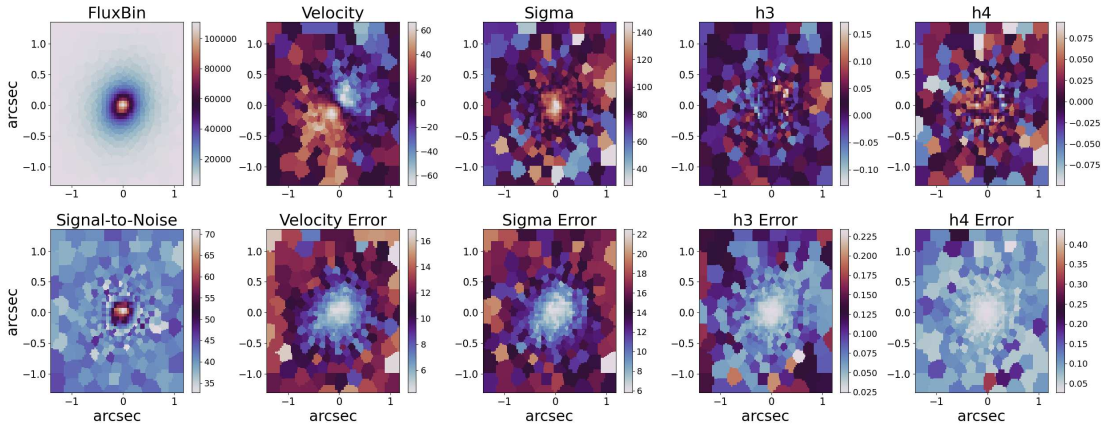

Figure 3.10.: 404 Voronoi bins, each with a target S/N of 40 $^{-1}$.

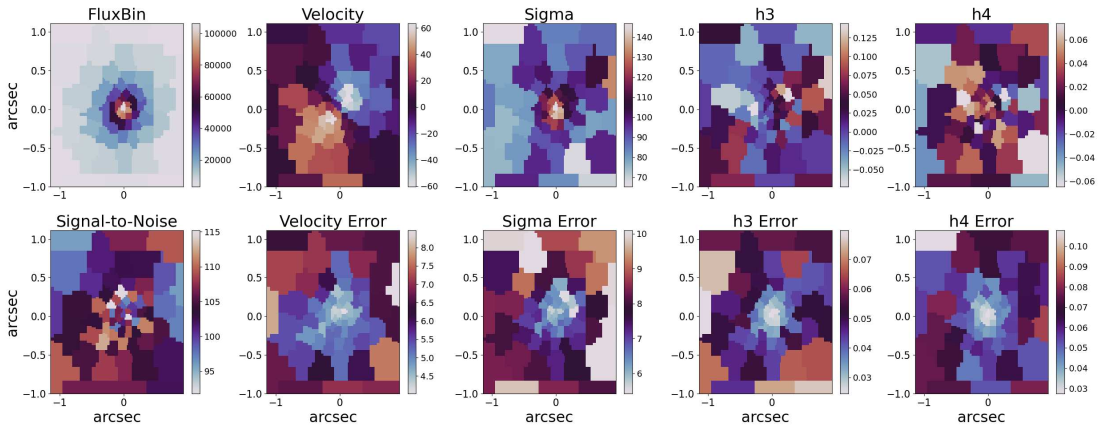

Figure 3.11.: 68 Voronoi bins, each with a target S/N of 100.

of the kinematic features and the higher concentration of surface brightness in the centre, the morphological feature of the NSC. The velocity plots reveal both a clear plattern, indicating the blue- and redshift of the galaxy's nucleus, relative to the systemic velocity, which has been subtracted. The velocity dispersion maps show a strong peak in the centre, indicating the presence of the SMBH. The higher-order Gauss-Hermite moments, h_3 and h_4, reflect asymmetries and deviations from Gaussian velocity profiles, indicating deviations from perfectly circular orbits. What is striking here is the anti-correlation between the h_3 moment and the velocity. Where h_3 is colored red, the velocity is blue. So when h_3 is positive, the LOSVD tends to a left skew while the velocity is negative or moving towards the observer. Thater et al. [2023] decided to use the kinematic data

with a target S/N of 40 for their Schwarzschild models to benefit from the higher spatial resolution, capturing more detailed features of the nucleus of FCC047.
In this chapter, I introduced the galaxy FCC047 and its NSC, highlighting their unique properties that make FCC047 an ideal candidate for dynamical modelling and the study of galaxy evolution. I described the photometric and spectroscopic datasets used in this study, their acquisition, and their role in constructing the stellar mass and kinematic models. The photometric data, derived from high-resolution HST imaging, provided the foundation for building accurate stellar mass models, incorporating spatially varying M/L ratios. The spectroscopic data, obtained from MUSE and SINFONI observations, offered crucial insights into the galaxy's stellar kinematics, enabling the construction of the LOSVD. The combination of these datasets allows for a detailed study of FCC047's structure, dynamics, and central components, including the interplay between the NSC and the SMBH. This robust data framework serves as the basis for the subsequent analysis and dynamical modelling presented in the following chapter.

4. Analysis

In this chapter, I present my analysis of FCC047, focusing on its central region and the NSC. To begin with, I carry out key calculations to better understand the galaxy and if available, compare my results with previous findings in the literature. I examine whether the mass of the SMBH can be dynamically measured and how the resolution of MUSE and SINFONI might limit this endeavor. Additionally, I derive quantities such as the spin-parameter, the effective radius (R_{eff}) and the baryonic mass of FCC047. I estimate the dark matter fraction and provide essential constraints for dynamical modelling and a more complete characterization of the galaxy.

Next, I extract the stellar kinematics of FCC047 and take a closer look at the NSC's kinematics. Using the *Bayes-LOSVD* approach, I obtain kinematics from MUSE data and demonstrate the advantages of this method for systems with multiple kinematic components. The *Bayes-LOSVD* technique allows for a detailed recovery of the LOSVD without imposing parametric assumptions, revealing exciting kinematic features within the NSC.

While I aimed to complement the MUSE kinematics with SINFONI data, I was unable to extract stellar kinematics from the SINFONI dataset using the *Bayes-LOSVD* method. This limitation is because the code currently cannot process K-band data due to the unavailability of appropriate template spectra. Consequently, I rely primarily on the MUSE kinematics for my analysis. However, as it will be demonstrated in the comparison of R_{SoI} and spatial resolution, the MUSE resolution alone is insufficient to robustly measure the SMBH mass. Remarkably, I obtain results that are surprisingly consistent with those of Thater et al. [2023], even using MUSE data alone. Despite this limitation, models based solely on MUSE data still serve as an excellent foundation for the decomposition of the NSC and the galaxy's central region.

To improve the robustness of my models, I perform additional dynamical modelling where the MUSE kinematics (derived with the *Bayes-LOSVD* method) are combined with the SINFONI kinematics extracted using the *pPXF* method by Thater et al. [2023]. These combined models enable a representation of the central kinematics with higher resolution SINFONI data, however finer details might be lost because the *pPXF* method fits a single Gaussian only and fails in providing the evidence for multiple kinematic components.

Finally, based on a chosen orbit library with its respective weights, I decompose the galaxy and identify its constituent orbital components. This decomposition further allows for the separation of the NSC from the galaxy's main body based on the orbit circularity values. It provides critical insights into the dynamical structure of the NSC, shedding light on its formation history and its relationship with the SMBH.

4.1. Calculations and Derivations

4.1.1. Compare the Sphere of Influence to Telescope Resolution

The sphere of influence R_{SoI} of a BH is defined as the region where the gravitational influence of the BH dominates the surrounding stellar potential:

$$R_{\mathrm{SoI}} = \frac{GM_{\mathrm{BH}}}{\sigma^2}, \tag{4.1}$$

where G is the gravitational constant, M_{BH} is the mass of the black hole, and σ is the velocity dispersion of the surrounding stellar population [Ferrarese and Ford, 2005]. The calculation of R_{SoI} assumes isotropy near the BH and a spherical geometry, which may not always represent the true conditions in every galaxy. A comparison of the R_{SoI} of a BH to the telescope resolution determines whether the BH can be resolved and a dynamical mass measurement could be achieved [Peebles, 1972, Kormendy and Richstone, 1995]. To transform to an angular size $R_{\mathrm{SoI}}[as] = \arctan\left(\frac{R_{\mathrm{SoI}}[pc]}{D}\right) \times 3600$, where D is the distance to the galaxy in parsecs.

If the telescope resolution is smaller than the R_{SoI}, the BH lies within the resolving power of the instrument. Conversely, if the resolution exceeds the R_{SoI}, the BH cannot be resolved and observing capabilities are limited. For modern instruments, the effective resolution is influenced by the instrument's PSF [Carroll and Ostlie, 2006].

To calculate the R_{SoI}, I use the best-fit black hole mass from Thater et al. [2023], which is $M_\odot = 4.4^{+1.2}_{-2.1} \times 10^7 M_\odot$, resulting in a $R_{SoI} = 21.69\mathrm{pc} \approx 0.24''$ using an effective velocity dispersion $\sigma_{eff} = 95$ km/s that was derived by co-adding the spectra in elliptical annuli of the size of the effective radius in Thater et al. [2023]. To compare this to the telescope's resolution:

$$\text{MUSE:} \quad \frac{R_{\mathrm{SoI}}[\mathrm{as}]}{\mathrm{Resolution}} = \frac{0.24}{0.7} \approx 0.35 \quad , \tag{4.2}$$

$$\text{SINFONI:} \quad \frac{R_{\mathrm{SoI}}[\mathrm{as}]}{\mathrm{Resolution}} = \frac{0.24}{0.14} \approx 1.75 \quad . \tag{4.3}$$

While MUSE cannot fully resolve the sphere of influence of the SMBH, SINFONI's higher spatial resolution enables a more detailed investigation. It is important to note that the sphere of influence is merely an estimate, providing a guideline on whether resolving the black hole's gravitational effects is feasible for mass measurement. Fahrion et al. [2019] explored FCC047's NSC using MUSE observations and found that, while the NSC is formally resolved at $0.7''$, the resolution is insufficient for detailed dynamical analysis. To overcome this limitation, Thater et al. [2023] combined MUSE data with adaptive-optics-assisted SINFONI observations, significantly improving the resolution of the galaxy centre. Thater et al. [2016] demonstrated that such spatial resolution is crucial for robust SMBH mass measurements using Schwarzschild models.

4.1.2. Effective Radius

The effective radius, also referred to as the projected half-light radius, is the circularized area enclosing half of the analytic total light from the Multi-Gaussian Expansion (MGE). Using the JamPy package developed by Cappellari [2008, 2002], which implements the Jeans Anisotropic modelling (JAM) formalism, the effective radius can be calculated numerically. This tool is widely used in the dynamical modelling of galaxies.
For FCC047, the effective radius was determined using the MGE derived from the stellar mass profile, see Table 3.1 for the fitted parameters for 14 Gaussian components. It computes the cumulative stellar mass as a function of radius and then interpolates to find the radius that contains half of the total stellar mass. The calculations yield an effective radius of $R_{\text{eff}} = 27.10''$, corresponding to $R_{\text{eff}} = 2.40\,\text{kpc}$ when transformed from angular to physical units, assuming a distance of 18.3 Mpc. The effective radius serves as a comparison metric for galaxies and can also be used to constrain the effective velocity dispersion. These results are consistent with findings by Fahrion et al. [2019], who measured $R_{\text{eff}} = 30''$, and Thater et al. [2023], who measured $R_{\text{eff}} = 2.60\,\text{kpc}$[1]. Underscored by Caon et al. [1994], who find $R_{\text{eff}} = 30.8''$.

4.1.3. Spin-Parameter

The spin parameter λ_{R_e} was calculated using binned MUSE data (velocity, velocity dispersion and flux) by Thater et al. [2023] with a FoV of $60'' \times 60''$, resulting in a $\lambda_{R_e} = 0.5595$. For comparison, the threshold value to separate fast from slow rotators $0.31 \times \sqrt{\varepsilon} = 0.1829$, where ϵ_{intr} is the ellipticity, was computed as 0.348 in Section 3.3.2. The approach used to derive λ_{R_e} is described in detail in Section 2.5.3. The calculation involved determining the radius r for each bin using $r = \sqrt{x_{\text{bin}}^2 + y_{\text{bin}}^2}$, limiting it to the effective Radius $R_{\text{eff}} \leq 27.10''$. The resulting λ_{R_e} classifies the galaxy FCC047 as a fast rotator. This result should be treated with caution since FCC047 is dominated by hot orbits with usually low λ_{R_e}. Probably this is because the binned data is not inclination corrected. They reflect the kinematics along the line of sight rather than the intrinsic rotational dynamics. Scott et al. [2014] find $\lambda_{R_e} = 0.32$ with WiFeS integral field observations, also classifying FCC047 as a fast rotator. They do not mention whether they have considered the inclination. Fahrion et al. [2019] find that the MUSE maps do not resemble the WiFes data at all.

4.1.4. Baryonic Mass

After inferring intrinsic luminosity distributions and MGE fitting, one can directly use this to further calculate the baryonic mass of a galaxy by integrating the luminosity obtained from the MGE of the surface brightness profile [Cappellari, 2008, 2002].
The MGE used in this work for further dynamical modelling takes into account a spatially varying M/L ratio with a free IMF, which allows for a more accurate representation of

[1] This measurement has been done with MGE that assume a constant M/L ratio and uses the traditional approach to describe the surface brightness profile. This explains deviations from my calculation.

the galaxy's true luminosity. Unlike models with a constant M/L ratio or a fixed IMF, the free IMF scenario accounts for local variations in the stellar population, leading to a more realistic determination of the luminosity and, consequently, the baryonic mass.
To calculate the baryonic mass of FCC047, the total luminosity is calculated for three different assumptions:

- A constant M/L ratio (Constant),
- A spatially varying M/L ratio with a Milky Way-like IMF (MW IMF),
- A spatially varying M/L ratio with a free IMF (Free IMF).

See Appendix A.1 for the MGE for a constant M/L and MW-like IMF. The Gaussian dispersions (σ) provided in angular units (arcseconds) are converted into physical units (parsecs) using the distance $D = 18.3\,\mathrm{Mpc}$:

$$\sigma[\mathrm{pc}] = D\,\tan\left(\sigma[\mathrm{arcsec}]\right). \tag{4.4}$$

The total luminosity is then calculated as:

$$L = \sum_i 2\pi I_i \sigma_i^2 q_i, \tag{4.5}$$

where I_i is the peak surface brightness, σ_i is the Gaussian dispersion in parsecs, and q_i is the observed axial ratio for each MGE component. The baryonic mass M_{baryonic} is determined by multiplying the luminosity L with the respective M/L ratio from best-fit models of Thater et al. [2023]. The table below lists the resulting luminosities and baryonic masses for three MGE types:

Table 4.1.: Baryonic masses derived from total luminosities and M/L ratios.

Approach	**Luminosity** ($L_\odot$)	M/L **Ratio** ($M_\odot/L_\odot$)	**Baryonic Mass** ($M_\odot$)
Constant ML	5.59×10^9	1.82 ± 0.07	$(1.02 \pm 0.04) \times 10^{10}$
MW IMF	1.15×10^{10}	0.83 ± 0.04	$(9.55 \pm 0.46) \times 10^9$
Free IMF	1.21×10^{10}	0.86 ± 0.04	$(1.04 \pm 0.05) \times 10^{10}$

The uncertainty in the baryonic mass arises due to the uncertainty in the M/L ratio $\Delta(M/L)$. Assuming the luminosity L has no uncertainty, the propagated uncertainty in the baryonic mass is given by:

$$\Delta M = L \times \Delta(M/L).$$

In the following work, I decide to work with a baryonic mass of $1.0 \times 10^{10} M_\odot$.

4.1.5. Dark Matter

For reasons of computational efficiency, I work with a cropped MUSE cube of $15'' \times 15''$, as described in the Data Section 3.4.1. While this spatial extent is sufficient to study the NSC and the orbital components in the central region, it is not large enough to provide robust constraints on the DM fraction. The enclosed mass profile, shown in Figure 4.1, reveals that the dark-matter contribution only accounts less than 20% within $15'' \times 15''$. The baryonic mass "mass-follows-light" is shown in red, the dark mass in blue, and the sum of the two in black. The mass in solar units is a function of distance from the galactic centre in arcseconds (bottom axis) and in kpc (top axis). The figure illustrates that the dark mass begins to dominate only at a radius of approximately $43''$. This plot is derived from an extrapolation by DYNAMITE, where the dark matter fraction is fixed, which is why no error bars are shown in the central regions. However, they start to appear around 1.5 R_{eff} because of the plotting routine. In contrast, the baryonic mass is driven by the M/L ratio, which remains a free parameter and therefore has uncertainties that have an impact on the calculation of the baryonic mass. The shaded regions in the plot are models that lie within the 1σ uncertainty interval.

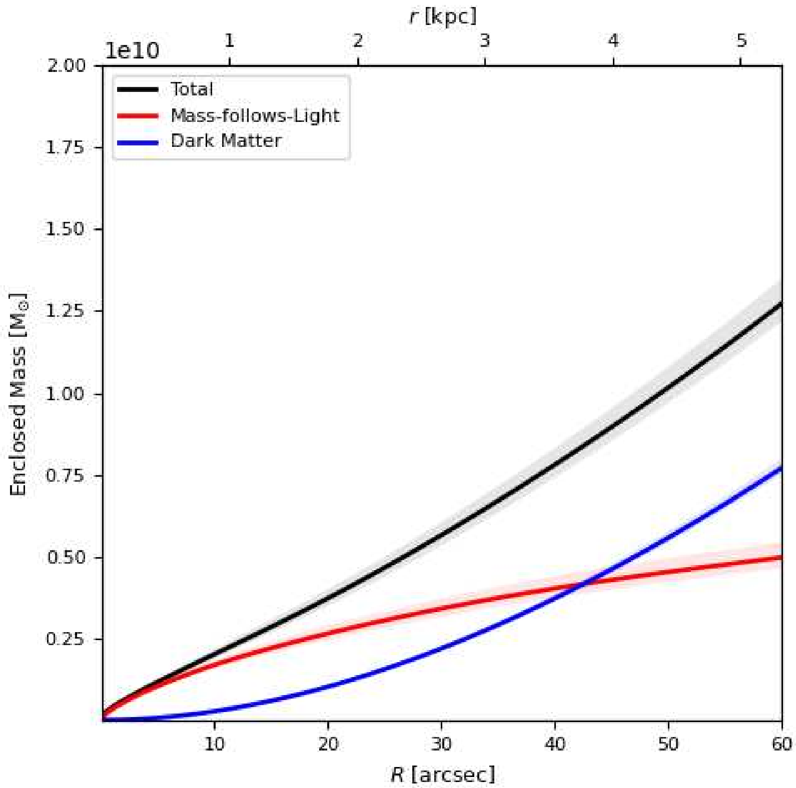

Figure 4.1.: Enclosed mass plot within $R = 60''$ derived with DYNAMITE.

Nevertheless, Thater et al. [2023] and Fahrion et al. [2019] used the full $60'' \times 60''$ MUSE cube for their models and provide robust constraints on the dark matter fraction of FCC047:

Study	**Fraction** (log/lin)	**Concentration** (log/lin)	M/L **ratio**
Fahrion et al. [2019]	$1.5 \approx 31.62$	$1.4 \approx 25.11$	constant
Thater et al. [2023]	$1.78 \approx 60.25$	$0.8 \approx 6.3$	spatially varying
This work based on Moster et al. [2013]	$1.47 \approx 29.51$	$0.96 \approx 9.29$	-

Table 4.2.: Dark matter fraction and concentration for FCC047 from Fahrion et al. [2019] and Thater et al. [2023] as well as my calculations based on simulations from Moster et al. [2013]. The values are shown in both logarithmic and linear scales.

Important to mention is that Fahrion et al. [2019] assume a constant M/L ratio, leading to a slightly lower DM fraction. In contrast, Thater et al. [2023] utilize the MGE with a spatially varying M/L ratio and a free IMF, as discussed above, resulting in a more accurate description of the mass distribution.

Abundance Matching by Moster et al. [2013]

To further validate their results, I apply the method of *Abundance matching* developed by Moster et al. [2013]. In their work, they matched galactic star formation and accretion histories by relating galaxies to dark matter halos. See Figure 4.2, relation of stellar mass to the dark matter halo virial mass M_{200} for different redshifts, based on galaxy evolution simulations. The thick lines are the data, the thinner ones are created by extrapolation. They state that the observational mass error is neglected and the arrows indicate the evolution of a system with a $M_{vir}(z=0) = 10^{14} M_{\odot}$ from z=1 to 0, showing that the more massive it is, the more stellar mass should be lost in course of the evolution of the system.
In Section 4.1.4, I calculate a baryonic mass of $\log(M_*/M_{\odot}) \approx 10$ for FCC047. At a redshift of $z \sim 0.0048$ Simbad2024, the stellar-halo mass relation gives an estimated halo mass of $\log(M_h/M_{\odot}) \approx 11.47$. Dividing these values results in a dark matter fraction at the virial radius R_{200}:

$$\mathrm{f} = \frac{M_{200}}{M_*} = 10^{1.47} \approx 29.5121. \tag{4.6}$$

By using the parameter $h = 0.671$, derived from spherical NFW fits from Dutton and Macciò [2014], I estimate a concentration within the R_{200} virial radius of $c_{200} = 9.29$ or $log_{10}c_{200} = 0.968$, as shown in Table 4.2. These findings are consistent with Thater et al. [2023]. It can be said that if the halo has a lower M_{200}, DM must be concentrated higher and vice versa while the total stellar mass remains constant.

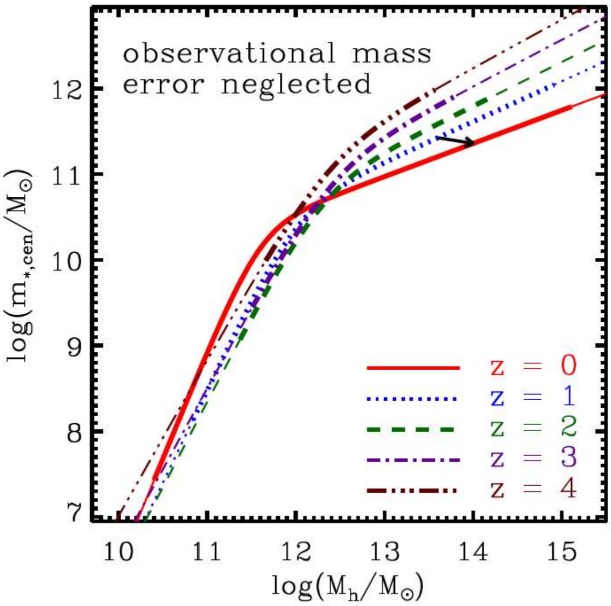

Figure 4.2.: Stellar mass of a galaxy as a function of the DM halo within the virial radius for different redshifts adapted from Moster et al. [2013].

Fixing the Dark Parameters

To ensure an appropriate dark matter fraction and concentration for my Schwarzschild models, I use the values derived from Thater et al. [2023]. Future studies incorporating a wider spatial field or additional constraints from kinematic data could refine these parameters. For the purpose of the NSC analysis, the baryonic mass remains the primary driver of the dynamical model, while the dark matter halo is treated as a secondary component.

4.2. Extraction of Stellar Kinematics

In this section, I outline the theoretical background of the *Bayes-LOSVD* approach, explain why it was chosen to extract the stellar kinematics of FCC047, and describe the execution of the code as well as the interpretation of its results. The resulting Schwarzschild dynamical models, constructed with the *Bayes-LOSVD* kinematics, will then form the basis for analyzing and interpreting the orbital structure of the NSC.

4.2.1. The *Bayes-LOSVD* method and its Advantages

The *Bayes-LOSVD* method from Falcon-Barroso and Martig [2020] is a Bayesian approach to solve the LOSVD extraction, a degenerate problem due to the fact that many combin-

ations of stellar populations and LOSVD shapes can explain the same spectroscopic data. It represents the LOSVD as a sequence of weights applied to template spectra.
Bayesian inference offers several advantages over traditional methods by maximizing the likelihood rather than minimizing the χ^2 as is commonly done. It accounts for uncertainties in the fitting process by allowing the inclusion of physical priors on the input parameters, offering a flexible framework for complex non-parametric LOSVDs [Falcon-Barroso and Martig, 2020]. The *Bayes-LOSVD* approach is particularly advantageous for systems that consist of multiple dynamical components, such as a NSC embedded in a host galaxy. NSCs have more intricate and overlapping kinematic features, which make non-parametric methods like *Bayes-LOSVD* better suited to capture these details. In contrast, parametric methods like penalized PiXel-Fitting (*pPXF*) may impose constraints that might smooth out these details and would fail to resolve subtle features [Cappellari and Emsellem, 2004]. The *Bayes-LOSVD* method is designed to overcome these limitations, making it more suitable for detailed studies of such multicomponent systems.
In the *Bayes-LOSVD* approach, the LOSVD is expressed as:

$$S(v) = \sum_k w_k T_k(v) + B(v) + C(n)$$

where T_k represents the template spectra with weights w_k, $B(v)$ is the broadening function (i.e. the LOSVD), and $C(n)$ is an additive polynomial of order n to reduce template mismatch [Falcon-Barroso and Martig, 2020].
A computational challenges in LOSVD extraction is the large number of templates involved, which can reach hundreds or even thousands. To address this, the *Bayes-LOSVD* method employs Principal Component Analysis (PCA) to reduce the dimensionality of the problem. This approach retains over 99% of the variance in the template library while using fewer than 10 PCA components, significantly reducing computational effort without compromising accuracy.

Regularization and Priors

Bayesian methods naturally incorporate regularization through the use of so called priors, which influence the solution's smoothness and stability [Falcon-Barroso and Martig, 2020]. Several types can be applied:

- **No Regularization:** In the absence of regularization, the LOSVDs in all bins are modelled independently as $\mathrm{LOSVD}_i \sim \mathcal{N}(0, \sigma^2)$, where $\mathcal{N}(0, \sigma^2)$ is a normal distribution with a mean of zero and a variance of σ^2. This approach assumes equal uncertainty for all LOSVDs and provides accurate results in low S/N regimes, though it can lead to high uncertainty and a broad range of possible solutions.

- **Random-Walk Prior:** This prior introduces dependency between LOSVD elements, such that each element is conditioned on the preceding one:

$$\mathrm{LOSVD}_i \sim \mathcal{N}(\mathrm{LOSVD}_{i-1}, \sigma^2).$$

  This leads to a smoothing of the solutions.

- **Auto-Regressive Prior:** The Auto-Regressive prior generalizes the Random-Walk model by linking each LOSVD element to a weighted combination of earlier elements:

$$\mathrm{LOSVD}_i \sim \mathcal{N}\left(\alpha + \sum_{k=1}^{N} \beta_k \mathrm{LOSVD}_{i-k}, \sigma^2\right),$$

  where α and β_k control the level and type of regularization. For $\alpha = 0$ and $\beta = 1$ (for $k = 1$), the prior reduces to the Random-Walk model. Increasing the order k strengthens regularization by linking more elements, but this may smooth out sharp kinematic features such as double-peaked LOSVDs.

- **Penalized B-Spline Prior:** The LOSVD is modelled using piecewise polynomials (B-splines). Regularization is introduced by applying priors to the B-spline coefficients, such as:

$$a_1 \sim \mathcal{N}(0,1), \quad a_i \sim \mathcal{N}(a_{i-1}, \tau), \quad \tau \sim \mathcal{N}(0,1).$$

  It smooths the LOSVD and prevents overfitting. The flexibility of the B-splines is determined by their order k.

In systems with low S/N, unregularized solutions can reveal complex structures like double-peaked LOSVDs, which might be obscured by regularized solutions.

Data Processing

The *Bayes-LOSVD* code is designed to process raw spectroscopic data (3-dim. cubes) from instruments such as MUSE. Typically, the data gets binned to achieve a desired S/N before the LOSVD is extracted. For cases where kinematic data are already binned, the preprocessing pipeline can be modified to read in binned kinematics.
The extraction of the LOSVD is run on high-performance computing systems such as the VSC4. The code compiles using Python 3.6 and GCC version (e.g., gcc/9.1.0) to handle the complex computation involving cached Stan models, see Carpenter et al. [2017] or Stan Development Team [2023], and the convolution of input stellar population templates with the broadening function. The resulting LOSVDs are inspected using a set of Python scripts. Once extracted, the LOSVDs are loaded into a hdf dictionary and prepared in jupyter notebooks for further analysis, such as the construction of Schwarzschild models.

$\hat{R}$ Value and Convergence Diagnostics

The $\hat{R}$ value, the potential scale reduction factor, is a tool used in Bayesian inference to assess the convergence of Markov Chain Monte Carlo (MCMC) simulations. It is particularly used in the *Bayes-LOSVD* context to evaluate whether the MCMC chains used to sample the posterior distribution have mixed well and converged. The $\hat{R}$ value compares the variance between multiple MCMC chains to the variance within each individual chain. If the chains have converged, the variances should be similar, resulting in an $\hat{R}$ value close to 1.

- $\hat{R} \approx 1$: This indicates that the chains have well converged, and the estimates are reliable.
- $\hat{R} > 1$: If $\hat{R}$ is significantly greater than 1, it suggests that the chains have not converged well or at all, and the results may not accurately reflect the posterior distribution. High $\hat{R}$ values indicate that adjustments to the model are needed.

4.2.2. Configuration and Extraction

To start, I processed the raw MUSE datacube by defining the spatial extent and wavelength range, as shown in Figure 4.3. The dataset was cropped to approximately $15'' \times 15''$ for reasons of computational efficiency and to focus on the NSC and its surrounding region, i.e., the galaxy's centre. The spectral range was restricted to 4750 to 5450 Å, covering key absorption features such as Hβ, Mg, and Fe. The reasoning behind this wavelength range is discussed in Section 3.4.1. However, I tested different spectral and spatial extents but ultimately chose this configuration as it produced the most reliable results detailed in the following sections. Processing the entire datacube in its full spatial and spectral extent was technically feasible but would have resulted in unnecessarily high computational costs.

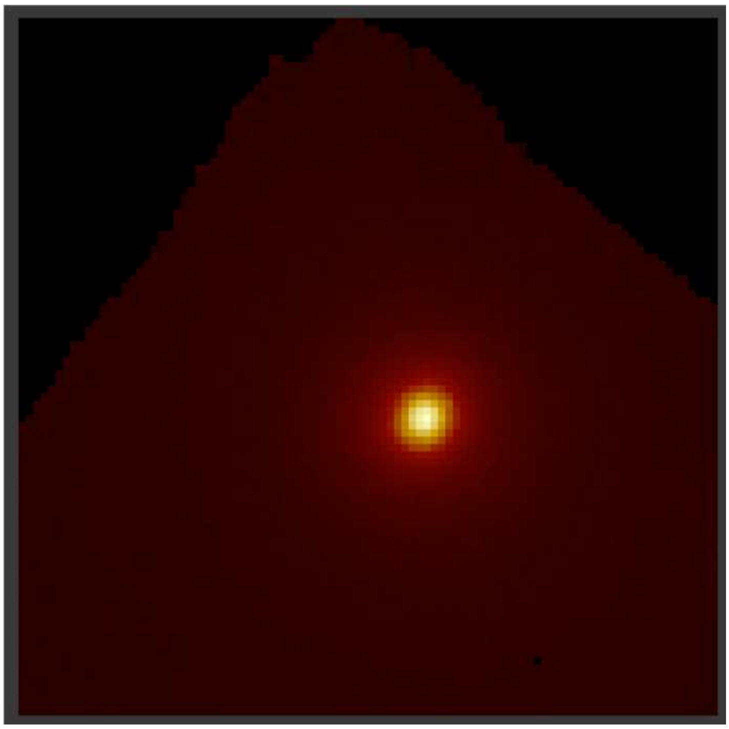

Figure 4.3.: Cropped MUSE cube with spatial extent of $15'' \times 15''$ and wavelength range of 4750 to 5450 Å. North is up and East is left.

Next, I configured the *Bayes-LOSVD* setup using a configuration file, which included essential parameters such as redshift, velocity range, signal-to-noise (S/N) threshold, and the selected template library. The key parameters are listed below:

- **Redshift:** 0.004800
- **Wavelength range:** 4750–5450 Å
- **Velocity scale:** 60 km/s/pix
- **Max velocity:** 700 km/s
- **S/N threshold:** 100 (min S/N = 1)
- **Template library:** MILES_SSP, see Sánchez-Blázquez et al. [2006]
- **Polynomial order: 1**
- **Principal components (PCA):** 5 components, explaining 99.95% of the variance

The datacube was binned to a target S/N of 100, resulting in 828 bins. The central bins, containing the highest S/N values, were particularly relevant for studying the NSC. A visual representation of the bins is shown in Figure 4.4. Although individual bin numbers are difficult or impossible to read, this figure still serves as a useful overview. During this analysis, bin number 320 and 781 were excluded due to poor convergence, with $\hat{R}$ values up to 1.8. Usually, $\hat{R}$ values up to 1.1 are considered acceptable. Additionally, bins in the upper outer region were excluded due to the presence of several NaN values in the processed data. To address this, I manually set the uncertainties in the bins 310, 320, 333, 369, 373, 375, 397, 430, 529, 683, 781 to 10.000, highlighted in orange, to ensure that only well-converged bins are considered. See Figure 4.5 for the data processing and fitting process for stellar population modelling. The top panel shows the central spectrum of FCC047. The x-axis represents the rest-frame wavelength in Å. The y-axis shows the normalized flux. It shows absorption features characteristic of stellar populations, such as those around ~ 4850 and ~ 5200, referring to elements like Hβ, Mg and Fe. The middle panel shows the mean template spectrum derived from the stellar library MILES_SSP. A single stellar population corresponds to the same age and the same metallicity. It closely resembles the observed spectrum, indicating a good match between the data and the template. The bottom panel shows the PCA templates that reduce the dimensionality of the stellar library during the fitting process. Each curve (in different colors) represents a principal component that captures significant variance in the template library. See Figure 4.6 for the fitted spectrum. The black line shows the observed spectrum, the red line the best-fit model and the residuals are shown in green. Additionally, the dashed lines show the continuum level, that provides a baseline for the normalization of the spectrum. It highlights the effectiveness of the fitting process as the modelled spectrum closely matches with the observed spectrum with minimal residuals.

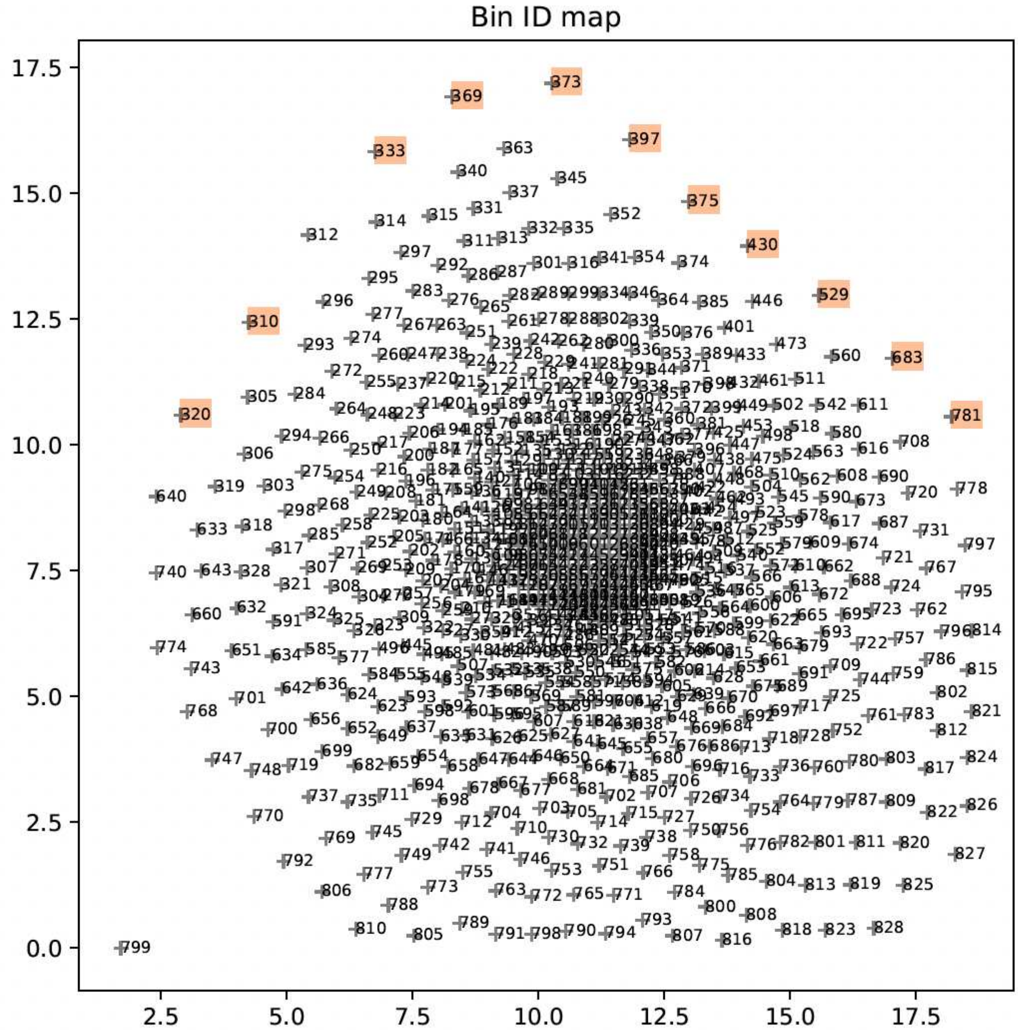

Figure 4.4.: Bin ID map of the cropped MUSE datacube. The central region contains the highest S/N values. The bins that did not converge well are highlighted in pink. Orientation as in Figure 4.3

4.2.3. Comparison: Unregularized vs. Regularized Kinematics

I tested various regularization methods, including different orders k for some, but all of them tend to smooth out the finer details of the kinematic structure. Without regularization, the LOSVD reveals finer details of the LOSVD, especially in the galaxy's nucleus. However, the regularization does help to reduce uncertainties. Figure 4.7 illustrates the difference between regularized (right) and non-regularized (left) solutions,

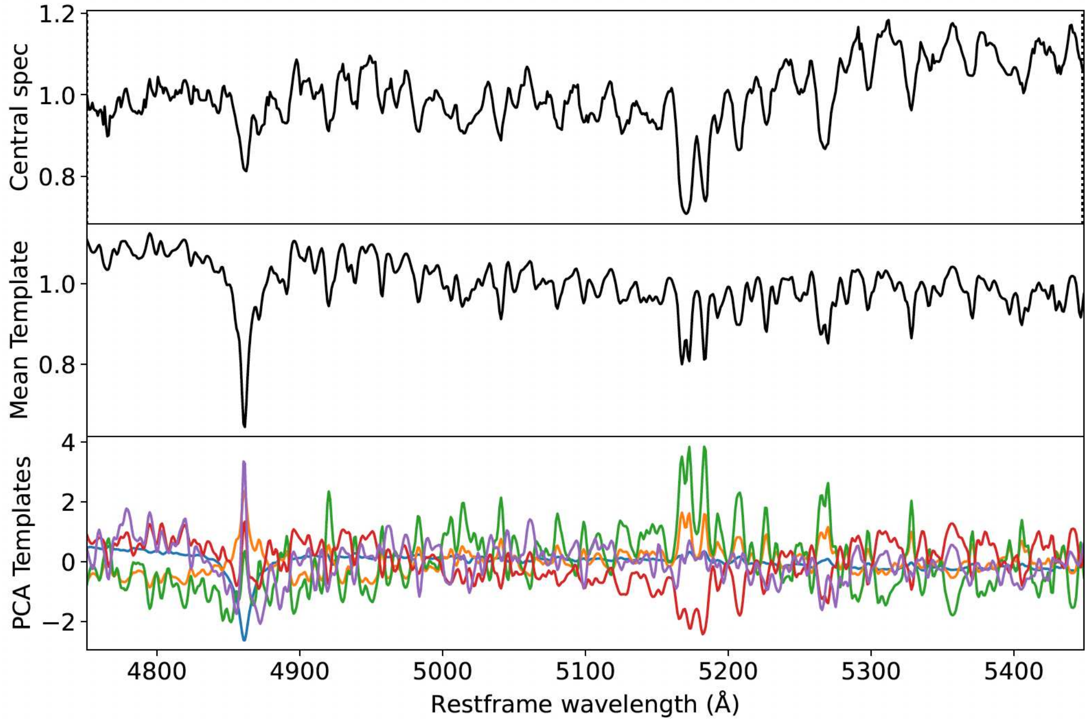

Figure 4.5.: This figure demonstrates the data preprocessing and fitting process for stellar population modelling. Top panel: Normalized spectrum. Middle panel: mean spectral templates and bottom panel: PCA templates

with the regularized solution (using Random-Walk regularization) exhibiting a smoother distribution. The peak amplitude for the non-regularized solution is slightly higher than for the regularized, which has a more symmetrical peak. In the following analysis, I chose to explore the stellar kinematics without applying any regularization to preserve the significant details of the kinematic structure.

4.2.4. Interpretation of the Stellar Kinematics

A LOSVD histogram represents the probability distribution of velocities along the line of sight. See the left plot in Figure 4.8 for the LOSVD Histogram for bin 0 of FCC047 in a linear scale. The x-axis is divided into 23 velocity intervals, each spanning 60 km/s, while the y-axis denotes the probability amplitude for each velocity interval. The 68% confidence interval corresponds to the range of velocities around the mean where 68% of the total probability is concentrated. This interval provides a measure of uncertainty and captures the majority of the velocity distribution, analogous to one standard deviation in a Gaussian distribution. An advantage of using the *Bayes-LOSVD* approach is its ability

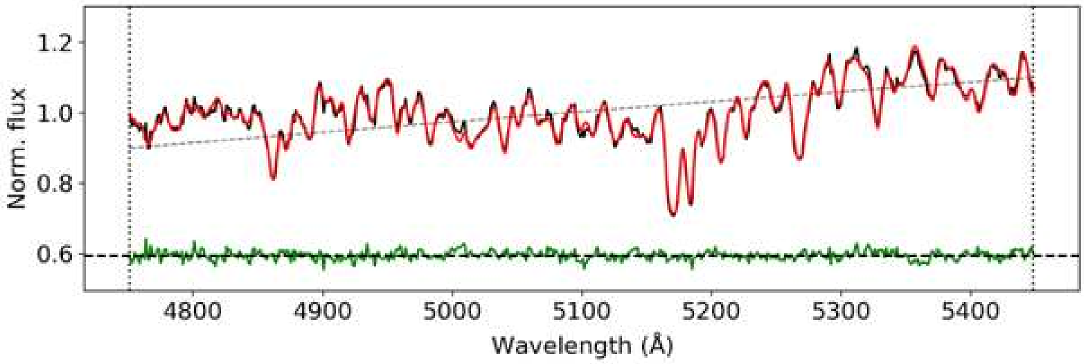

Figure 4.6.: This Figure shows the effectiveness of the fitting process as the modelled spectrum (red) closely matches the observed spectrum (black) with minimal residuals (green).

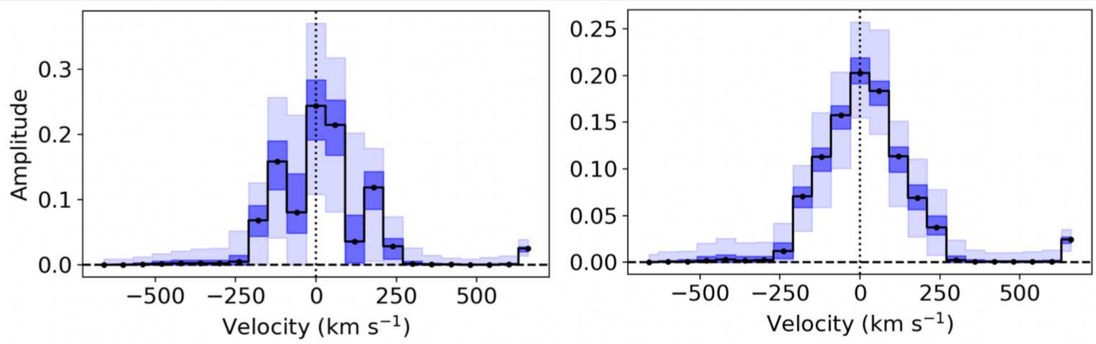

Figure 4.7.: Comparison of Bin 0 between regularized and non-regularized LOSVDs. Here in particular the Random-Walk Regularization. Regularization smooths out fine kinematic details, particularly in regions of lower S/N.

to reveal complex LOSVD structures, such as triple-peaked distributions as it is the case here. This allows for the detection of substructures or kinematic components that would otherwise be unresolved or smoothed out with traditional methods.
See Figure 4.8 for the LOSVD Histogram for bin 0 of FCC047 in a logarithmic scale. The long tails in the *Bayes-LOSVD* distribution contrast with the Gaussian approximation (in red), which would appear wider than the median *Bayes-LOSVD* result in a linear scale. *Bayes-LOSVD* does not force the LOSVD to decay at large velocities. The long tails give rise to large standard deviations. The key kinematic parameters, mean velocity and velocity dispersion, were extracted from the LOSVD using a `DYNAMITE` data preparation notebook. The mean velocity v and velocity dispersion σ for each aperture are calculated based on the marginalised LOSVD data. First, LOSVD values get normalized to ensure they sum to 1 per aperture. Then computing the mean velocity as the weighted sum of

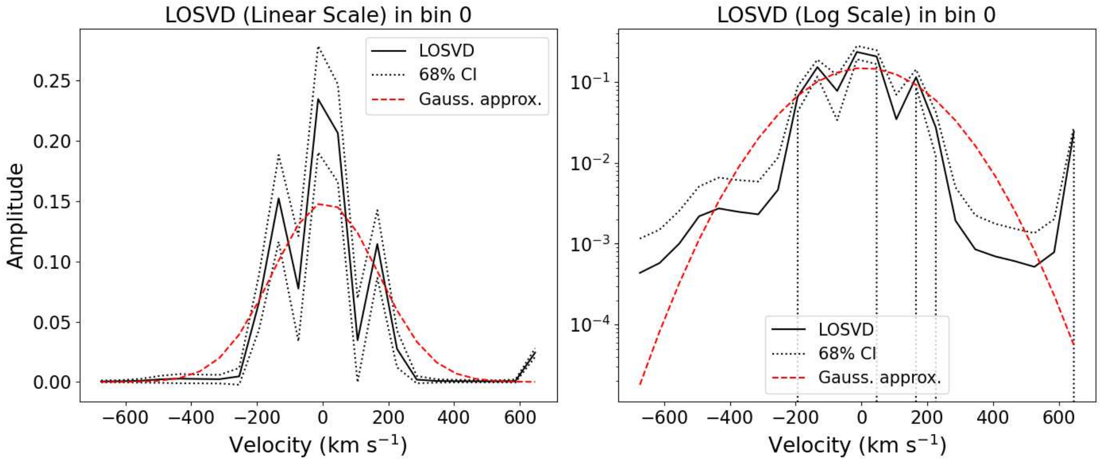

Figure 4.8.: LOSVD of Bin 0 centred on the systemic velocity in a linear vs. logarithmic scale. An advantage of using the *Bayes-LOSVD* approach is its ability to reveal complex LOSVD structures, such as triple-peaked distributions. It shows extended tails, which are better suited for capturing complex kinematic features.

velocities. The velocity variance is calculated from the squared deviations of velocities from the mean, weighted by the LOSVD. The square root of this variance gives the velocity dispersion [DYNAMITE, 2025a].
The right plot in Figure 4.9 shows the binned standard deviations (velocity dispersions) for FCC047 colorcoded from 60km/s up to 200km/s. Thater et al. [2023] report a maximum velocity dispersion of approximately 130 km/s in the centre of FCC047. However, the velocity dispersion values obtained with *Bayes-LOSVD* often appear inflated due to the extended tails of the LOSVD being unrepresentative of the width of the main body of the distribution. Additionally, see the left plot in Figure 4.9 for the binned averaged velocities of the LOSVD histograms centred on systemic velocity (flux weighted mean velocity). Spanning a range from -30 km/s to 30 km/s, blue- and redshift patterns are subtle but discernible in the centre and main body of FCC047.

4.2.5. Interpretation of the Central Region Kinematics

Given that the NSC is in the galaxy's nucleus per definition, it can be assumed that it is located in or close to Bin 0. The binning routine starts with Bin 0, which corresponds to the area with the highest signal-to-noise ratio (S/N), typically aligning with the galaxy's nucleus. The central bins within a radius corresponding to the NSC's effective radius ($R_{\text{eff}} = 66.5$ pc $= 0.74''$) can be selected as those that most likely contain the NSC.[2] This

[2] 1" is approx. 88.7 pc at 18.3 Mpc distance

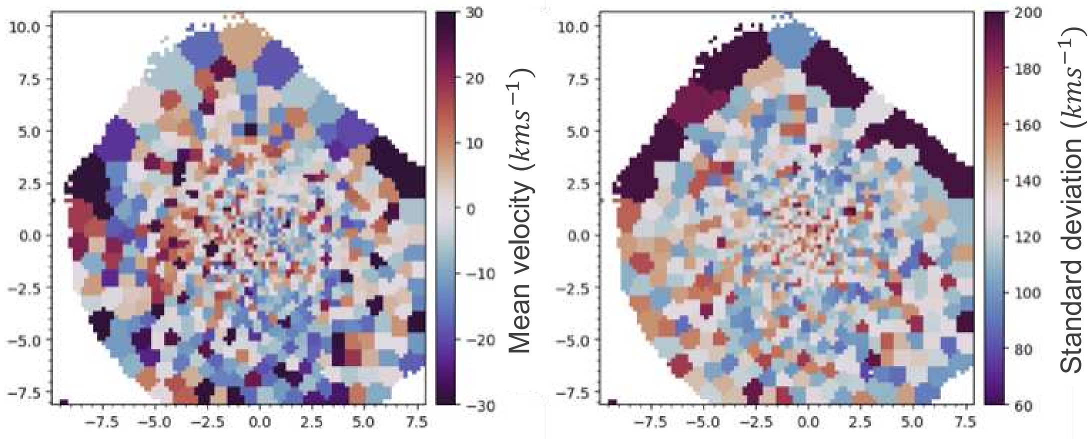

Figure 4.9.: Binned averaged velocity and so-called inflated velocity dispersions. North is up and East is left.

corresponds to approximately 4 bins, given the pixel scale of 0.2″ per pixel and the seeing conditions that also need to be taken into account (0.7″).
See Apendix A.1 for the LOSVD histograms corresponding to the region of the galaxy nucleus. These bins display the region with the highest S/N and thereby, kinematic properties of the NSC, such as higher velocity dispersions and complex velocity structures. The primary peaks are typically concentrated around the systemic velocity (0 km/s) or slightly offset, indicating a dominance of ordered motion. Secondary peaks, when present, are often offset by 200–300 km/s. Many of these bins have complex velocity structures, with a combination of single, double, and even triple-peaked distributions:

- Single-peaked LOSVDs: These are typically found in bins located further from the very centre of the NSC. These distributions suggest a more uniform stellar population moving in a relatively smooth velocity field. This indicates that the stars in these regions are likely orbiting the galaxy in a ordered manner without significant perturbations.

- Double-peaked LOSVDs: Closer to the nucleus, some bins display double-peaked LOSVDs. This indicates the presence of two stellar components moving at distinct velocities. Double-peaked distributions are usually interpreted as evidence of kinematic substructures, such as counter-rotating stellar populations or the presence of a stellar disk. The existence of such features can also suggest interaction between different dynamical components, possibly due to the influence of the SMBH or past mergers.

- Triple-peaked LOSVDs: In some cases, a triple-peaked LOSVD can be observed, particularly in the very central bins. These distributions may point to the presence of more than two distinct kinematic components, suggesting highly complex dynamics near the NSC. This is validating the results found by Fahrion et al. [2019] that there is significant counter-rotation in the centre.

In comparison, see Appendix A.2 for a random sample of bins around the galaxy, spanning from the central region to the outskirts of the galaxy, providing a broader view of the kinematic diversity. The peaks in the central bins are sharper and more prominent compared to the outskirts, reflecting the higher velocity dispersion and stronger gravitational influence in the central regions. The peaks in the outskirts tend to be broader, single-peaked and less defined compared to the central bins, reflecting lower velocity dispersion and weaker gravitational influence. The 68% confidence intervals tend to be larger in the outskirts likely due to lower signal-to-noise ratios in these regions. The dominant middle peaks in the central regions are mostly around 0 km/s or show moderate offsets. In contrast, peaks in the outskirts are more widely spread across a broader velocity range.
The overall results from the *Bayes-LOSVD* model provide a comprehensive understanding of the kinematic structure of FCC047, which will serve as a foundation for further dynamical modelling and analysis of its orbital structure.

4.3. Dynamical modelling

The following section outlines the dynamical modelling process. The model is based on *Bayes-LOSVD* kinematics using MUSE data alone, as the integration of *pPXF* SINFONI and MUSE data became feasible shortly before the completion of this thesis. Since I dedicated significant time to modelling MUSE-only data and developing an architecture to decompose these models into their orbital components, the core of this thesis remains centred on the MUSE model, which provides a robust foundation for the decomposition. However, incorporating both MUSE and SINFONI data into a dynamical modelling will be subject of future work.

4.3.1. Settings

To recreate the gravitational potential of FCC047, I utilized the `DYNAMITE` software, configuring it specifically for this galaxy while incorporating prior knowledge from the literature. Before arriving at the final model, I conducted numerous test runs, initially defining the upper and lower limits of the free parameters more generously to explore the parameter space. The following configuration represents the refined model used in the analysis, with detailed explanations for the settings taken from DYNAMITE [2025b].

Black Hole

The central black hole is modelled using a Plummer potential. The logarithmic black hole mass, $\log M_{\mathrm{BH}}$, was allowed to vary between $[7.0, 8.0]$ with a step size of 0.05. As discussed in Section 4.1.1, the Sphere of Influence of the black hole is unresolved with MUSE observations only, therefore a reliable black hole mass cannot be obtained. Consequently, I could have also fixed its mass to the value obtained by Thater et al. [2023] for the MUSE-only model, as its primary purpose is to serve as a foundation for decomposing the galaxy. The scale length of the black hole potential was fixed at 1×10^{-3} arcsec.

Dark Matter Halo

The dark matter halo follows a spherical NFW profile, with parameters estimated as described in Section 4.1.5 [Navarro et al., 1996]. The concentration parameter was fixed at $C = 6.4$, while the dark matter fraction, expressed as $M_{200}/M_{\star}$, was set to 1.8.

Intrinsic shape parameters

The stellar component is modelled as a triaxial structure, with intrinsic shape parameters translating the projected properties into intrinsic ones. The minor-to-major intrinsic axis ratio, q, spans from 0.05 to 0.90. The intermediate-to-major axis ratio, p, varies within the range $[0.04, 0.90]$, providing insight into whether the galaxy is oblate, prolate, or axisymmetric. Additionally, the ratio between the observed and intrinsic major axis, u, is constrained to $[0.7, 0.9999]$, representing the difference between projected and intrinsic axes. Eventually, these shape parameters need to satisfy the condition $q \leq p < u$ to ensure a physically consistent model.

M/L ratio

The M/L ratio was treated as a free parameter, varying within the range $[0.6, 0.8]$ with a step size of 0.01. The initial value was set to 0.7, serving as a reasonable starting point for the model.

Orbit Library Settings

The orbit library is constructed using three parameters that define the grid for the parameter search and the generation of orbit initial conditions. Each initial condition seeds three orbits: one box orbit and two tube orbits with opposite rotational senses. A tube orbit is described by the three integrals of motion n_E, n_{I2} and n_{I3}. The box orbits are characterized by a binding energy and spherical angles [Thater et al., 2023]. Additionally, a dithering parameter introduces an additional mini-grid of orbits by slightly perturbing the initial conditions to further refine the model. The total number of orbits is determined by:

$$\text{Total Orbits} = 3 \times n_E \times n_{I2} \times n_{I3} \times (\text{dithering}^3) = 343035. \tag{4.7}$$

In this configuration, the number of energy grid points, n_E, is set to 35, while the second and third integrals of motion, n_{I2} and n_{I3}, are both fixed at 11. The dithering parameter is set to 3, producing 3^3 times more orbits, ensuring sufficient resolution in

orbit space. This results in 343.035 orbits in total or in 12.705 so-called orbit bundles. The logarithmic minimum and maximum orbit radii are defined as $\log r_{\min}[kpc] = -2.0$ and $\log r_{\max}[kpc] = 2.2$. Each orbit is integrated for 200 orbital periods, with 50,000 sampling points per orbit.
Figure 4.10 displays the distribution of angular momentum of the orbits in the orbit library, represented by three coloured histograms for the three angular momentum components. The dotted vertical lines show a threshold angular momentum used for orbit classification. This threshold is set to the `DYNAMITE` default value of of $dL = 1 \times 10^{17}$. Given this choice of dL, the classification proceeds as follows:

- If $|L_x| < dL$, $|L_y| < dL$, and $|L_z| < dL$, then it's a box orbit.
- Otherwise, it's a tube orbit, with the largest component of L determining the axis (e.g., if L_z is largest, then it's a short-axis tube orbit).

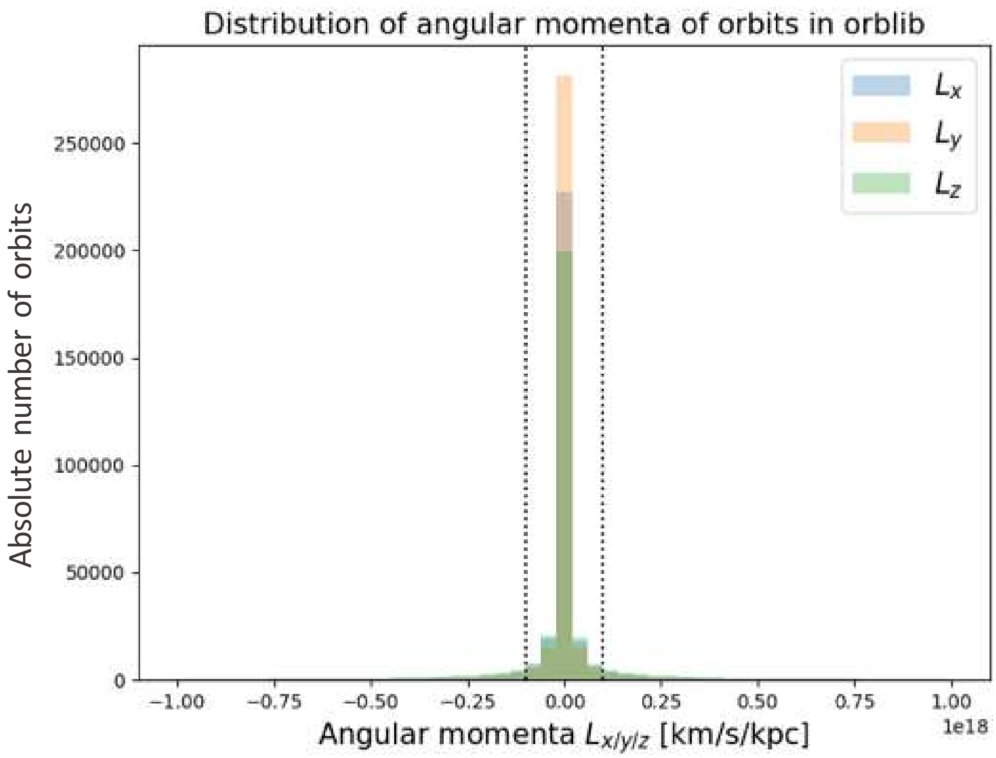

Figure 4.10.: Distribution of angular momentum of the orbits in the orbit library. The dashed line indicates a somewhat arbitrary value that intents to visualize the threshold for classifying tube and box orbits.

Weight Solving

To determine the optimal orbital weights that reproduce best the input data, I employ the `NNLS` (Non-Negative Least Squares) solver, using the `scipy` implementation. The relative errors for luminosity and surface brightness were set to 0.01 and 0.02, respectively, ensuring a robust weight determination.

Parameter Space Exploration

The parameter space of the intrinsic shape parameters was explored using a `FullGrid` approach to avoid local minima while fixing the M/L ratio and the BH mass. Following this, I applied a `LegacyGridSearch` generator and let the BH mass and the M/L ratio free with a $\Delta\chi^2$ threshold of 0.15 and minimum stepsize of 0.1. 1481 models were generated to ensure a thorough exploration of the parameter space with a maximum of 31 iterations.

Multiprocessing Settings

To improve computational efficiency, parallel processing was employed. All available CPUs were utilized for orbit integration, while the weight-solving process was allocated six CPU cores at the VSC-5.

This configuration forms the foundation of the dynamical modelling for FCC047, integrating MUSE kinematics and HST photometry to study its physical and dynamical properties. The settings described above were optimized through extensive testing to ensure that the model accurately represents the system while maintaining computational feasibility.

4.3.2. Best-Fit model

In the following, I describe the Best-fit model found with MUSE data only. The right panel of Figure 4.11 displays the kinematic map of the reduced χ^2_r for the best-fit model compared to the observed LOSVD. This metric is the standard method for assessing model goodness-of-fit and allows for a fair comparison between models with different numbers of data points and free parameters. It is constrained by dividing through the degrees of freedom (dof). The dof are defined as:

$$\mathrm{dof} = N_{\mathrm{spatial}} \times N_{\mathrm{velocity}} - N_{\mathrm{free}}, \tag{4.8}$$

where $N_{\mathrm{spatial}} = 829$ is the number of spatial bins (independent spatial regions where kinematics are measured), $N_{\mathrm{velocity}} = 23$ is the number of velocity bins per spatial bin (corresponding to the number of LOSVD points fitted per spatial element), and $N_{\mathrm{free}} = 2$ represents the number of free parameters in the model. The final model comes from a `LegacyGridSearch`, where the black hole mass and the M/L ratio were the free parameters. For this analysis, dof = 19065. The left panel of Figure 4.11 represents nine selected bins to illustrate the fit quality across a variety of cases. For instance, bin 9 has a well-constrained fit, whereas bins 3 and 4 show slightly poorer fits. Bin 8 serves as an example where the uncertainties were manually set to high values, as this bin was excluded from the analysis due to poor convergence in the MCMC chain (see Section 4.2). The reduced χ_r^2 value of 0.95 suggests a good agreement between the model and the observed LOSVD.

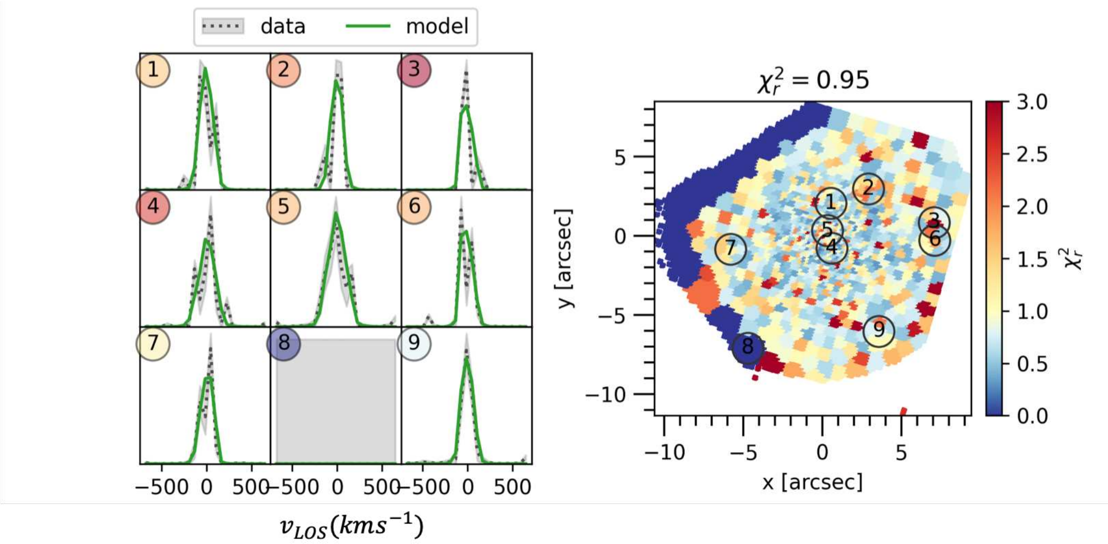

Figure 4.11.: Kinematic map from Best-Fit dynamical model with MUSE-only. The reduced χ_r^2 value of 0.95 suggests a good agreement between the model and the observed LOSVD.

Figure 4.12 presents the kinematic χ^2 plot, illustrating the parameter space exploration during the modelling process. A total of 335 models (highlighted) lie within the 1σ uncertainty interval, while 1481 models fall within the broader 3σ interval. The best-fit parameters derived from the dynamical models are summarized in Table 4.3:

Parameter	Best Fit	1σ Uncertainty	3σ Uncertainty	Unit
M/L	0.64	$^{+0.06}_{-0.04}$	$^{+0.11}_{-0.04}$	$M_\odot/L_\odot$
$M_{\rm BH}$	6.31	$^{+2.60}_{-2.33}$	$^{+2.60}_{-4.53}$	$\times 10^7 M_\odot$
q	0.40	$^{+0.00}_{-0.05}$	$^{+0.00}_{-0.30}$	—
p	0.80	$^{+0.05}_{-0.05}$	$^{+0.10}_{-0.30}$	—
u	0.825	$^{+0.13}_{-0.00}$	$^{+0.17}_{-0.03}$	—

Table 4.3.: Best-fit values for the MUSE-only model with 1σ and 3σ uncertainties.

The best-fit intrinsic shape parameters are $q = 0.4$, $p = 0.8$, and $u = 0.82$, providing

insights into the three-dimensional structure of the stellar component. A value of $q = 0.4$ indicates that the minor-to-major axis ratio is relatively low, suggesting a more flattened shape along the minor axis [Binney and Tremaine, 2008]. The intermediate-to-major axis ratio, $p = 0.8$, is close to unity, suggesting a near-oblate geometry. In this case, the intermediate axis is significantly larger than the minor axis but still smaller than the major axis. However, I compute the Triaxiality parameter $T_{Re} = 0.429$, indicating a triaxial shape following the definition from Santucci et al. [2022]. Finally, $u = 0.82$ implies that the observed major axis is 82% of the intrinsic major axis. This value indicates that the galaxy is not observed perfectly edge-on but is seen under a moderate inclination. The upper and lower uncertainty for q and u, respectively, is zero. No weights have been solved for models with higher values for q and lower values for u due to numerical issues. However, for q the upper limit would have been at most 0.49, as it is restricted by the MGE. The condition $q \leq p < u$ is satisfied.
The stellar M/L ratio now corresponds to the dynamical M/L ratio Y_r. Since a mass map, rather than a surface brightness distribution, was used to construct the MGE, I expect the Y_r to be ≤ 1. In particular, it is expected even lower due to the fact that the model is based on *Bayes-LOSVD* kinematics. Those implications on mass contributions will be discussed further later on. Therefore, the best-fit value of $Y_r = 0.64$ aligns well with my expectations and remains below unity, as anticipated. Thater et al. [2023] find a $Y_r = 0.86 \pm 0.04$ using *pPXF* kinematics.
The best-fit $M_{BH} = 6.31 \times 10^7 M_\odot$ is marginally above the 3σ uncertainty interval of the measurement from Thater et al. [2023], who reported $M_\odot = 4.4^{+1.2}_{-2.1} \times 10^7 M_\odot$, but is well within my 1σ uncertainty. In logarithmic space, the upper uncertainty is 7.74 compared to 7.8 in the present measurement. This agreement is reassuringly close, particularly considering that the MUSE data used here are not expected to resolve the BH's sphere of influence.
In summary, the best-fit model derived from the MUSE data has a triaxial structure, as indicated by the intrinsic shape parameters. The dynamical $Y_r = 0.64$ is consistent with expectations given the use of a mass map, while the black hole mass measurement of $M_{BH} = 6.31 \times 10^7 M_\odot$ aligns well with prior findings despite the limited spatial resolution of the MUSE data. The reduced χ^2_r value of 0.95 confirms a good fit between the model and the observed LOSVD.

Best-fit Orbit distribution

For a comprehensive view of the orbit distribution in FCC047, we classify the orbits based on their rotation axis and their angular momentum, as described in Section 2.5.1. To analyse the orbital structure, we use the projection tensor in `DYNAMITE`, which has dimensions `(4, 24, 28, 12705)`, representing four orbit types, 24 radial bins, 28 circularity bins, and 12,705 orbit bundles. This tensor stores the information about the orbit distribution, and I am adjusting it to my needs. For instance, summing over all radii and circularity bins provides insight into how different orbits are distributed across a bundle in the orbit library (see Figure 4.13 for the orbits within 200kpc). Due to dithering >1, a single bundle can contain a mix of orbits.

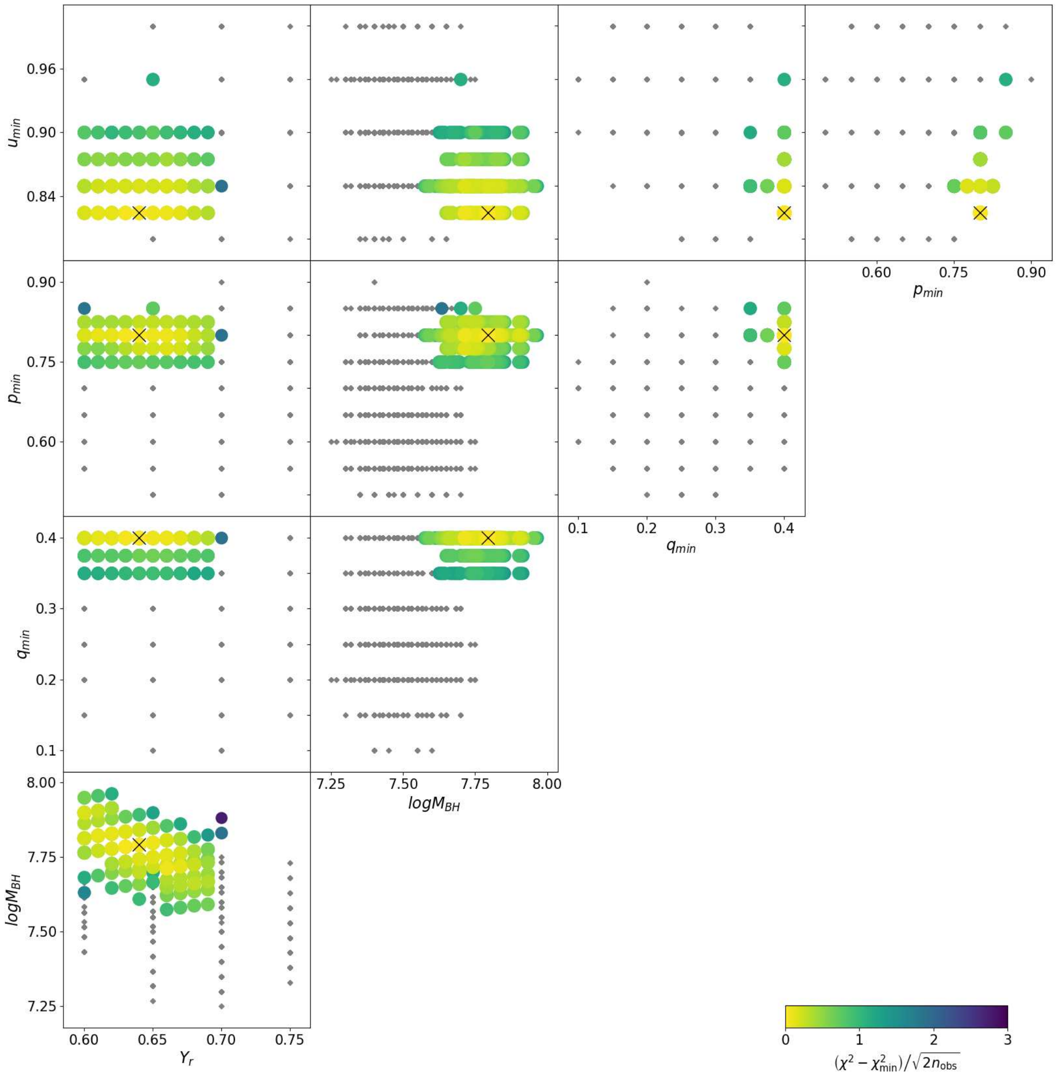

Figure 4.12.: Kinematic χ^2 plot: Each point denotes a model, colour coded by the reduced χ^2 as indicated in the colorbar. The best-fit value of each parameter is marked by a black cross.

To investigate the best-fit orbit distribution, I compute the dot product of the projection tensor with the orbital weights (which have the shape `(4, 24, 28)`). The best-fit model reveals the following orbit distribution:

- **Long-axis tubes** (λ_x): 25.3%

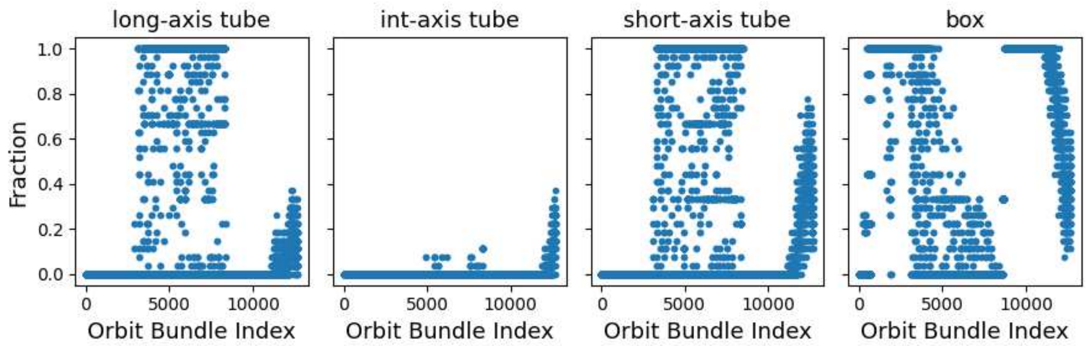

Figure 4.13.: Fraction of different orbit types per orbit bundle within 200kpc.

- **Intermediate-axis tubes** (λ_y): 1.2% [3]
- **Short-axis tubes** (λ_z): 69.1%
- **Box orbits** (λ_{tot}): 4.4%

The dominance of tube orbits, particularly short-axis tubes, is expected in triaxial potentials. Tube orbits are associated with stable, regular motion around a principal axis, compared to chaotic box orbits, which do not conserve any component of angular momentum and fill a two-dimensional region (box) in phase space [Bovy, 2023]. Short-axis tubes, in particular, dominate because they conserve angular momentum around the short axis, ensuring stability and a more ordered phase space structure [Binney and Tremaine, 2008]. The negligible contribution of intermediate-axis tubes is also consistent with theoretical expectations, as such orbits are known to be unstable and are not sustained in realistic galactic potentials [Binney and Tremaine, 2008]. Hence, the high fraction of tube orbits aligns well with the dynamical structure expected for FCC047 and its nuclear star cluster.
An orbit distribution is typically visualized in the phase space of circularity L_z (or L_x) versus intrinsic radius [Zhu et al., 2018]. Theoretical considerations are discussed in Section 2.5.2. Figure 4.14 shows the circularity distribution of the tube orbits along the minor z-axis within $r = 2''$. The color bar indicates the orbital weights. What immediately stands out is the significant fraction of hot orbits around $L_z \approx 0$, indicative of random motion. This is a characteristic feature of early-type galaxies, and represent pressure-supported motion with little to no net angular momentum [Santucci et al., 2022]. Additionally, a notable fraction of counter-rotating orbits is observed within $1''$, appearing kinematically decoupled from the rest of the system.
Figure 4.15 provides a broader view of the orbital distribution. The left panel shows the distribution up to $\approx 25''$, while the right panel extends further, showing up to $\approx 60''$.

[3] Tube orbits along the intermediate axis are not stable and do not exist in reality [Bovy, 2023].

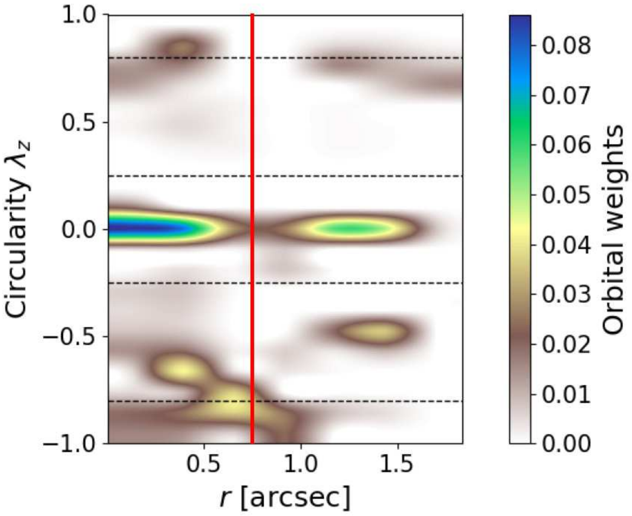

Figure 4.14.: Orbit distribution around the minor z-axis within $r = 2''$, revealing substantial counter-rotating motion towards the centre. The red line indicates 1 $R_{\mathrm{eff,NSC}} = 0.74''$.

The dominance of hot orbits persists until $\approx 15''$, corresponding to approximately 0.5 R_{eff}. Within this region (up to $15''$), many warm and some cold prograde orbits (rotating in the direction of the galaxy's spin) are also present. In the outer regions, up to $60''$, the orbital distribution broadens, with contributions from orbits spanning a range of circularities (L_z). Notably, the structure changes at $\sim 1R_{\mathrm{eff}}$. Beyond this radius, there is an increased contribution from mildly prograde orbits.

To compare this with motion around the major x-axis, Figure 4.16 presents the circularity distribution up to an intrinsic radius of $2''$ (left) and $20''$ (right). Hot orbits are clearly dominating the distribution around the x-axis. The counter-rotating features as well as dynamically cold and warm contributions observed along the z-axis are not prominent along the x-axis.

Summarized, the best-fit dynamical model of FCC047 reveals a complex orbit structure, dominated by hot tube orbits, as expected for early-type galaxies [Santucci et al., 2022]. Counter-rotating orbits within $1''$ suggest a kinematically decoupled core (KDC). The orbital structure changes beyond 1 R_{eff}, with a growing contribution from mildly prograde orbits, indicating an extended outer component. Comparing orbit distributions along the z- and x-axes provides a deeper understanding of the galaxy's dynamical structure and a multidimensional view of FCC047 and its NSC.

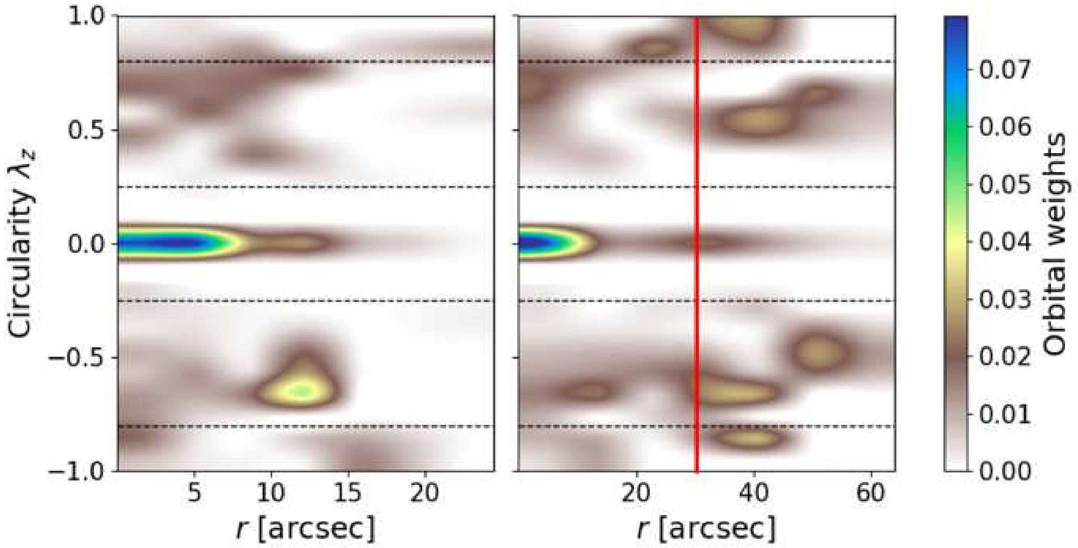

Figure 4.15.: Orbit distribution around the minor z-axis within $r = 20''$ and $r = 60''$. The red line indicates 1 $R_{\mathrm{eff}} = 30''$.

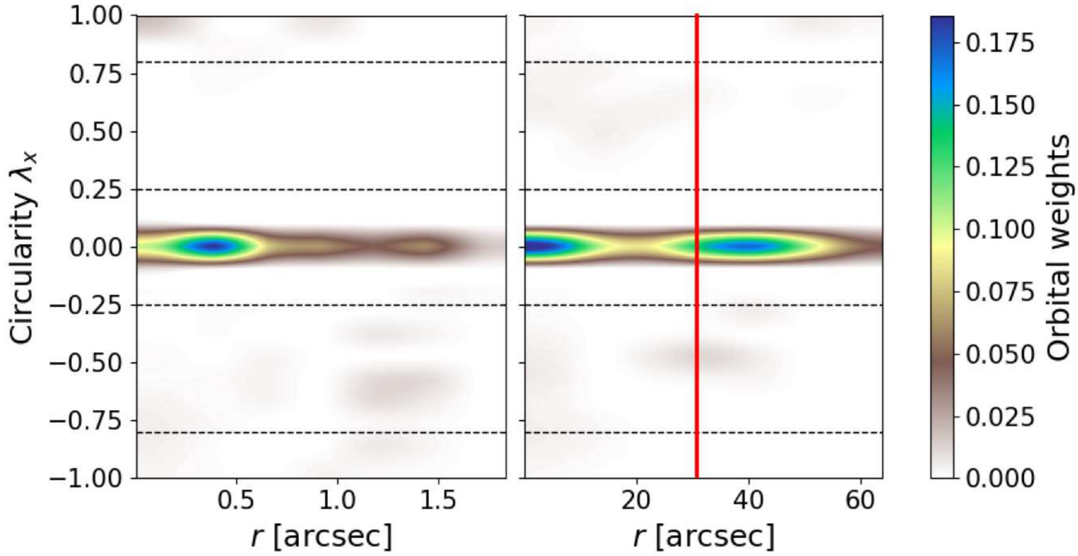

Figure 4.16.: Orbit distribution around the major x-axis within $r = 2''$ and $r = 20''$. The red line indicates 1 $R_{\mathrm{eff}} = 30''$.

4.4. Decomposition

This section describes the decomposition of FCC047 into different dynamical components and the calculation of their individual kinematics for further analysis. The decomposition method follows recent advances in dynamical decomposition techniques. Santucci et al. [2022] applied Schwarzschild models to a sample of galaxies from the SAMI Galaxy Survey, finding correlations between stellar mass and internal orbital structures, with massive galaxies having a higher fraction of hot orbits. With the initial assistance of Giulia Santucci, I developed a full decomposition routine that is structured as:

1. Best-fit orbit-library (including LOSVD histograms and projected masses) is read from the dynamical modelling outputs
2. Orbit libraries are analysed to classify the orbits based on their angular momentum around a particular axis. The components are defined using the same cuts as described in Section 2.5.2.
3. Orbits are multiplied with their weights
4. LOSVD, which initially has the shape $(n_{orbits}, n_{velocitybins}, n_{apertures})$ are summed up over all orbits to gain a spatial velocity distribution
5. Resulting LOSVD histograms are used to re-calculate the kinematic properties (e.g. v, σ) of the individual components including higher-order moments per aperture
6. Flux contribution per component is computed
7. Plots and histograms are generated to illustrate the orbital structure

Besides developing my own routine, I refined and extended the `DYNAMITE` Decomposition routine. This routine facilitates the kinematic extraction based on Gaussian-fits to the LOSVD histograms, which will serve as a comparison to the kinematic extraction via the mean/sigma of histograms directly as I've used in my routine.

4.4.1. Best-Fit Model

The following figures provide an overview of the decomposition of the best-fit dynamical model derived from MUSE data with the routine developed for this thesis. Figure 4.17 shows the number of orbits per component that contribute to the potential within the $15'' \times 15''$ spatial extent. Orbits with zero weight are excluded, and the same classification cuts as described in Section 2.5.2 are applied. It is important to note that these orbits are not confined to this spatial extent, as they do not maintain a constant radius. Instead, they contribute to the potential across the entire modelled region. The distribution of orbits varies significantly across components, with certain orbital types dominating. In total, 447 orbits have non-zero weight. The majority of these orbits are hot (259 along the z-axis, 346 along the x-axis) with almost no angular momentum around the

z-axis, a characteristic feature of an early-type galaxy like FCC047 [Santucci et al., 2022]. Additionally, the presence of counter-rotating orbits is evident. The best-fit model reveals 39 dynamically cold and 64 warm counter-rotating orbits along the z-axis, and 26 dynamically cold and 31 warm counter-rotating orbits along the x-axis. This distribution aligns with the orbit distribution seen in phase-space of circularity L_z and L_z vs. intrinsic radius, as illustrated in Figure 4.14 and Figure 4.16.

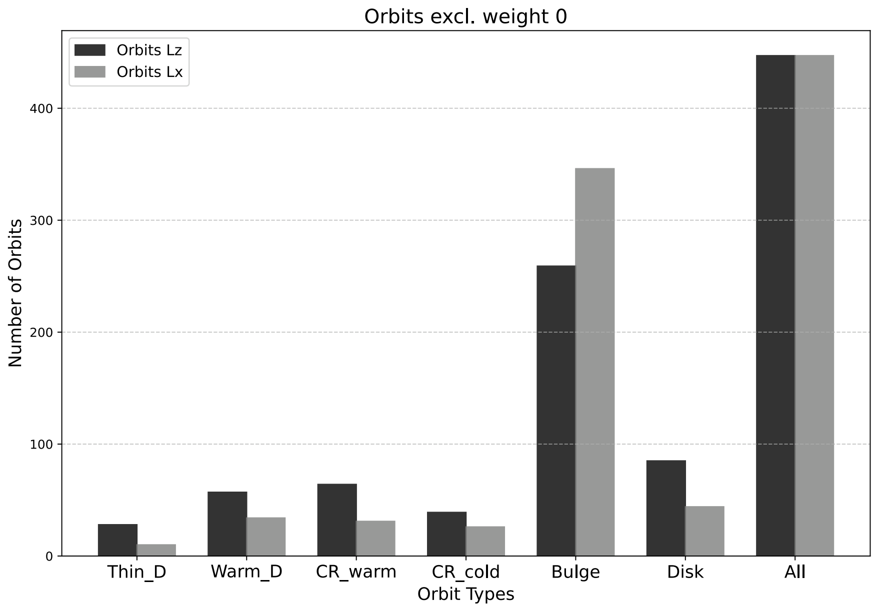

Figure 4.17.: The distribution of orbits included in the best-fit model, excluding those with zero weight. Only orbits contributing within a $15'' \times 15''$ spatial extent are shown.

Figure 4.18 presents the orbital decomposition based on the L_z circularity value of the best-fit model. The rows correspond to the individual dynamical components, while the columns (from left to right) represent the flux contribution, the re-calculated velocity [km/s] and velocity dispersion [km/s] derived from the mean and sigma of the LOSVD histograms, and the ratio of velocity to velocity dispersion $|v|/\sigma$, which serves as an indicator of ordered to random motion:

- **Cold:** This component is characterized by high rotation, with a pronounced velocity peak at $v_{max} = 60.4$ km/s. Interestingly, it also exhibits a relatively high central velocity dispersion of $\sigma_{max} = 85.6$ km/s. The flux contribution is strongest in the centre, with a luminosity fraction of $\approx 11.1\%$.
- **Warm disk:** The warm disk has lower angular momentum than the cold disk and extends further out, leading to a luminosity fraction of $\approx 21.5\%$. It reaches a maximum velocity of $v_{max} = 47.1$ km/s and a peak velocity dispersion of $\sigma_{max} = 79.3$

km/s. Notably, the "Disk" component (row 6) represents the sum of the warm and cold components, resulting in a total luminosity fraction of approximately 32.5%.

- **Counter-rotating (Cr) components:** The counter-rotating warm and cold components appear at negative L_z, forming a distinct kinematic subpopulation:
  - **Cr warm:** This component peaks in flux at the center but extends to larger radii, contributing a luminosity fraction of about 23.4%. The velocity dispersion peaks in the centre at $\sigma_{max} = 96.1$ km/s and then spreads into a broad distribution. The maximum velocity reaches $v_{max} = 43.4$ km/s, comparable to its non-counter-rotating counterpart.
  - **Cr cold:** This component is highly concentrated in the nucleus, exhibiting strong rotation and a peak velocity dispersion of $\sigma_{max} = 78.7$ km/s, although lower than that of the non-counter-rotating cold disk. The maximum velocity reaches $v_{max} = 62.1$ km/s, similar to its non-counter-rotating counterpart. The luminosity fraction is approximately 6.6%.
- **Hot:** The hot orbits have very high velocity dispersion, peaking at $\sigma_{max} = 103.4$ km/s, with a wide range of velocities and a relatively low maximum velocity of $v_{max} = 19.9$ km/s. The flux contribution is approximately 37.4%. Notably, in the nucleus, the velocity map reveals clear rotation in the opposite sense to the overall motion of the main body. It is important to note that I used the L_z cuts, as is commonly done in the literature. Alternatively, one could consider increasing the cut between hot and counter-rotating warm orbits to increase the population of the counter-rotating warm component.
- **Overall structure:** The counter-rotating orbits are concentrated in the centre, indicating a dynamically complex nuclear region. Overall velocities are lower than those of individual components due to orbit cancellation effects. The peak velocity dispersion is $\sigma_{max} = 94.1$ km/s. Furthermore, the total luminosity fraction of 100% confirms the validity of the decomposition.

I show the measured velocity extrema and maximum velocity dispersions for the individual components in Table 4.4. To estimate the uncertainties in the kinematics, I selected models with the largest deviation in M_{BH} while keeping the intrinsic shape parameters and Y_r fixed to the best-fit values. By decomposing the models with the highest and lowest M_{BH}, I found no significant deviations in the recalculated kinematics for most components. However, for the model with the highest $M_{BH} = 7.07 \times 10^7 M_{\odot}$, the dynamically cold and warm components showed velocity differences of up to 0.083 km/s and 0.037 km/s, respectively. Similarly, for the velocity dispersion, I found deviations of 0.0795 km/s and 0.0550 km/s, respectively. To further test the robustness of my measurements, I decomposed the ten best models with the lowest χ^2_{kin} values. The results were consistent with those from the models with the largest M_{BH} deviations from the best-fit. Again, most components showed no deviations in the kinematic recalculations. However, for the dynamically cold and warm components, I found maximum velocity differences of 0.0368 km/s and 0.0164 km/s, respectively. The corresponding maximum dispersion deviations were 0.0353 km/s and 0.0244 km/s. These minimal or even negligible deviations are expected, given that these models are closely aligned with the best-fit. Furthermore, I decomposed a model that lies outside the 3σ confidence interval, with parameters that strongly differ from the best-fit model: $M_{\rm BH} = 1.78 \times 10^7 M_\odot$, $q = 0.2$, $p = 0.6$, $u = 0.95$, and $Y_r = 0.7$. Here, I found significantly larger deviations in both velocities and dispersions across all components. For example, velocity deviations reached up to 129.982 km/s in certain spatial bins for the (counter-rotating and non-counter-rotating) dynamically cold component. Similarly, the maximum dispersion deviation for the warm component was 22.23 km/s. The kinematic patterns reveal complex variations in the $|v|/\sigma$ ratio, highlighting the interplay between dynamically distinct components. Notably, the rotation axis of cold and warm orbits shifts by approximately 15°. The rotation axis of the hot orbits, which appear counter-rotating in the nucleus, aligns closely with that of the counter-rotating warm component.

Flux is typically measured in physical units of erg/s/cm^2/arcsec^2, which represents the energy received per second per unit area and per unit solid angle. However, to describe brightness in a way that aligns with human perception and observational data, flux is often expressed on a logarithmic scale. Surface brightness in magnitudes (mag/arcsec^2) is a logarithmic scale that expresses relative brightness, making it easier to compare objects with vastly different luminosities. In `DYNAMITE`, we do not scale the surface brightness by -2.5, instead, the model maintains a direct logarithmic representation of surface brightness without this scaling factor. To convert it to proper magnitudes, additional adjustments and calibrations would be required, but here, I focus solely on comparing different flux contributions. The fractional contribution of light by different components is shown in Table 4.4.1. Counter-rotating cold orbits contribute about 6.6% of the flux, predominantly concentrated in the nucleus. The counter-rotating warm orbits extend further outward and, when considering a spatial extent of $15'' \times 15''$, contributing with 23.4% to the total luminosity along the $z-$axis. The hot orbits, including a significant fraction of counter-rotating hot orbits, contribute 37.4%.

Comp.	max $\lvert v_x \rvert$	max $\lvert v_z \rvert$	max σ_x	max σ_z	max $\lvert v_x \rvert/\sigma_x$	max $\lvert v \rvert_z/\sigma_z$
Cold	93.9	60.4	92.4	85.6	5.87	1.86
Warm	70.8	47.1	75.3	79.3	1.97	0.98
Cr warm	70.2	43.6	92.5	96.1	1.71	0.96
Cr cold	87.2	62.1	94.7	78.7	5.79	2.90
Hot	10.1	19.9	94.9	103.4	0.19	0.25
Disk	70.2	49.9	81.5	82.0	1.95	1.14
All	8.5	8.5	94.1	94.1	0.21	0.18

Table 4.4.: Kinematic properties (v, σ) and maximum absolute velocity to velocity dispersion ratios $(|v|/\sigma)$ for individual components. The absolute maximum velocities are reported, as the model is point-symmetric.

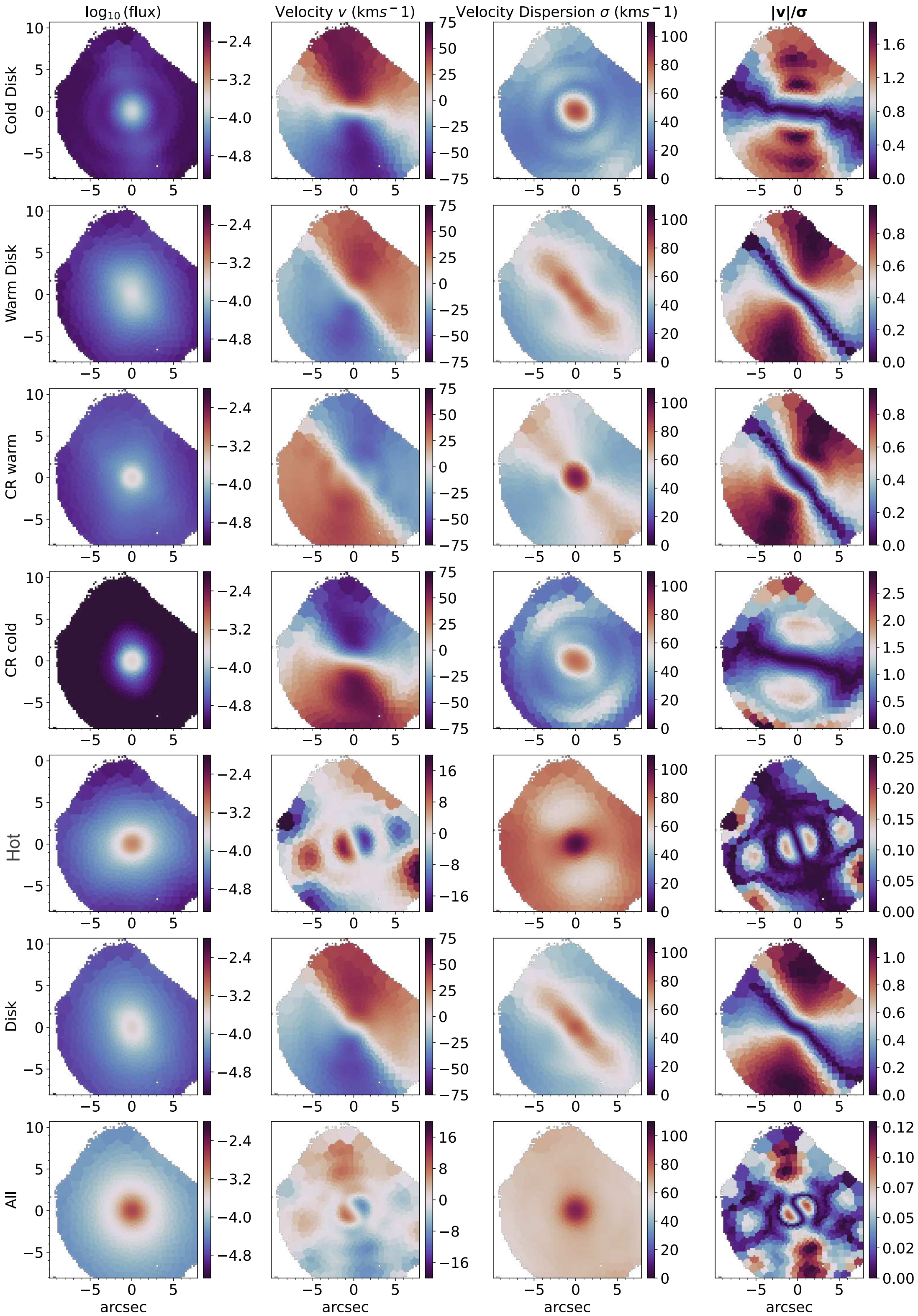

Figure 4.18.: Orbital decomposition of the best-fit mode along the minor $z-$axis.

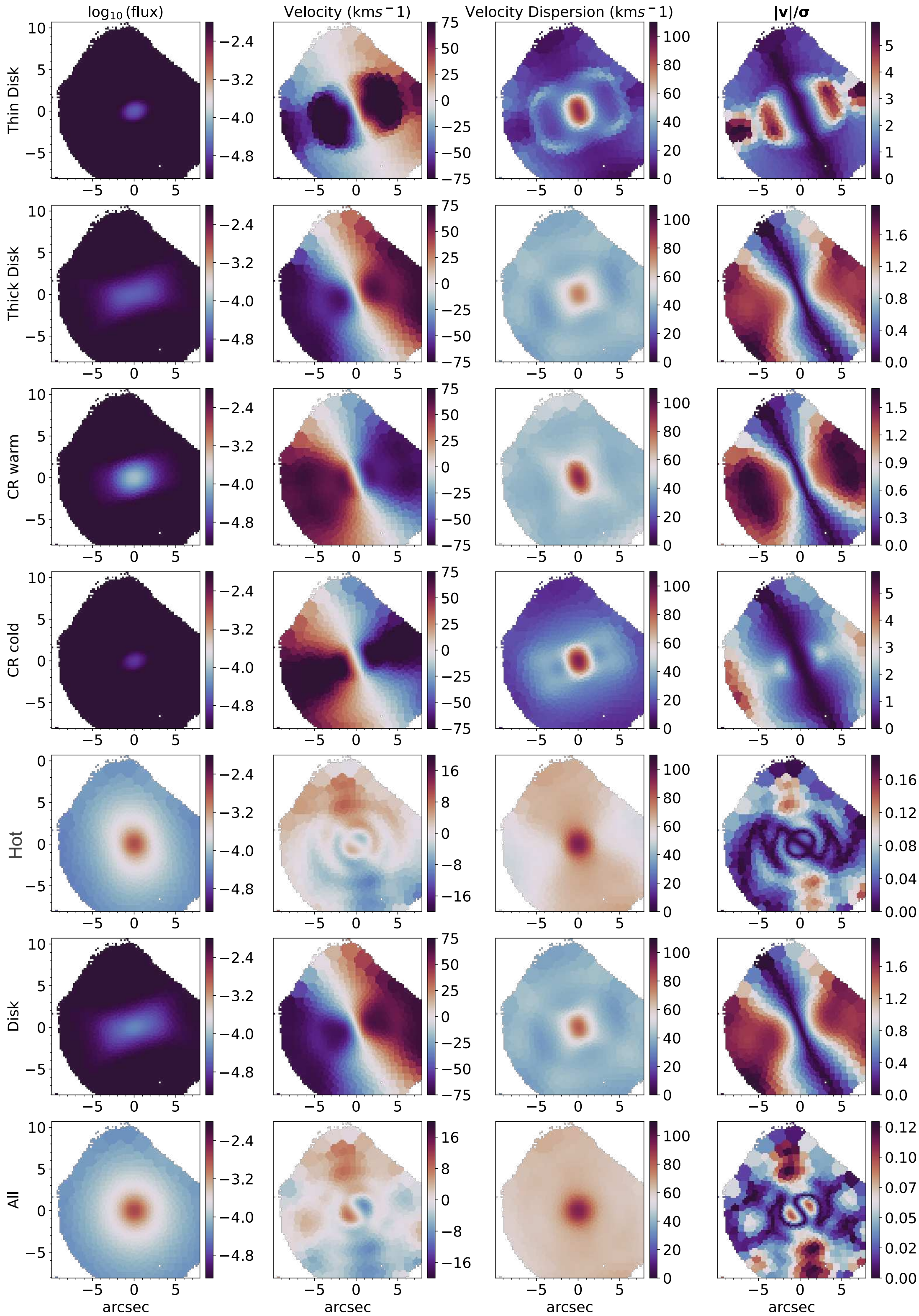

Figure 4.19.: Orbital decomposition of the best-fit mode along the $x-$axis.

Component	Thin D	Warm D	Cr warm	Cr cold	Hot	Disk	All
Lum. fraction L_x	0.007	0.038	0.039	0.007	0.909	0.045	1.000
Lum. fraction L_z	0.111	0.215	0.234	0.066	0.374	0.326	1.000

Table 4.5.: Luminosity contributions along L_x and L_z for the individual components within $15'' \times 15''$.

To complement the analysis along the minor z-axis, Figure 4.19 provides an insight into the orbital decomposition along the major x-axis, offering an additional perspective on the dynamically distinct components. A striking difference compared to the L_z plot is the change in rotation axis, which is expected as we are now observing the motion around a different axis. The flux contribution is overwhelmingly dominated by hot orbits with low angular momentum, contributing nearly all the flux, consistent with the orbit distribution and the high luminosity fraction of 90.9%. An interesting feature is the "whirl" pattern observed within the flux map of the hot orbits, which is also clearly reflected in the "all" component, suggesting a coherent dynamical structure. As in the L_z analysis, the hot component reveals clear counter-rotating motion in the nucleus. The velocity dispersion shows a prominent peak at the centre, as expected with peak values of $\sigma_{max} = 94.871$ km/s. Although small, there is still some flux contribution from the counter-rotating warm component with a luminosity fraction of 3.9%, indicating its presence even along the x-axis. The extrema in velocity and maximum velocity dispersion for the components along the $x-$axis are shwon in Table 4.4.

In summary, the orbital decomposition of the best-fit model reveals a complex interplay of components with the hot orbits as the dominant structure, high dispersion, and flux contribution. The kinematic properties of the defined counter-rotating orbits suggest highly complex dynamics in the galaxy's nucleus. The nucleus seems kinematically decoupled due to the significant fraction of counter-rotating orbits. The presence of these orbits, including the hot orbits with negative l_z/l_x, suggests a dynamically complex formation history, possibly influenced by past mergers or external accretion events.

4.4.2. Closer look at the counter-rotating components

In this section, I examine the counter-rotating components in greater detail. Since they appear to be predominantly concentrated in the galaxy's nucleus, consistent with the interpretation of the stellar kinematics and the findings of Thater et al. [2023], which suggest that this structure corresponds to the dynamical configuration of the NSC. The counter-rotating cold component has distinct kinematic features, as shown in the left panel of Figure 4.20. It displays clear signs of rotation and a remarkably high velocity dispersion for a dynamically cold structure [Zhu et al., 2017]. The right panel of Figure 4.20 shows the counter-rotating warm component, demonstrating a more complex kinematic pattern with higher velocity dispersion and less coherent rotation. To further investigate the kinematic properties of these components, I measured the higher-order Gauss-Hermite moments, h_3 (skewness) and h_4 (kurtosis), by performing a non-linear least squares Gauss-Hermite fit on the LOSVD histograms. The theoretical background of these moments is discussed in Section 2.6.1. Uncertainties in h_3 and h_4 are estimated using a residual function to measure the difference between the fit and the dynamical model output. Some of the structures found are very subtle corresponding to a smaller spatial extent than the MUSE resolution and must therefore be treated with caution. Notably, the anti-correlation between the velocity maps and the h_3 maps is visible, at least for the inner region where the components have significant flux contribution.

The h_3 moment quantifies the asymmetry of LOSVD. In the Cr Cold component, the h_3 values are significantly larger compared to the warm component, indicating a highly asymmetric LOSVD. In contrast, the Cr Warm component shows notably lower h_3 values, reflecting a more Gaussian-like LOSVD. Warm orbits, with their higher velocity dispersion, smooth out such asymmetries.

The h_4 moment characterizes whether the LOSVD is more peaked (positive h_4) or flat-topped (negative h_4) compared to a Gaussian distribution. For the Cr Cold component, the h_4 moment shows a complex pattern. A ring-like structure with large positive and negative h_4 values appears in layers around the nucleus at a radius of $\sim 1.5''$ up to $\sim 5.5''$. In the Cr Warm component, there is an overall dominance of negative h_4 values. Warm orbits, being more pressure-supported with lower angular momentum, have a broader velocity spread, which smooths out peaking effects and results in a more flat-topped LOSVD. In contrast, the cold component has a more confined velocity range (smaller range of velocity dispersion), resulting in a more peaked LOSVD and thus higher (negative and positive) h_4. However, these findings should be treated with caution, as the flux contribution is predominantly concentrated in the central regions, particularly for the counter-rotating cold component. This is also reflected in the increasing errors at larger radii.

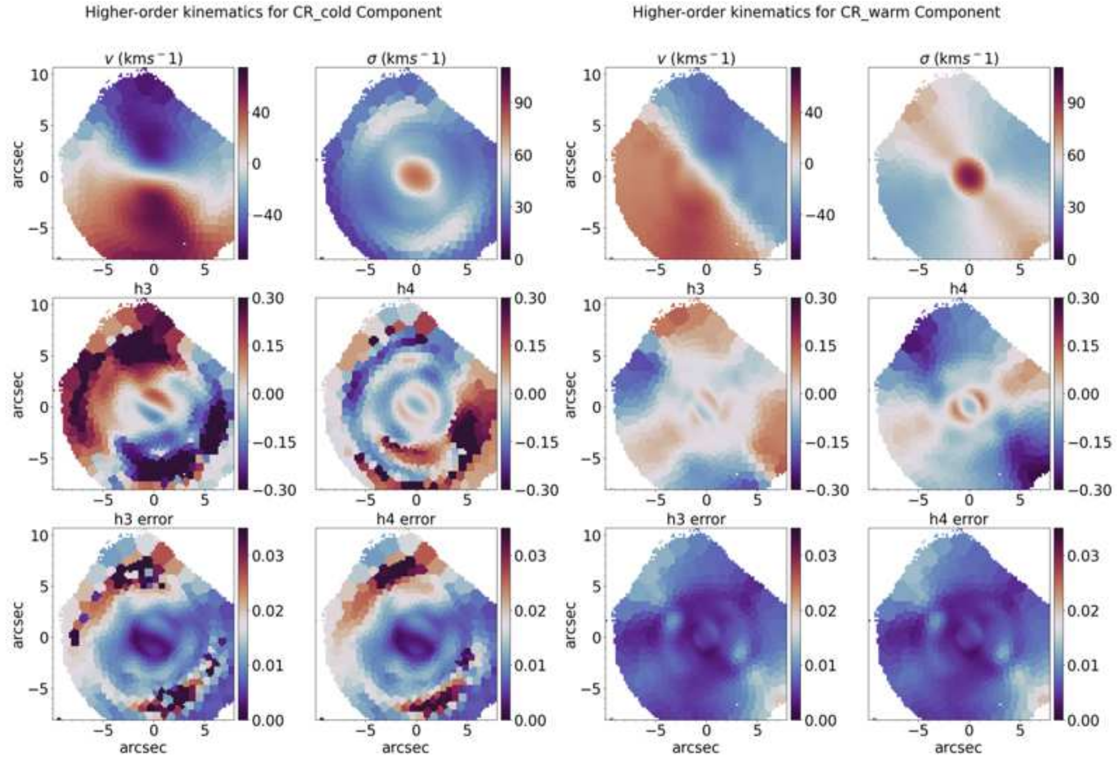

Figure 4.20.: Higher-order kinematics of the cold and warm counter-rotating components with error estimates using the L_z decomposition.

4.4.3. Decomposition of the SINFONI kinematic set from the best-fit model from Thater et al. [2023] with DYNAMITE

Thater et al. [2023] modelled the galaxy FCC047 with MUSE data complemented by SINFONI high-resolution observations. Since this model dates back to 2023, some adjustments were necessary in the DYNAMITE code to enable reprocessing. Furthermore, I extended and refined the DYNAMITE decomposition routine, and then applied it to the SINFONI kinematic set. Figure 4.21 displays the inner $3'' \times 3''$ region of FCC047 separated into its distinct dynamical components based on the same cuts in L_z as above. The first column represents the flux contribution, the second shows the velocity maps, and the third column represents the velocity dispersion maps. The rows correspond to the individual components, analogous to the decomposition of the MUSE model. It is important to note that Thater et al. [2023] measured a black hole mass of $M_{\rm BH} = 4.4^{+1.2}_{-2.1} \times 10^7 M_\odot$, whereas my best-fit model, based solely on MUSE data, yields $M_{\rm BH} = 6.31^{+2.60}_{-2.33} \times 10^7 M_\odot$, which is 43.4% higher. This discrepancy could certainly influence the orbit distribution and therefore the distinct dynamical components observed.
When comparing luminosity fractions, while keeping in mind that the SINFONI model shows only the inner $3'' \times 3''$ region , notable differences emerge. The SINFONI decomposition reveals a significantly lower cold disk luminosity contribution of approximately 1.2%, compared to 11.1% in the MUSE model, indicating a less prominent thin disk component. Additionally, the counter-rotating warm component contributes 23.4% in the MUSE model but only 4.79% in the SINFONI model, suggesting a stronger presence of warm counter-rotating orbits in the former. Similarly, the counter-rotating cold component is less significant in the SINFONI model (0.78%) than in the MUSE model (6.6%), implying a less distinct nuclear disk structure. In contrast, the hot orbits dominate the SINFONI model with a luminosity fraction of 82.82%, compared to 37.4% in the MUSE model, reinforcing the idea that hot orbits play an even more dominant role in the SINFONI decomposition. The primary counter-rotating motion appears to be associated with hot orbits with negative l_z.
The SINFONI model has overall higher velocity peaks in all components, that point towards the presence of an SMBH, which is slightly lower in my MUSE-only model. The maximum velocity dispersion for the hot component is significantly higher in the SINFONI model ($\max\sigma_{hot} = 113.8\,\mathrm{km/s}$) compared to the other model ($\max\sigma_{hot} = 103.4\,\mathrm{km/s}$), further supporting the notion that the hot component dominates the central kinematics in the SINFONI decomposition. Furthermore, the rotation axis appears tilted similarly to that in the MUSE model, though not identically.
The difference in luminosity fractions, velocity peaks and dispersion extrema may stem from the different approaches in kinematic extraction method: the MUSE model utilizes *Bayes-LOSVD* kinematics, which is particularly effective in recovering the LOSVD in multi-component systems and on small physical scales, such as the NSC. Unlike *pPXF*, which fits a Gauss Hermite series, *Bayes-LOSVD* allows for a more flexible representation of multi-peaked LOSVDs, characteristic of a system with multiple dynamical components. In general, *pPXF* tends to produce broader velocity distributions compared to *Bayes-LOSVD* (see Figure 4.8), which can lead to higher inferred velocity dispersions and,

consequently, greater mass contributions in dynamical models. This effect may explain why the dominance of hot orbits is even more pronounced in the SINFONI decomposition.

Component	max $\|v\|$	σ_{max}	Lum. Fraction
Thin Disk	82.9	65.0	0.0123
Thick Disk	30.7	106.4	0.1038
Disk	46.1	101.8	0.1161
Cr cold	81.2	72.9	0.0078
Cr warm	68.8	82.6	0.0479
Hot	39.8	113.8	0.8282
All	35.7	103.7	1.0000

Table 4.6.: Maximum absolute velocities as the model is point-symmetric, maximum sigma, and luminosity fractions of the dynamically decomposed components from SINFONI data.

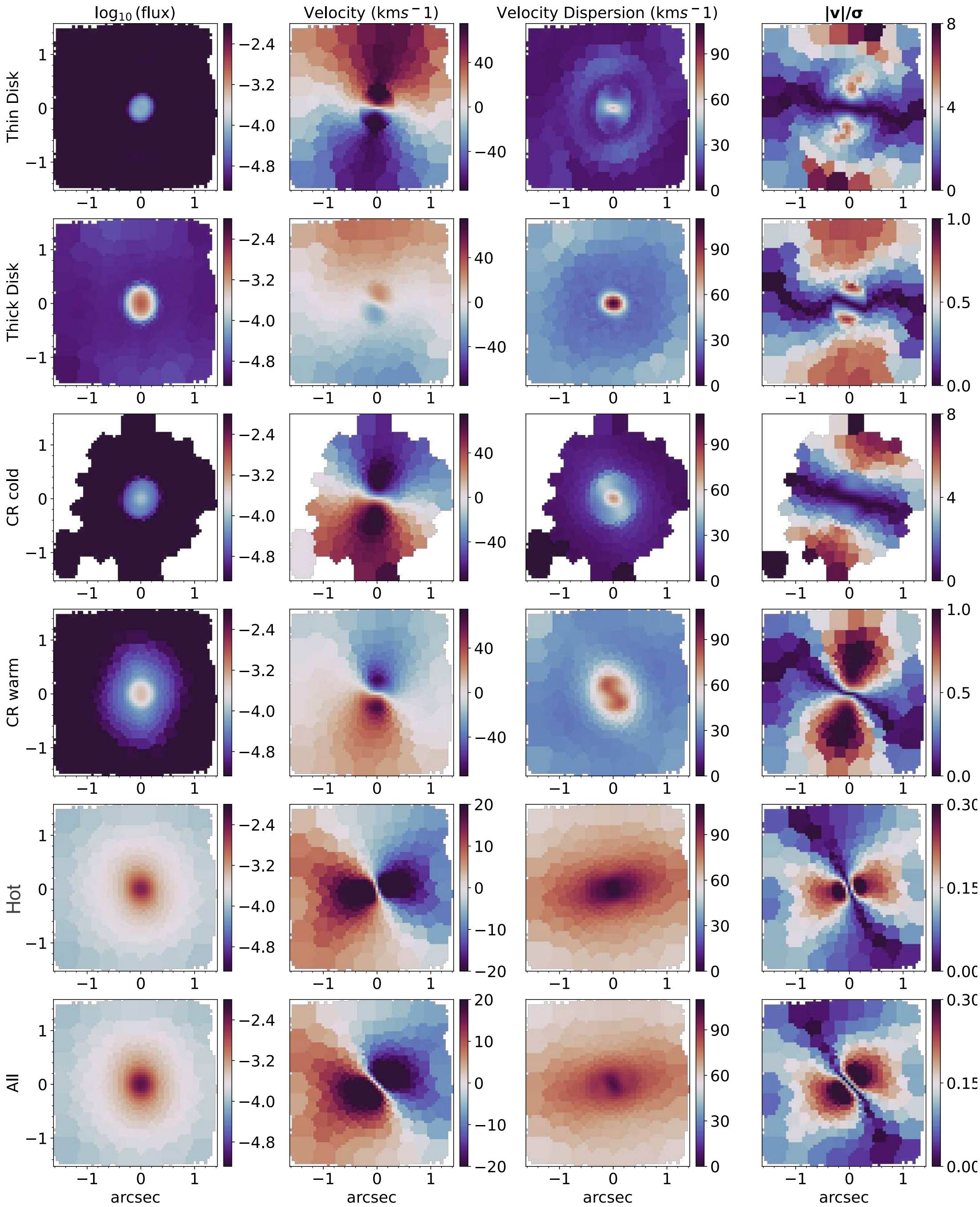

Figure 4.21.: Dynamical decomposition of the inner $3'' \times 3''$ region of FCC047 based on the SINFONI data. The first column represents the flux contribution, the second column the velocity maps, and the third column the velocity dispersion maps for each component.

5. Conlusion and Outlook

5.1. Results

This study focused on the "Orbital Decomposition of the Nuclear Star Cluster in the Early-Type Galaxy FCC047", utilizing the Schwarzschild orbit-superposition method within the `DYNAMITE` framework. The primary objective was to decompose the NSC into its dynamically distinct components and analyse its formation history based on its orbital structure and angular momentum distribution. Separating the NSC as a physically distinct entity proved to be challenging, as `DYNAMITE` operates with an average radius rather than strictly confined spatial boundaries. In this framework, each orbit contributes throughout the model space, meaning that no orbits are exclusively contained within the NSC's effective radius of $R_{\text{eff}} = 0.74''$. Implementing a method to assign specific radii to orbits could be feasible, but it would require extensive discussion, testing, and technical development - potentially forming the basis for future research.

Despite this limitation, I successfully decomposed the galaxy FCC047 in its dynamically distinct components and analysed a spatial region of $15'' \times 15''$ based on a Schwarzschild model using MUSE data and *Bayes-LOSVD* kinematics. The stellar kinematics revealed a triply peaked LOSVD in bin number 0, which, by definition of the binning routine, corresponds to the bin with the highest S/N. This bin aligns with the galaxy's nucleus, as shown in Figure 4.8. The presence of a counter-rotating subpopulation in the galaxy's nucleus was already evident during the kinematic extraction step. The derived best-fit Schwarzschild model achieved a $\chi^2 = 0.95$, indicating a strong agreement between the model and the observed LOSVD. I measure a $M_{\text{BH}} = 6.31^{+2.60}_{-2.33} \times 10^7 M_\odot$, that aligns well with prior findings despite the limited spatial resolution of the MUSE data, and a dynamical $\Upsilon_r = 0.64^{+0.06}_{-0.04}$.

The best-fit orbit distribution reveals a dominance of tube orbits, in particular short-axis tube orbits with 69.1%. This is consistent with expectations for triaxial potentials [Bovy, 2023]. Regarding the orbit distribution in phase space of intrinsic radius and circularity L_z highlights two key features: A significant fraction of hot orbits is counter-rotating within $1''$, which is consistent with the effective radius of the NSC, $R_{\text{eff,NSC}} = 0.74''$, as shown in Figure 4.14. Additional counter-rotating motion can be attributed to a counter-rotating cold disk and a counter-rotating warm structure. Beyond 1 R_{eff}, the orbital structure shifts, with an increased contribution from mildly prograde orbits, which could be an outer galaxy disk, that might be another distinct dynamical component reaching further out than the $15'' \times 15''$ FoV (see Figure 4.15). When examining the orbit distribution along the major $x-$axis, the dominance of hot orbits is evident (see Figure 4.16). The boundaries for circularity values along the minor $z-$axis were defined based on literature values, such as those in Santucci et al. [2022], Zhu et al. [2018], and Zhu et al. [2017]. Decomposing the MUSE model along L_z revealed a total of 444 orbits with weights larger than 0, including 39 counter-rotating cold, 64 counter-rotating warm and 259 hot orbits. The results of the decomposition (see Figure 4.18) are summarized as follows:

1. **Cr cold:** This component is highly concentrated in the nucleus, having strong rotation with a peak velocity dispersion of $\sigma_{max} = 78.7$ km/s and a maximum velocity of $v_{max} = 62.2$ km/s. It contributes approximately 6.6% of the total luminosity.

2. **Cr warm:** This component peaks in flux at the centre but extends to larger radii, contributing about 23.4% of the total luminosity. The velocity dispersion peaks at $\sigma_{max} = 96.1$ km/s in the centre and broadens at larger radii, with a maximum velocity of $v_{max} = 43.4$ km/s.

3. **Hot:** The hot orbits have very high velocity dispersion, peaking at $\sigma_{max} = 103.4$ km/s, with a wide range of velocities and a relatively low maximum velocity of $v_{max} = 19.9$ km/s with 37.4% flux contribution. Notably, in the nucleus, the velocity map reveals clear rotation in the opposite sense to the overall motion of the main body, suggesting a significant fraction of counter-rotating hot orbits.

To complement the kinematic analysis for the individual components, I measured higher-order moments by performing a non-linear least squares Gauss-Hermite fit on the LOSVD histograms, see Figure 4.20. The anti-correlation between the velocity maps and the h_3 maps is visible in the central regions, where the flux peaks. However, the structures are very subtle corresponding to a smaller spatial extent than the MUSE resolution and must therefore be treated with caution. A key distinction between the two counter-rotating components is that the cold component has significantly larger values in both h_3 and h_4. The strong signal in h_3 is expected, because dynamically cold orbits are predominantly rotation-supported, leading to a pronounced skewness. In contrast, warm orbits, with their higher velocity dispersion, smooth out such asymmetries. The cold component has a more confined velocity range (smaller range of velocity dispersions), resulting in a more peaked LOSVD and thus stronger h_4. Meanwhile, warm orbits span a broader range of velocities, leading to a more flat-topped LOSVD.
Additionally, I analysed a smaller spatial region of $3'' \times 3''$, derived from the SINFONI kinematic set, using the combined model of MUSE and SINFONI data based on *pPXF* kinematics from Thater et al. [2023]. Including high-resolution SINFONI data allows for a more precise measurement performed by Thater et al. [2023] of the SMBH, which has significant influence on the orbit distribution. The SINFONI model reveals lower contribution from the cold disk (1.2%) compared to the MUSE model (11.1%), indicating a less prominent thin disk. Similarly, the counter-rotating warm and counter-rotating cold components are less dominant in the SINFONI model (4.79% and 0.78%, respectively) than in the MUSE model (23.4% and 6.6%). In contrast, the hot component dominates the SINFONI model with a luminosity fraction of 82.82%, compared to 37.4% in the

MUSE model. The SINFONI model has higher velocity peaks in the cold and counter-rotating cold components, with a maximum velocity dispersion for the hot component of $\sigma_{Hot} = 113.81\,\mathrm{km/s}$, compared to $\sigma_{Hot} = 103.42\,\mathrm{km/s}$ in the MUSE model. But since the BH mass is by 43% lower for the model from Thater et al. [2023], I do not suspect this to be reason but the different approaches used to extract stellar kinematics.

5.2. Comparison of *Bayes-LOSVD* and *pPXF*

This study compared the kinematic extraction between *Bayes-LOSVD* and *pPXF*. The first is particularly advantageous for systems that consist of multiple dynamical components, such as a NSC embedded in a host galaxy. NSCs have more intricate and overlapping kinematic features, which make non-parametric methods like *Bayes-LOSVD* better suited to capture these details [Falcon-Barroso and Martig, 2020]. In contrast, parametric methods like *pPXF* may impose constraints that might smooth out these details and would fail to resolve subtle features [Cappellari and Emsellem, 2004].
The LOSVD extracted with *pPXF* has higher inferred velocity dispersions, leading to greater mass contributions in dynamical models. This is because the Gaussian approximation produces wider standard deviations by fitting only a single component, compared to the more detailed *Bayes-LOSVD* approach, see Figure 4.8. Consequently, the *pPXF*-based dynamical model favors a higher fraction of warm and hot orbits, with more random motion and less angular momentum. In contrast, the *Bayes-LOSVD* approach, with its ability to capture finer details and avoid smoothing, results in lower velocity dispersions and smaller mass contributions. This method reveals a higher fraction of cold orbits, characterized by generally lower velocity dispersion values. The circularity λ_z peaks are therefore smaller than those derived with *pPXF* due to the narrower LOSVD tails.
This difference is evident in the decomposition based on SINFONI *pPXF* kinematics, which shows higher contribution of hot orbits and a lower fraction of dynamically cold orbits compared to the MUSE model. The MUSE model, based on *Bayes-LOSVD* kinematics, reveals a stronger contribution from dynamically cold (including counter-rotating) orbits, indicating a more prominent nuclear disk. Overall, the MUSE model displays a more balanced orbital mix with a greater thin-disk contribution.
The use of a mass map instead of a traditional surface brightness distribution implies an expected dynamical mass-to-light ratio (Y_r) of 1. However, Thater et al. [2023] found $Y_r = 0.86 \pm 0.04$ using high-resolution SINFONI data, while the best-fit MUSE model yielded $Y_r = 0.64^{+0.06}_{-0.04}$. This discrepancy may arise from the lower mass contributions inferred by *Bayes-LOSVD* kinematics.
Regarding the uncertainties in the kinematic extraction, *Bayes-LOSVD* applies a consistent Bayesian methodology across all bins, resulting in uniform uncertainty levels [Falcon-Barroso and Martig, 2020]. In contrast, *pPXF* uncertainties vary spatially, with lower values in the central regions and higher values in the outskirts, as they are weighted by the signal-to-noise ratio [Cappellari and Emsellem, 2004]. For this study, I opted not to use regularization for the *Bayes-LOSVD* kinematics to preserve subtle kinematic details, particularly in the galaxy's nucleus. While this approach resulted in higher uncertainties,

it was deemed acceptable given the primary focus on dynamical decomposition.

5.3. Discussion

The findings of this study confirm that the NSC in FCC047 has high angular momentum, strong rotation, and a high velocity dispersion as previously found in Fahrion et al. [2019]. The orbital decomposition and higher-order moments analysis suggest that the NSC consists of a high fraction of hot orbits, a cold disk, representing a distinct kinematic subpopulation, and a warm component that appears more mixed into the main body of the galaxy. These kinematic features, combined with the structural and stellar population properties of the NSC and its host galaxy from different studies, provide insights into its formation history. Traditionally, NSC formation is understood through two primary channels: in-situ star formation and the accretion of Globular Clusters (GCs) or external stellar systems [Neumayer et al., 2020, Fahrion et al., 2019]. In the in-situ scenario, the NSC might form independently of the GC system, with gas-infall from the surrounding region, such as accretion from a disk, driving efficient star formation and rapid metal enrichment [Neumayer et al., 2020]. This process typically results in NSCs with strong rotation and high metallicities, as observed in many late-type galaxies [Seth et al., 2006]. In contrast, the dry GC accretion scenario involves the inspiral of GCs due to dynamical friction, leading to NSCs that reflect the metallicity of the accreted GCs [Neumayer et al., 2020, Fahrion et al., 2019]. While this scenario often predicts weaker rotation due to the random infall directions of GCs, simulations have shown that NSCs formed through mergers of GC can still have significant rotation if they keep the angular momentum of their formation origin [Hartmann et al., 2011, Tsatsi et al., 2017, Lyubenova and Tsatsi, 2019]. Guillard et al. [2016] have shown that these processes may operate together in a hybrid scenario of gas-rich proto-star cluster accretion.

The traditional view that NSCs in low-mass galaxies are mostly formed by accretion of GC, while those in high-mass galaxies tend to form via in-situ star formation, has been refined by recent studies [see Neumayer et al., 2020, and references therein]. Fahrion et al. [2021] demonstrated that the NSC formation process cannot be fully explained by the structural properties of the host galaxy alone. Instead, they found that the NSC mass as well as the ratio of the NSC mass to the total GC system mass point to the dominant formation channel. Specifically, low-mass NSCs ($M_{\mathrm{NSC}} \leq 10^7\, M_\odot$) are predominantly formed via GC accretion, while higher-mass NSCs ($M_{\mathrm{NSC}} \geq 10^7\, M_\odot$) are primarily assembled through in-situ star formation. Fahrion et al. [2021] state that at a NSC mass of $\sim 10^7 M_\odot$, there is a "transition" between the relative importance of the GC-accretion and in-situ star formation. For FCC047, the NSC mass of $M_{\mathrm{NSC}} = 7 \pm 1.4 \times 10^8\, M_\odot$ places it firmly in the regime where in-situ formation is expected to dominate. However, since the NSC is counter-rotating, this suggests that GC accretion or the infall of an external stellar system may have also contributed to its formation.

To refine the formation history of FCC047's NSC, it is essential to consider its stellar population properties. Fahrion et al. [2019] used *pPXF* to recover the ages and metallicities of the NSC. Their results state that the NSC marks the peak of metallicity and ages in

the system. FCC047 seems to be an overall an old galaxy with an age larger than 8 Gyr, with a gradient towards older ages in the centre and the NSC with up to 13 Gyr. Fahrion et al. [2019] find that "the central region has super-solar metallicities, with a gradient towards lower metallicities within 10″ from the centre". They state that these properties are consistent with a formation scenario involving both in-situ star formation and the accretion of metal-rich GC or gas-rich star clusters very early on.
Given that the NSC in FCC047 rotates almost orthogonal to the short axis of the galaxy, the presence of a past merger-induced kinematically decoupled core could be a plausible scenario. This aligns with previous studies, such as Lyubenova and Tsatsi [2019] and Fahrion et al. [2019], who confirmed the presence of strong counter-rotation in massive NSCs, among others FCC047. There might be two kinematically decoupled components - a NSC and a disk (with an extend of up to 20″, as already suggested in Fahrion et al. [2019]) - likely linking to a major merger that has significantly changed the dynamics of FCC047.
In conclusion, the structural and stellar population properties of FCC047's NSC indicate that both formation processes, GC accretion and in-situ star formation, are necessary to explain its complex kinematics and chemical enrichment [Fahrion et al., 2019]. The high mass and strong rotation of the NSC point to a dominant role of in-situ star formation, possibly the formation scenario of the counter-rotating disk. The counter-rotating hot orbits and metal-rich stellar populations suggest an early accretion of metal-rich GCs or gas-rich star clusters [Fahrion et al., 2019]. The decoupled kinematics of the NSC, along with the presence of a second kinematically decoupled component, a disk, may not solely reflect its formation pathway but could also be the result of a major merger that significantly reshaped FCC047's structure [Fahrion et al., 2019]. The counter-rotating cold disk appears concentrated in the nucleus, while the counter-rotating warm component is more intermixed with the surrounding population, likely reflecting interactions between the counter-rotating cold disk and hot orbits. This interplay may explain why the rotation axis of the cold and warm orbits shifts by approximately 15°. These results highlight how galaxy mergers play a crucial role in driving the intricate kinematic structures seen in galactic dynamics.

5.4. Outlook

By combining kinematic models derived from *Bayes-LOSVD* (for MUSE) and SINFONI *pPXF* data, a more robust joint dynamical model could be developed. However, the integration of SINFONI *pPXF* data became feasible shortly before the completion of this thesis. Future implementations could address key limitations by introducing regularization techniques or optimizing the relative weighting of the datasets. For instance, the sheer volume of *Bayes-LOSVD* histogram data (from MUSE) compared to SINFONI's *pPXF* kinematics requires careful balancing. A regularized framework could preserve the multi-component kinematic structures resolved by *Bayes-LOSVD* while leveraging SINFONI's high spatial resolution.
A critical advancement lies in adapting the *Bayes-LOSVD* code to near-infrared (K-band)

SINFONI data. This could refine BH mass measurements, as narrower velocity dispersions, free from the limitations of Gaussian approximations, may refine measurements. This might complement findings from Thater et al. [2023], who demonstrated that spatially varying IMFs in the nucleus of FCC047 lower BH mass estimates, bringing them closer to scaling relations. By applying *Bayes-LOSVD* to SINFONI data, further reductions in BH mass uncertainties are anticipated.
In general, the *Bayes-LOSVD* method has already demonstrated its potential through its first application to an NSC, resolving subtle features such as an asymmetric LOSVD and distinct kinematic subpopulations. These capabilities provide a foundation for probing black hole and host galaxy co-evolution in dense environments.
Beyond kinematics, future work could integrate additional physical layers to improve realism:

- Variable IMFs in MGE: Implementing full spectral fitting techniques with *pPXF* to fit stellar templates (instead of stellar population templates) to infer metallicity and ages of the binned spectra and construct a mass distribution in order to model a varying stellar M/L ratio map by taking variable IMF constraints into account [Cappellari and Emsellem, 2004, Martín-Navarro et al., 2019, Martín-Navarro and Vazdekis, 2024]. This could refine the dynamical M/L ratios and could further bridge stellar population properties (e.g., metallicity, age) with dynamical modelling.
- Orbit Coloring: A planned implementation to the *DYNAMITE* software aims to "color" orbits based on metallicity or other stellar population properties, linking kinematic structures to chemical enrichment processes. This would enable a unified analysis of dynamics and stellar population gradients.

Summarized, I aim to bridge the gap between dynamical information and stellar population properties of NSCs through a comprehensive, multi-faceted approach. My PhD project will integrate dynamical modelling with stellar population analysis and refine SMBH mass measurements by applying an advanced kinematic extraction approach tailored for multi-component systems, such as galaxies hosting NSCs [Falcon-Barroso and Martig, 2020]. By combining the methodologies stated above, the project will provide a unified view of NSC formation and its role in galactic evolution, addressing key questions about how NSCs assemble, grow, and interact with their host galaxies.

Bibliography

Hst user documentation. https://hst-docs.stsci.edu/acsihb/chapter-10-imaging-reference-material/10-3-throughputs-and-correction-tables/wfc-f850lp. Date: 2024-11-20.

E. Athanassoula. Bars and secular evolution in disk galaxies: Theoretical input, 2012. URL https://arxiv.org/abs/1211.6752.

James Binney and Michael Merrifield. *Galactic Astronomy*. Princeton University Press, Princeton, NJ, 1998. ISBN 0691004021.

James Binney and Scott Tremaine. *Galactic Dynamics*. Princeton University Press, Princeton, NJ, 2nd edition, 2008. ISBN 978-0691130279.

John P. Blakeslee, Andres Jordan, Simona Mei, Patrick Cote, Laura Ferrarese, Leopoldo Infante, Eric W. Peng, John L. Tonry, and Michael J. West. The acs fornax cluster survey. v. measurement and recalibration of surface brightness fluctuations and a precise value of the fornax–virgo relative distance. 1 2009. doi: 10.1088/0004-637X/694/1/556. URL http://arxiv.org/abs/0901.1138.

Jo Bovy. *Dynamics and Astrophysics of Galaxies*. 2023. Online book available at https://galaxiesbook.org/index.html.

Andreas Burkert and Thorsten Naab. The surprising anisotropy of fast rotating, discy elliptical galaxies. *Monthly Notices of the Royal Astronomical Society*, 363(2):597–602, 10 2005. ISSN 0035-8711. doi: 10.1111/j.1365-2966.2005.09482.x. URL https://doi.org/10.1111/j.1365-2966.2005.09482.x.

N. Caon, M. Capaccioli, and M. D'Onofrio. 'Global mapping' B-band photometry of a complete sample of Fornax and Virgo early-type galaxies. , 106:199–242, August 1994. URL https://ui.adsabs.harvard.edu/abs/1994A&AS..106..199C.

Michele Cappellari. Efficient multi-gaussian expansion of galaxies. *Monthly Notices of the Royal Astronomical Society*, 333(2):400–410, June 2002. doi: 10.1046/j.1365-8711.2002.05412.x. URL https://doi.org/10.1046/j.1365-8711.2002.05412.x.

Michele Cappellari. Measuring the inclination and mass-to-light ratio of axisymmetric galaxies via anisotropic Jeans models of stellar kinematics. , 390(1):71–86, October 2008. doi: 10.1111/j.1365-2966.2008.13754.x. URL https://ui.adsabs.harvard.edu/abs/2008MNRAS.390...71C.

Michele Cappellari and Yannick Copin. Adaptive spatial binning of integral-field spectroscopic data using Voronoi tessellations. Technical report, 2003.

Michele Cappellari and Eric Emsellem. Parametric Recovery of Line-of-Sight Velocity Distributions from Absorption-Line Spectra of Galaxies via Penalized Likelihood. , 116 (816):138–147, February 2004. doi: 10.1086/381875. URL https://ui.adsabs.harvard.edu/abs/2004PASP..116..138C.

Bob Carpenter, Andrew Gelman, Matthew D. Hoffman, Daniel Lee, Ben Goodrich, Michael Betancourt, Marcus Brubaker, Jiqiang Guo, Peter Li, and Allen Riddell. Stan: A probabilistic programming language. *Journal of Statistical Software*, 76(1):1–32, 2017. doi: 10.18637/jss.v076.i01. URL https://www.jstatsoft.org/index.php/jss/article/view/v076i01.

Bradley W. Carroll and Dale A. Ostlie. *An Introduction to Modern Astrophysics*. Pearson Addison-Wesley, San Francisco, 2nd edition, 2006. ISBN 978-0805304022.

Nicolas Cretton, P. Tim de Zeeuw, Roeland P. van der Marel, and Hans-Walter Rix. Axisymmetric three-integral models for galaxies. *arXiv preprint astro-ph/9902034*, February 1999. URL https://arxiv.org/abs/astro-ph/9902034.

Herwig Dejonghe. A completely analytical family of anisotropic plummer models. *Monthly Notices of the Royal Astronomical Society*, 224(1):13–39, January 1987. doi: 10.1093/mnras/224.1.13. URL https://doi.org/10.1093/mnras/224.1.13.

Aaron A. Dutton and Andrea V. Macciò. Cold dark matter haloes in the planck era: evolution of structural parameters for einasto and NFW profiles. *Monthly Notices of the Royal Astronomical Society*, 441(4):3359–3374, may 2014. doi: 10.1093/mnras/stu742. URL https://doi.org/10.1093%2Fmnras%2Fstu742.

DYNAMITE. *Bayes LOSVD Tutorial Notebook*, 2025a. URL https://dynamics.univie.ac.at/dynamite_docs/tutorial_notebooks/4_BayesLOSVD.html. Accessed: 2025-01-08.

DYNAMITE. *Configuration Documentation for DYNAMITE Framework*, 2025b. URL https://dynamics.univie.ac.at/dynamite_docs/getting_started/configuration.html. Accessed: 2025-01-13.

Eric Emsellem, Michele Cappellari, Davor Krajnović, Katherine Alatalo, Leo Blitz, Maxime Bois, Frédéric Bournaud, Martin Bureau, Roger L. Davies, Timothy A. Davis, P. T. de Zeeuw, Sadegh Khochfar, Harald Kuntschner, Pierre-Yves Lablanche, Richard M. McDermid, Raffaella Morganti, Thorsten Naab, Tom Oosterloo, Marc Sarzi, Nicholas Scott, Paolo Serra, Glenn van de Ven, Anne-Marie Weijmans, and Lisa M. Young. The atlas3d project - iii. a census of the stellar angular momentum within the effective radius of early-type galaxies: unveiling the distribution of fast and slow rotators: Census of the stellar angular momentum in etgs. *Monthly Notices of the Royal Astronomical Society*, 414(2):888–912, May 2011. ISSN 0035-8711. doi: 10.1111/j.1365-2966.2011.18496.x. URL http://dx.doi.org/10.1111/j.1365-2966.2011.18496.x.

Katja Fahrion, Mariya Lyubenova, Glenn van de Ven, Ryan Leaman, Michael Hilker, Ignacio Martín-Navarro, Ling Zhu, Mayte Alfaro-Cuello, Lodovico Coccato, Enrico M. Corsini, Jesús Falcón-Barroso, Enrichetta Iodice, Richard M. McDermid, Marc Sarzi, and Tim de Zeeuw. Constraining nuclear star cluster formation using muse-ao observations of the early-type galaxy fcc 47. *Astronomy Astrophysics*, 628, 2019. ISSN 1432-0746. doi: 10.1051/0004-6361/201935832. URL https://doi.org/10.1051/0004-6361/201935832.

Katja Fahrion, Ryan Leaman, Mariya Lyubenova, and Glenn van de Ven. Disentangling the formation mechanisms of nuclear star clusters. 12 2021. doi: 10.1051/0004-6361/202039778. URL http://arxiv.org/abs/2112.05610.

J. Falcon-Barroso and M. Martig. Bayes-losvd: a bayesian framework for non-parametric extraction of the line-of-sight velocity distribution of galaxies. 11 2020. doi: 10.1051/0004-6361/202039624. URL http://arxiv.org/abs/2011.12023.

Laura Ferrarese and Holland Ford. Supermassive black holes in galactic nuclei: Past, present and future research. *Space Science Reviews*, 116(3–4):523–624, February 2005. doi: 10.1007/s11214-005-3947-6. URL https://doi.org/10.1007/s11214-005-3947-6.

Nicolas Guillard, Eric Emsellem, and Florent Renaud. New insights on the formation of nuclear star clusters. *Monthly Notices of the Royal Astronomical Society*, 461 (4):3620–3629, 06 2016. ISSN 0035-8711. doi: 10.1093/mnras/stw1570. URL https://doi.org/10.1093/mnras/stw1570.

Markus Hartmann, Victor P. Debattista, Anil Seth, Michele Cappellari, and Thomas R. Quinn. Constraining the role of star cluster mergers in nuclear cluster formation: simulations confront integral-field data. , 418(4):2697–2714, December 2011. doi: 10.1111/j.1365-2966.2011.19659.x. URL https://ui.adsabs.harvard.edu/abs/2011MNRAS.418.2697H.

Prashin Jethwa, Sabine Thater, Thomas Maindl, and Glenn Van de Ven. DYNAMITE: DYnamics, Age and Metallicity Indicators Tracing Evolution. Astrophysics Source Code Library, November 2020. URL https://ui.adsabs.harvard.edu/abs/2020ascl.soft11007J.

John Kormendy and Douglas Richstone. Inward bound—the search for supermassive black holes in galactic nuclei. *Annual Review of Astronomy and Astrophysics*, 33:581–624, 1995. doi: 10.1146/annurev.aa.33.090195.003053. URL https://doi.org/10.1146/annurev.aa.33.090195.003053.

Christopher M. Liepold, Matthew E. Quenneville, Chung-Pei Ma, Jonelle L. Walsh, Nicholas J. McConnell, Jenny E. Greene, and John P. Blakeslee. The massive survey –

xv. a stellar dynamical mass measurement of the supermassive black hole in massive elliptical galaxy ngc 1453. 1 2020. doi: 10.3847/1538-4357/ab6f71. URL http://arxiv.org/abs/2001.08753.

Mariya Lyubenova and Athanassia Tsatsi. Nuclear angular momentum of early-type galaxies hosting nuclear star clusters. *Astronomy Astrophysics*, 629, September 2019. doi: 10.1051/0004-6361/201833954. URL https://doi.org/10.1051/0004-6361/201833954.

I. Martín-Navarro, M. Lyubenova, G. van de Ven, J. Falcón-Barroso, L. Coccato, E. M. Corsini, D. A. Gadotti, E. Iodice, F. La Barbera, R. M. McDermid, F. Pinna, M. Sarzi, S. Viaene, P. T. de Zeeuw, and L. Zhu. Fornax 3d project: A two-dimensional view of the stellar initial mass function in the massive lenticular galaxy fcc 167. *Astronomy Astrophysics*, 626, June 2019. doi: 10.1051/0004-6361/201935360. URL https://doi.org/10.1051/0004-6361/201935360.

I. Martín-Navarro and A. Vazdekis. Counting stars from the integrated spectra of galaxies. 10 2024. doi: 10.1051/0004-6361/202451604. URL http://arxiv.org/abs/2410.11961.

Benjamin P. Moster, Thorsten Naab, and Simon D. M. White. Galactic star formation and accretion histories from matching galaxies to dark matter haloes. *Monthly Notices of the Royal Astronomical Society*, 428(4):3121–3138, February 2013. doi: 10.1093/mnras/sts261. URL https://doi.org/10.1093/mnras/sts261.

Clemens Nagel. *"Einführung in das experimentelle Arbeiten", Lecture material from SS2017, Fakulty of Physics, Uni Wien*. 2020.

Julio F. Navarro, Carlos S. Frenk, and Simon D. M. White. The structure of cold dark matter halos. *The Astrophysical Journal*, 462:563, May 1996. doi: 10.1086/177173. URL https://doi.org/10.1086/177173.

Nadine Neumayer. Nuclear star clusters - structure and stellar populations. 11 2012. URL http://arxiv.org/abs/1211.1795.

Nadine Neumayer, Anil Seth, and Torsten Böker. Nuclear star clusters. *The Astronomy and Astrophysics Review*, 28(4), December 2020. ISSN 0935-4956. doi: 10.1007/s00159-020-00125-0. URL https://doi.org/10.1007/s00159-020-00125-0.

European Southern Observatory. Sinfoni: The spectrograph for integral field observations in the near infrared, 2019. URL https://www.eso.org/sci/facilities/paranal/decommissioned/sinfoni.html. Accessed: 2024-11-26.

European Southern Observatory. Muse: Multi unit spectroscopic explorer, 2024. URL https://www.eso.org/sci/facilities/paranal/instruments/muse.html. Accessed: 2024-11-26.

P. J. E. Peebles. Star distribution near a collapsed object. *The Astrophysical Journal*, 178:371–376, 1972. doi: 10.1086/151797. URL https://doi.org/10.1086/151797.

Joel Pfeffer, J M Diederik Kruijssen, Robert A Crain, and Nate Bastian. The E-MOSAICS project: simulating the formation and co-evolution of galaxies and their star cluster populations. *Monthly Notices of the Royal Astronomical Society*, 475 (4):4309–4346, 12 2017. ISSN 0035-8711. doi: 10.1093/mnras/stx3124. URL https://doi.org/10.1093/mnras/stx3124.

H. C. Plummer. On the problem of distribution in globular star clusters. *Monthly Notices of the Royal Astronomical Society*, 71:460–470, 1911. doi: 10.1093/mnras/71.5.460. URL https://doi.org/10.1093/mnras/71.5.460.

Gustav Rasmussen. Structural and dynamical properties of dark matter halos. Master's thesis, University of Copenhagen, May 2016. URL https://www.researchgate.net/publication/314913282.

Hans-Walter Rix, P. Tim de Zeeuw, Nicolas Cretton, Roeland P. van der Marel, and C. Marcella Carollo. Dynamical Modeling of Velocity Profiles: The Dark Halo around the Elliptical Galaxy NGC 2434. , 488(2):702–719, October 1997. doi: 10.1086/304733. URL https://ui.adsabs.harvard.edu/abs/1997ApJ...488..702R.

P. Sánchez-Blázquez, R. F. Peletier, J. Jiménez-Vicente, N. Cardiel, A. J. Cenarro, J. Falcón-Barroso, J. Gorgas, S. Selam, and A. Vazdekis. Medium-resolution Isaac Newton Telescope library of empirical spectra. , 371(2):703–718, September 2006. doi: 10.1111/j.1365-2966.2006.10699.x. URL https://ui.adsabs.harvard.edu/abs/2006MNRAS.371..703S.

Giulia Santucci, Sarah Brough, Jesse van de Sande, Richard M. McDermid, Glenn van de Ven, Ling Zhu, Francesco D'Eugenio, Joss Bland-Hawthorn, Stefania Barsanti, Julia J. Bryant, Scott M. Croom, Roger L. Davies, Andrew W. Green, Jon S. Lawrence, Nuria P. F. Lorente, Matt S. Owers, Adriano Poci, Samuel N. Richards, Sabine Thater, and Sukyoung Yi. The sami galaxy survey: The internal orbital structure and mass distribution of passive galaxies from triaxial orbit-superposition schwarzschild models. *The Astrophysical Journal*, 930(2):153, May 2022. ISSN 1538-4357. doi: 10.3847/1538-4357/ac5bd5. URL http://dx.doi.org/10.3847/1538-4357/ac5bd5.

Martin Schwarzschild. A numerical model for a triaxial stellar system in dynamical equilibrium, 1979.

Nicholas Scott, Roger L. Davies, Ryan C. W. Houghton, Michele Cappellari, Alister W. Graham, and Kevin A. Pimbblet. Distribution of slow and fast rotators in the fornax cluster. *Monthly Notices of the Royal Astronomical Society*, 441:274–288, 2014. doi: 10.1093/mnras/stu472. URL https://doi.org/10.1093/mnras/stu472.

J. A. Sellwood. Secular evolution in disk galaxies. *Reviews of Modern Physics*, 86(1): 1–46, 2014. doi: 10.1103/RevModPhys.86.1. URL https://doi.org/10.1103/RevModPhys.86.1.

Anil C. Seth, Julianne J. Dalcanton, Paul W. Hodge, and Victor P. Debattista. Clues to Nuclear Star Cluster Formation from Edge-on Spirals. , 132(6):2539–2555, December 2006. doi: 10.1086/508994. URL https://ui.adsabs.harvard.edu/abs/2006AJ....132.2539S.

Simbad2024. *Simbad basic query result FCC047*. Date: 2024-11-20.

Stan Development Team. *Stan: A Probabilistic Programming Language*, 2023. URL https://mc-stan.org. Version 2.32.0, Accessed: 2025-01-29.

Thomas S. Statler. Self-consistent Models of Perfect Triaxial Galaxies. , 321:113, October 1987. doi: 10.1086/165619. URL https://ui.adsabs.harvard.edu/abs/1987ApJ...321..113S.

Sabine Thater, Davor Krajnović, Martin A. Bourne, Michele Cappellari, Tim de Zeeuw, Eric Emsellem, John Magorrian, Richard M. McDermid, Marc Sarzi, and Glenn van de Ven. A low upper mass limit for the central black hole in the late-type galaxy ngc 4414. 10 2016. doi: 10.1051/0004-6361/201629480. URL http://arxiv.org/abs/1610.04269.

Sabine Thater, Prashin Jethwa, Behzad Tahmasebzadeh, Ling Zhu, Mark den Brok, Giulia Santucci, Yuchen Ding, Adriano Poci, Edward Lilley, P. Tim de Zeeuw, Alice Zocchi, Thomas I. Maindl, Fabio Rigamonti, Meng Yang, Katja Fahrion, and Glenn van de Ven. On the robustness of triaxial schwarzschild modelling: The effects of correcting the orbit mirroring. *Astronomy Astrophysics*, 667:A51, November 2022. doi: 10.1051/0004-6361/202243926. URL https://doi.org/10.1051/0004-6361/202243926.

Sabine Thater, Mariya Lyubenova, Katja Fahrion, Ignacio Martín-Navarro, Prashin Jethwa, Dieu D. Nguyen, and Glenn van de Ven. Effect of the initial mass function on the dynamical smbh mass estimate in the nucleated early-type galaxy fcc 47. 4 2023. URL http://arxiv.org/abs/2304.13310.

A. Tsatsi, M. Lyubenova, G. van de Ven, J. Chang, J. A. L. Aguerri, J. Falcón-Barroso, and A. V. Macciò. CALIFA reveals prolate rotation in massive early-type galaxies: A polar galaxy merger origin? , 606:A62, October 2017. doi: 10.1051/0004-6361/201630218. URL https://ui.adsabs.harvard.edu/abs/2017A&A...606A..62T.

R. C. E. van den Bosch, G. van de Ven, E. K. Verolme, M. Cappellari, and P. T. de Zeeuw. Triaxial orbit based galaxy models with an application to the (apparent) decoupled core galaxy ngc 4365. *Monthly Notices of the Royal Astronomical Society*, 385(2):647–666, April 2008. doi: 10.1111/j.1365-2966.2008.12874.x. URL https://doi.org/10.1111/j.1365-2966.2008.12874.x.

Ling Zhu, Remco van den Bosch, Glenn van de Ven, Mariya Lyubenova, Jesús Falcón-Barroso, Sharon E. Meidt, Marie Martig, Juntai Shen, Zhao-Yu Li, Akin Yildirim, C. Jakob Walcher, and Sebastian F. Sanchez. Orbital decomposition of califa spiral galaxies. 9 2017. doi: 10.1093/mnras/stx2409. URL http://arxiv.org/abs/1709.06649.

Ling Zhu, Glenn van de Ven, Remco van den Bosch, Hans-Walter Rix, Mariya Lyubenova, Jesús Falcón-Barroso, Marie Martig, Shude Mao, Dandan Xu, Yunpeng Jin, Aura Obreja, Robert J. J. Grand, Aaron A. Dutton, Andrea V. Macciò, Facundo A. Gómez, Jakob C. Walcher, Rubén García-Benito, Stefano Zibetti, and Sebastián F. Sánchez. The stellar orbit distribution in present-day galaxies inferred from the califa survey. *Nature Astronomy*, 2:233–238, March 2018. doi: 10.1038/s41550-017-0348-1. URL https://doi.org/10.1038/s41550-017-0348-1.

A. Appendix

A.1. MGE

The fitted MGE parameters for the projected mass distribution with a spatially varying M/L ratio and a Milky-Way like IMF, see Table A.1, and for the projected stellar light distribution with a constant M/L ratio, see Table A.2.

Σ_j [$M_\odot$ pc^{-2}]	σ_j [arcsec]	q_j
120605.50	0.0340	0.9999
231471.60	0.0820	0.9999
116595.41	0.1709	0.6425
19193.38	0.4089	0.7142
4042.31	0.5630	0.9999
6721.78	0.7964	0.8249
3317.37	1.4020	0.9999
1278.50	2.4749	0.9999
628.81	4.3952	0.9819
384.99	4.5254	0.4900
378.52	8.4004	0.9052
167.00	20.1851	0.7177
26.97	56.0465	0.9789
22.94	56.0465	0.4900

Table A.1.: Projected mass distribution with spatially varying M/L and MW-like IMF.

I_j [$L_\odot$ pc^{-2}]	σ_j [arcsec]	q_j
40064.07	0.0236	0.9919
14543.81	0.0382	0.5720
89491.19	0.0883	0.8744
39861.01	0.1705	0.7237
6212.08	0.4671	0.6806
2995.64	0.6038	0.9999
1656.73	1.2777	0.8853
841.17	2.4291	0.9225
51.03	3.7395	0.9178
319.28	4.9925	0.8903
163.89	9.2963	0.9139
1.77	22.9579	0.4900
69.97	23.9823	0.6518
20.53	56.0367	0.8572

Table A.2.: Projected stellar light distribution with constant M/L, no IMF considered.

A.2. *Bayes-LOSVD* Kinematics

See Figure A.1 for the LOSVD bins aligning with the galaxy's nucleus and the surrounding region, as it can be assumed that the NSC is located in bin 0. With $R_{\mathrm{eff,NSC}} = 66.5$ pc $= 0.74''$ and given the pixel scale of $0.2''$ per pixel, the NSC can formally be resolved with MUSE. Primary peaks are centred at the systemic velocity $(0km/s)$, indicating a dominance of ordered motion. Secondary peaks, when present, are often offset by 200–300 km/s. I find single-peakek LOSVDs that suggest a uniform stellar population, double-peaked LOSVDs closer to the centre, indicating the presence of two stellar components moving at distinct velocities e.g. presence of a stellar disk. And finally, triple-peaked LOSVDs in the nucleus pointing to the presence of more than two distinct kinematic components, suggesting highly complex dynamics near the NSC.
See Figure A.2 for a randomly sampled selection of bins. Covering the central region up to the outskirts of the galaxy, providing a broader view of the kinematic diversity. The closer to the nucleus, the more complex and sharper the LOSVDs compared to the outskirts, reflecting higher velocity dispersions and stronger gravitational influence. The peaks in the outskirts tend to be broader, single-peaked and less defined.

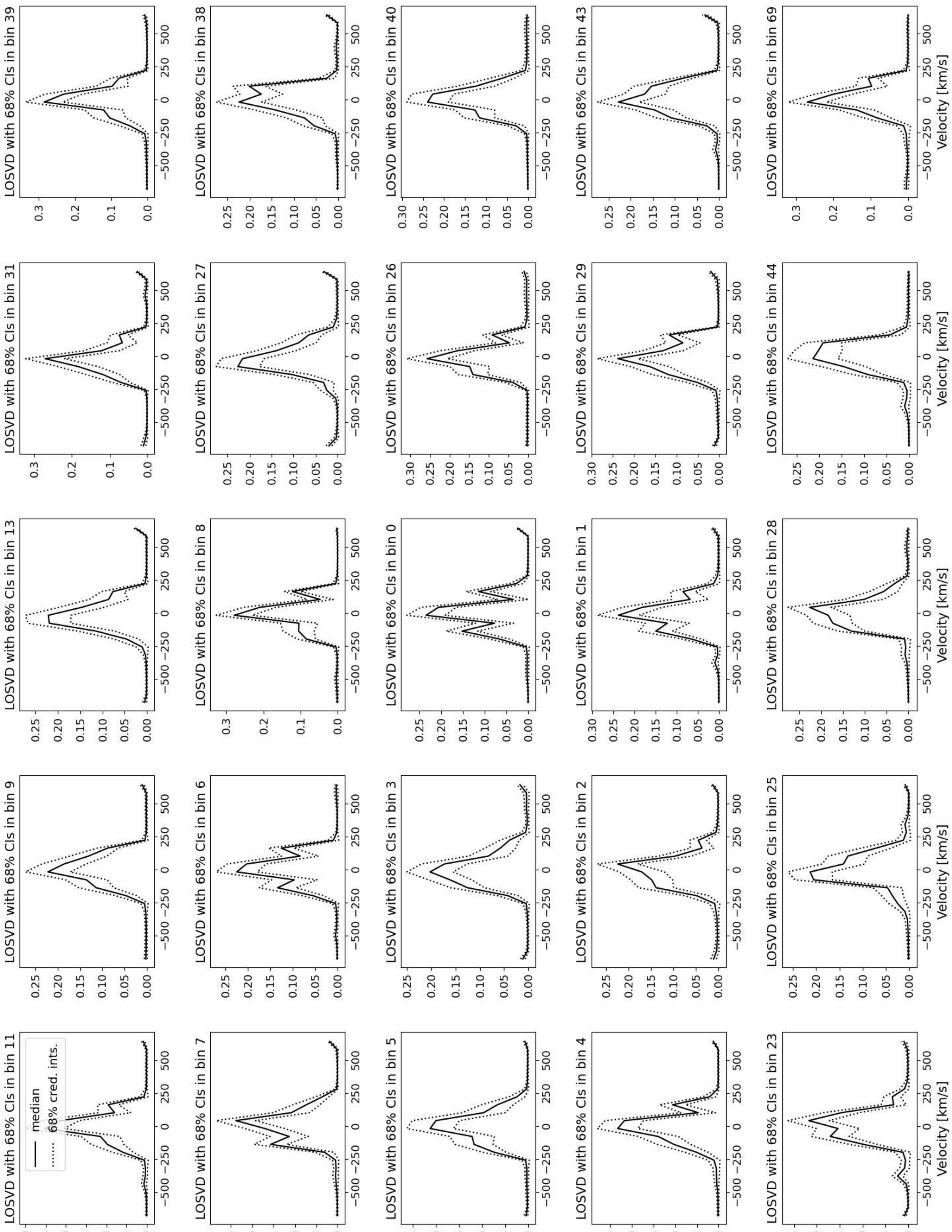

Figure A.1.: Plot showing the LOSVD bins that correspond to the nucleus where the NSC is expected to reside. The dotted line correspond to the 68% confidence interval, the solid line is the median LOSVD.

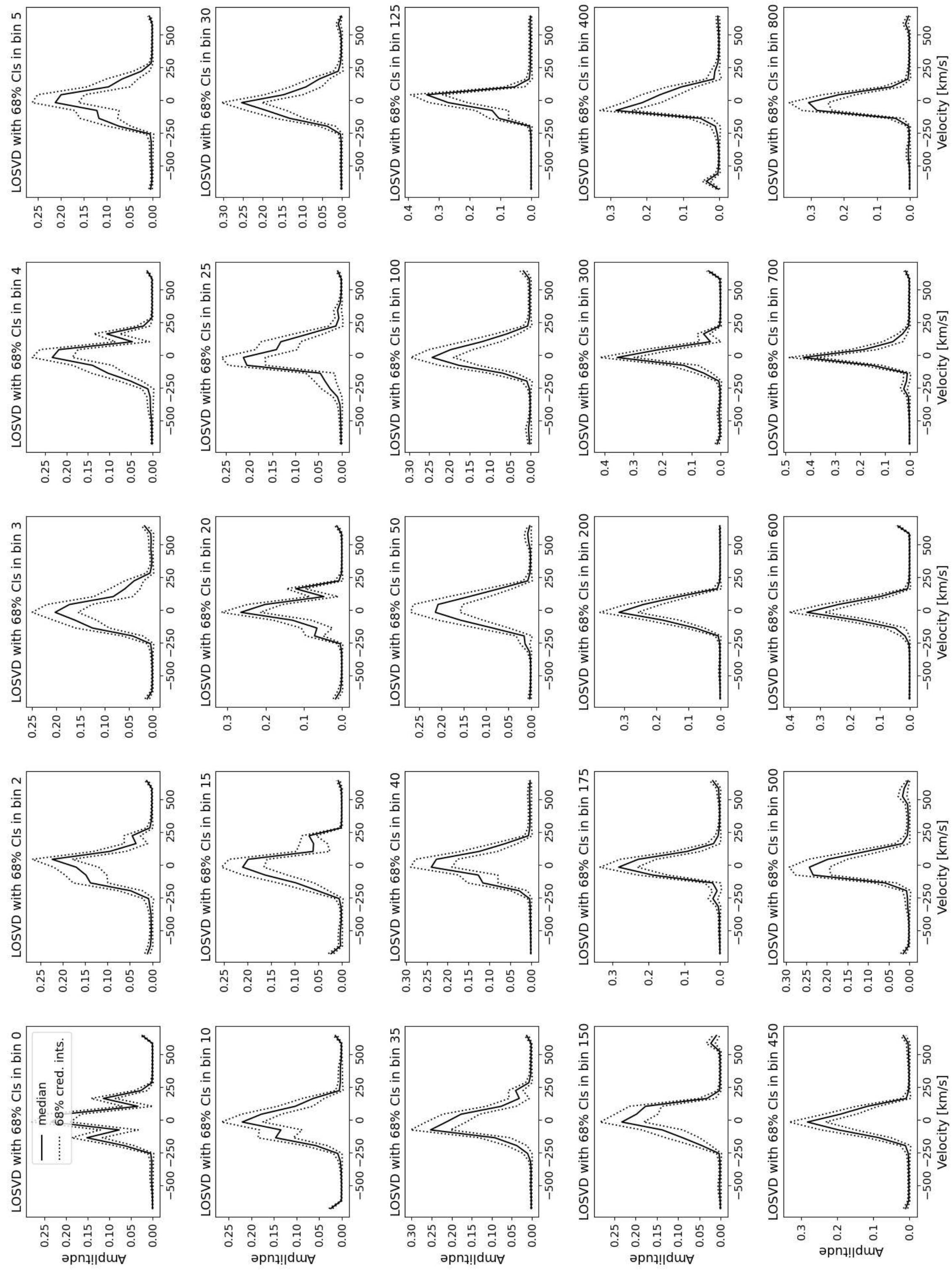

Figure A.2.: LOSVD Histograms of different bins sampled around the galaxy. The dotted line correspond to the 68% confidence interval, the solid line is the median LOSVD.

A.3. Inaccuracy of Kinematics Re-calculation: Comparison of different Approaches with the DYNAMITE Routine

In this section, I highlight inaccuracies that arise during the kinematic re-calculation for individual components. I illustrate these issues using the counter-rotating components as an example. The subject of comparison are two different methods: 1. Using the amplitude of the LOSVD histogram as the velocity and the standard deviation of that histogram as the velocity dispersion. 2. Fitting a Gaussian to the LOSVD histogram and then use the fits' amplitude and standard deviation as the kinematic properties. Both approaches have been tested with the same code, the DYNAMITE routine, for reasons of consistency. See Figure A.3 for the kinematics of the counter-rotating cold and counter-rotating warm component. The first column presents the velocity, the second the velocity dispersion, respectively, both derived with the Gaussian-fit (first row) and the moments-approach (second row). The third row displays the delta in measurements of those two approaches. For the delta, the moments-approach measurement has been subtracted from the Gaussian measurement.

Component	max $\|v_G\|$	$\sigma_{max,G}$	max $\|v_M\|$	$\sigma_{max,M}$
Cr cold	88.7	119.4	76.7	96.7
Cr warm	60.8	103.1	54.9	89.8

Table A.3.: Comparison of maximum absolute velocity and velocity dispersion values derived from Gaussian fits and moments-based approaches for the counter-rotating cold and counter-rotating warm components.

For the counter-rotating cold component, the maximum velocity difference is 23.14 km/s, and the maximum velocity dispersion difference is 22.67 km/s. For the counter-rotating warm component, the maximum velocity difference is 15.34 km/s, and the maximum velocity dispersion difference is 13.29 km/s. These values highlight the discrepancies between the two methods in measuring kinematic properties. The largest deviation are found in the nucleus, where I find the largest measurements. It can be said, the larger the absolute measurement in velocity or velocity dispersion, the larger the deviation between the two methods. A Gaussian-fit to a LOSVD appears wider and simultaneously stretched compared to the initial LOSVD. For the decompositions presented above, for both models, MUSE and SINFONI data, the moments approach has been used.

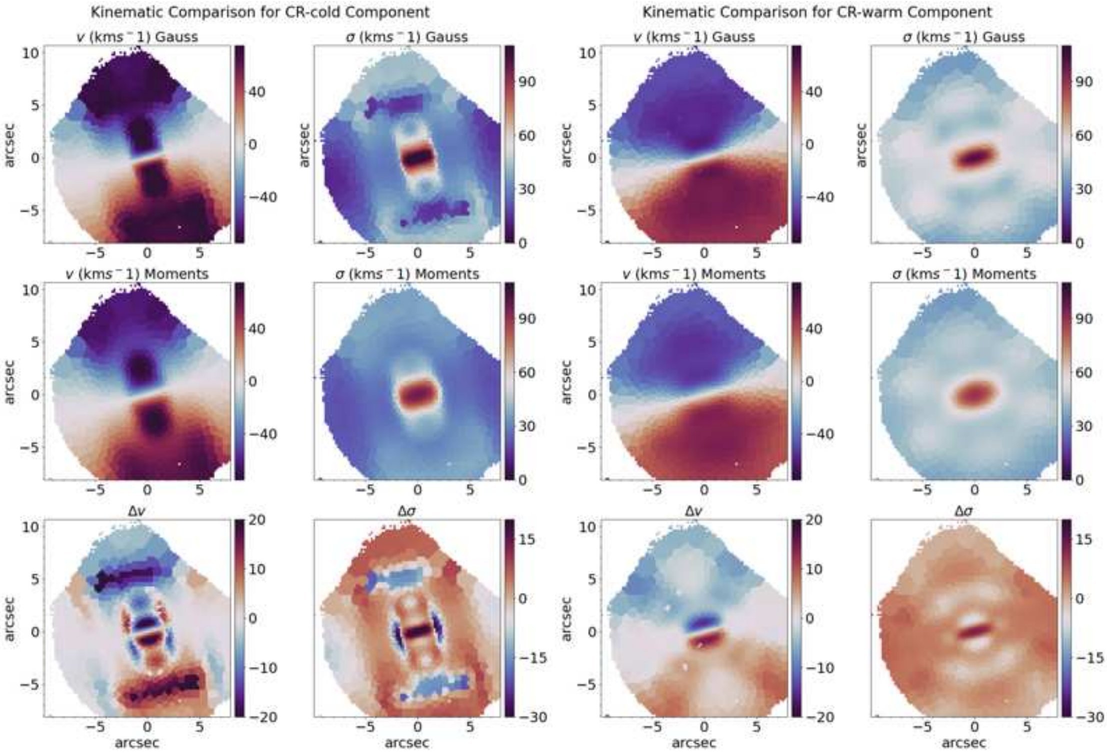

Figure A.3.: Kinematics of the counter-rotating thin and counter-rotating thick component derived from Gaussian fits and moments-based approaches. The last row presents the deviations between the two approaches.